Investigating the Quantitative Nature of Magnetization Transfer in vivo at 3 tesla

By

Alex Kenneth Smith

Dissertation
Submitted to the Faculty of the
Graduate School of Vanderbilt University
in partial fulfillment of the requirements
for the degree of

DOCTOR OF PHILOSOPHY
in

Biomedical Engineering
December, 2016
Nashville, Tennessee

Approved:

Seth A Smith, Ph.D.
Adam W Anderson, Ph.D.
Richard D Dortch, Ph.D.
Siddharama Pawate, M.D.
E. Brian Welch, Ph.D.

ACKNOWLEDGEMENTS

I would like to thank my wonderful advisor Seth Smith for all the guidance, support, witty banter, and insight he has provided over my past four years here. He has ignited the excitement I feel for research, and has taught me many things about research and the many different future career paths that lay before me. The contributions I have summarized here would not have been possible without his counsel, encouragement, and funding. I would also like to thank my committee members Dr. Anderson, Dr. Dortch, Dr. Pawate, and Dr. Welch for all of their instruction and guidance these past few years that helped forge me into the researcher and person I am today.

I would also like to particularly thank Sam By, Aliya Gifford, and Kristin O'Grady. They were pivotal to helping me revise and edit this dissertation; without them, I would have not found nearly all the mistakes and poor grammar choices that I made throughout the writing of this dissertation.

Last, I would like to thank my wife, Allison. You are the light of my life, and without you, this world would be a darker place.

"An expert is a person who has made all the mistakes that can be made in a very narrow field."
~Neils Bohr

TABLE OF CONTENTS

Page

LIST OF TABLES

Table Page

LIST OF FIGURES

Figure Page

LIST OF ABBREVIATIONS

ANOVA	Analysis of variance
APT	Amide proton transfer
AUC	Area under the curve
B_0	Static main magnetic field
B_1	Excitation magnetic field
BET	Brain extraction tool
CEST	Chemical exchange saturation transfer
CI	Confidence interval
CNS	Central nervous system
CSF	Cerebrospinal fluid
CW	Continuous wave
D_{BA}	Bland-Altman difference
DC	Dorsal column
DTI	Diffusion tensor imaging
DWS	Direct water saturation
EDSS	Kurztke expanded disability status scale
EPI	Echo planar imaging
f	free water pool
F^{19}	Flourine-19
FID	Free induction decay
FLIRT	FSL linear image registration tool
FOV	Field of View
FSL	FMRIB Software library
GM	Grey matter
GRE	Gradient recalled echo
IC	Internal capsule
ihMT	Inhomogeneous magnetization transfer
ihMTR	inhomogeneous magnetization transfer ratio
k_{mf}	Macromolecular to free chemical exchange rate
LC	Lateral columns
LOA	Limits of agreement for the Bland-Altman test
m	macromolecular pool
MAD	Mean absolute difference
MFA	Multiple flip angle
mFFE	Multiple fast field echo
MIPAV	Medical image processing, analysis, and visualization application
MPF	Macromolecular pool fraction
MRI	Magnetic resonance imaging
MS	multiple sclerosis
MT	Magnetization transfer
MTR	Magnetization transfer ratio
MTR_{Asym}	Magnetization transfer ratio asymmetry

N^{14}	Nitrogen-14
NAWM	Normal appearing white matter
NIH	National Institutes of Health
NMR	Nuclear magnetic resonance
NOE	Nuclear Overhauser effect
OCC	Occipital calcarine cortex
ODE	Ordinary differential equation
ON	Optic nerve
OP	Out-of-phase
P	Putamen
ppm	Parts per million
PPMS	Primary progressive multiple sclerosis
PSR	Macromolecular to free pool size ratio
qMT	Quantitative magnetization transfer
R_1	Longitudinal relaxation rate
R_{1f}	Longitudinal relaxation rate in the free pool
R_{1m}	Longitudinal relaxation rate in the macromolecular pool
R_{1obs}	Observed longitudinal relaxation rate
R_2	Transverse relaxation rate
RF	Radio frequency
RL	Right/left direction
ROI	Region of interest
RRMS	Relapsing-remitting multiple sclerosis
s	solute pool
Sp	Splenium
S_0	MT reference image
SAR	Specific absorption rate
SC	Spinal cord
SD	Standard deviation
SENSE	Sensitivity encoding
SIR	Selective inversion recovery
SNR	Signal to noise ratio
SPAIR	Spectral attenuated inversion recovery
SPGR	Spoiled gradient recalled acquisition
SPIR	Spectral presaturation with inversion recovery
STIR	Short TI inversion recovery
T	tesla
T_1	Longitudinal relaxation time
T_2	Transverse relaxation time
T_{2f}	Transverse relaxation time in the free pool
T_{2m}	Transverse relaxation time in the macromolecular pool
TE	Echo time
TLC	Thoracolumbar spinal cord
TR	Repetition time

W	Water
WASSR	Water saturation shift referencing
WM	White matter
χ^2	Chi-squared goodness of fit metric
$\Delta\omega$	Offset frequency from water
α	Flip angle

Chapter 1: Introduction

1.1. Objective

The theories and experiments described in this thesis aim to advance the in vivo utility of magnetization transfer (MT) at clinical field strengths (e.g., 3 tesla (T)). MT pulse sequences have the ability to probe tissue macromolecular content by exploiting dipolar and chemical exchange, a biophysical phenomenon where hydrogen atoms in macromolecular tissue components, such as in the myelin of white matter, exchange information with the surrounding hydrogen atoms attached to water. MT experiments have been used to characterize healthy tissues such as in the brain (1-13), spinal cord (11,14,15), and muscle (16-22). Additionally, MT has been shown to be sensitive to several different pathologies, including multiple sclerosis (MS) (13,23-29), Lupus erythematosus (30), dementia, Huntington's, Parkinson's (31), and schizophrenia (32).

While the MT effect can be measured by utilizing a variety of pulse sequences, the focus of this thesis will be on off-resonance saturation-based MT, as formalized by Wolff and Balaban (33). By applying a large amplitude saturation pulse off-resonance with respect to water, tissue macromolecules (so-called macromolecular pool) can be selectively saturated; the saturation will then exchange with water protons (so-called free pool) through the MT effect. Previous work has built a solid foundation to study the MT effect in vivo (15,33-39); however, the existing literature has not explored in depth into how the MT effect can be better exploited to aid clinical diagnosis. Several previous studies (40-43) have introduced new methods and concepts regarding the MT effect, however, many of these techniques have not been tailored towards clinical implementation in the human imaging domain. Additionally, when MT is a confounding factor, a few researchers (40,43-45) have found ways to model the MT component in CEST, however, they have not provided a clinically utilizable acquisition and modeling strategy to effectively remove this effect to improve the sensitivity to the CEST effect alone, which this dissertation aims to overcome. Advancing methods of characterizing tissues using MT will be valuable for understanding tissue macromolecular composition, as well as characterizing pathologies at clinical field strengths.

In this chapter, a brief summary of the history of MT is provided, followed by the fundamental background that explains the manner in which magnetic resonance imaging (MRI) works and the foundation of MT upon which this thesis is based. This chapter then concludes with a brief overview of the body of work contained herein.

1.2. Background Theory in MT

1.2.1. A Brief History of Magnetization Transfer

MRI has proven to be remarkably versatile since its inception, introducing many different types of contrasts that can provide exceptional anatomical detail, including the ability to quantitatively characterize the underlying tissue structure and function within organs and systems. In particular, magnetization transfer (MT) has proven to be an important method of probing tissue macromolecular structure and composition that cannot be captured from conventional MRI contrasts alone.

After Bloch discovered and formulated the now famous Bloch equations in 1946 (46,47), describing how the magnetic moments of nuclei will form a magnetization vector in a static magnetic field, a period of rapid discovery occurred. Only a few years later, resonance shifts due to electronic shielding were observed in several different media (48-50). In particular, in 1950 Dickinson (49) & Proctor and Yu (50) each demonstrated that the resonance frequencies of F^{19} and N^{14}, respectively, would change depending on which compound they were within. Later, Gutowsky, et al. (51) in 1953 discovered that nuclei could induce an observable magnetic moment on other nuclei, laying the foundations for exchange-related nuclear magnetic resonance (NMR) spectroscopy and for assessing physiologic processes such as chemical exchange.

Finally, after several years of deriving line-shape reaction-rate formulas as solutions to the Bloch equations with exchange, in 1958 McConnell (52) simplified these equations to form the two pool (macromolecular and free) Bloch-McConnell equations, which was modified to add a chemical exchange component. These equations are fundamental for describing how systems exchange NMR signal over time, and are the foundations for current research into multi-pool systems. Experiments by Edzes and Samulski (16,53) in 1977 and 1978 demonstrated some of the first studies showing that water molecules in biological systems are perturbed by exchange

from other tissues. By utilizing collagen and muscle tissue, they demonstrated that macromolecular protons affect water T_1 relaxation, and thus, proved that exchange occurs between water and its surroundings in biological systems. In 1986, Sobol, et al. (17) further demonstrated that T_1 relaxation of water changes in biological tissues, and importantly, developed some of the first estimates of the exchange rate between water and the semi-solid macromolecular components.

The first example of MT in vivo was performed in 1989 by Wolff and Balaban (33) in a rabbit kidney. They demonstrated that by irradiating off-resonance from water, they could selectively saturate the restricted, macromolecular pool; this in turn attenuated the water signal through dipole-dipole (54) and chemical exchange (55) between macromolecular and free water protons. A few years later, in 1991, Caines, et al. (18) utilized these experiments to incorporate off-resonance saturation effects into the Bloch-McConnell equations, providing one of the first models to simulate saturation transfer experiments. To test these theories in vitro, in 1993 Henkelman, et al. (34) applied these equations to agar phantoms, demonstrating that these models can be applied to quantify the MT effect. The improvement from this group was the addition of a line shape function/model for the MT (macromolecular) pool, which is now adopted as current practice for modeling the MT pool. Morrison (3,19) in 1995 refined the theories proposed by Henkelman and predecessors by incorporating a super-Lorentzian function for the MT pool line shape in tissues. She theorized that membrane proteins or lipids are primarily participating in exchange in these large, solid tissues, and thus, can be approximated by using a super-Lorentzian line shape, while liquids like blood exhibit a more Lorentzian line shape due to the lack of these proteins and lipids.

The robust translation towards human in vivo MT experiments was supported by Sled and Pike (35,36) in 2000 and 2001 when they developed a pulsed steady state spoiled gradient echo (SPGR) sequence to generate MT contrast that could be easily deployed on human scanners. Early MT acquisitions relied on continuous wave (CW) pulses (4,5), which are long high-amplitude RF saturation pulses. However, CW pulses are difficult to employ in human scanners due to hardware (CW pulses utilize specialized transmit coils) and power (CW pulses typically require high amplitude pulses, which may exceed human safety limits) constraints. Pulse trains were also

employed to reduce hardware constraints (56), but these were still not as time-efficient as the pulsed method Sled and Pike introduced. Alternatively, Gochberg, et al. (57) demonstrated that a selective inversion recovery (SIR) acquisition scheme can also yield MT contrast and offer quantifiable indices, however, it was less time efficient than the pulsed approach presented by Sled and Pike. Sled and Pike provided an acquisition method that was much faster than the above techniques, and could easily be deployed over large volumes with minimal hardware demands, making this acquisition strategy ideal for clinical use. This pulse sequence has been so integral to fast imaging, that it is still one of the dominant strategies for in vivo MT imaging today.

The progression of magnetization transfer theory has been rapid, and the growth of applications has been tremendous since the discovery of MT-based contrasts. These newly developed acquisition strategies and processing techniques make MT an important investigatory tool for examining the underlying microstructure in a variety of tissues today, both in research and in the clinic and variants on such techniques are the benchmark for this body of work.

1.2.2. Basic MR Theory

The NMR phenomenon arises from nuclear spins interacting with a static magnetic field. In order for a nucleus to be detectable in an NMR experiment, it must have intrinsic angular momentum ($\boldsymbol{S}$), known as spin. This angular momentum induces a magnetic dipole in these nuclei, given by:

$$\boldsymbol{\mu} = \gamma \boldsymbol{S} \qquad 1.1$$

where γ is the gyromagnetic ratio (42.58 MHz/T for protons). From quantum mechanics, while the NMR phenomenon may arise within any nucleus with spin quantum number $I > 0$, MRI is almost exclusively performed on the protons of water molecules (where $I = 1/2$), and thus will serve as an example without loss of generality. There are naturally $2I + 1$ degenerate spin states for a nucleus of spin quantum number I, but placing the nucleus in an external magnetic field ($\boldsymbol{B_0}$) breaks the degeneracy by splitting the energy states (orientations) into high and low energy, and thus, for protons, this splitting results in two possible orientations, spin up (low energy) and spin down (high energy). These orientations are governed by the thermal equilibrium condition, which is characterized by the Boltzmann distribution. Letting N^+ be the higher energy state (anti-parallel to $\mathbf{B_0}$), and N^- be the lower energy state, Boltzmann dictates:

$$\frac{N^+}{N^-} = e^{-\frac{\Delta E}{kt}} \quad 1.2$$

where k is Boltzmann's constant, T is temperature (in kelvin), and ΔE is the energy difference between the N^+ and N^- states, defined as $\Delta E = \hbar\gamma B_0$, where $\hbar$ is Planck's constant.

Returning to classical mechanics principles, these spins will attempt to align with the external magnetic field, and will therefore experience a torque. This torque is defined as the rate of change of the angular momentum:

$$\frac{d\boldsymbol{S}}{dt} = \boldsymbol{\mu}\times\boldsymbol{B} \quad 1.3$$

Furthermore, unless these dipoles are perfectly aligned with the $\boldsymbol{B_0}$ field, they will trace a circular path about the axis of $\boldsymbol{B_0}$, which is called precession. The rate of this precession is $\omega_0 = \gamma B_0$, where ω_0 is defined as the Larmor frequency.

Multiplying both sides of Equation 1.3 by γ produces:

$$\frac{d\boldsymbol{\mu}}{dt} = \boldsymbol{\mu}\times\gamma\boldsymbol{B} \quad 1.4$$

And finally, considering that these forces will sum over a spin system (such as tissue), we find

$$\frac{d\boldsymbol{M}}{dt} = \boldsymbol{M}\times\gamma\boldsymbol{B} \quad 1.5$$

where **M** is the net magnetization. These are the fundamental classical phenomenological equations that describe the precession of the net magnetic moment in a static magnetic field. Given enough time, **M** will reach an equilibrium, given by

$$M_0 \approx \frac{B_0\gamma^2\hbar^2 N}{4kT} \quad 1.6$$

where N is the number of dipoles per unit volume and T is the temperature in kelvin.

Interaction with an RF Field

To generate signal in MRI, another magnetic field $\boldsymbol{B_1}$, perpendicular to $\boldsymbol{B_0}$ must first be applied at the precessional (Larmor) frequency of the magnetic moment. As this happens to lie in the radio frequency (RF) range, it is termed an RF field. Applying a $\boldsymbol{B_1}$ field to **M** tips **M** away from $\boldsymbol{B_0}$; the magnitude of this tip is defined as the flip angle (α), and is the integral of the envelope of $\boldsymbol{B_1}$ (B_1^e) over time:

$$\alpha = \gamma \int_0^t B_1^e(t)dt \qquad 1.7$$

The effect of applying a $\boldsymbol{B_1}$ field to **M** can be visualized in Figure 1.1. If we consider the main magnetic field, $\mathbf{B_0}$, to be along the z-axis (termed the longitudinal axis), applying $\mathbf{B_1}$ along the x-axis at a frequency ω_0 will cause **M** to appear to corkscrew down (Figure 1.1a) towards the x-y plane (the transverse plane). However, to better understand the effect of the $\mathbf{B_1}$ field, we can use the idea of the rotating reference frame. We can imagine that we are rotating at the Larmor frequency of **M**, and thus, all rotational affects around the z-axis are removed. In this reference frame, all corkscrew effects are removed, and application of an RF field on **M** will result in a simple rotation towards the transverse plane: this is referred to as nutation. For ease, all further terminology will be described in the rotating reference frame.

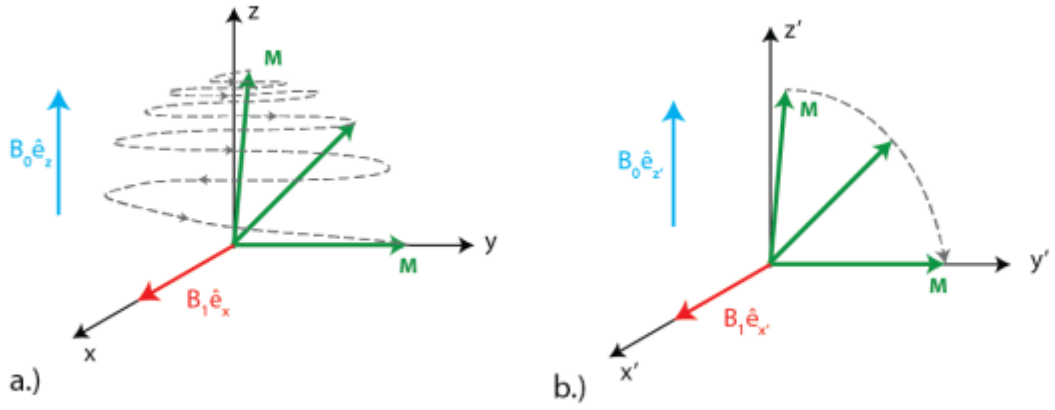

Figure 1.1. The effect of a $\mathbf{B_1}$ pulse applied along $\hat{\boldsymbol{e}}_{\boldsymbol{x}}$ on a magnetic moment aligned with $\mathbf{B_0}$. In the laboratory frame (a.), the orientation of **M** follows a corkscrew pattern as it moves to the transverse plane. However, in the rotating frame (differentiated here by the axes labeled [x',y',z']) with rotational frequency $\boldsymbol{\omega_0}$, **M** effectively tips away from $\mathbf{B_0}$ towards the transverse plane in a straight line.

Now that the magnetization has been rotated away from $\mathbf{B_0}$ it will form a measureable transverse magnetization. In the lab frame, this transverse magnetic moment will precess about the z-axis at the Larmor frequency. This bulk magnetization can be observed by utilizing Faraday's Law of

induction, which states that a current will be induced in a closed loop when in the presence of a changing magnetic flux oriented perpendicular to the plane of the loop:

$$\epsilon = -\frac{\partial \Phi}{\partial t} \qquad 1.8$$

where ϵ is the induced electromotive force and Φ is the magnetic flux.

Relaxation

So far, we've manipulated **M** as if it were a constant, without other forces acting upon it – besides $\mathbf{B_1}$ – however, in practice this is not the case. There are thermal processes that will tend to restore **M** back to the Boltzmann equilibrium state (aligned with the main magnetic field $\mathbf{B_0}$). These processes are random, and will result in random fluctuations in the local magnetic field; this will in turn modulate the local magnetic field experienced by the individual magnetic moments. The component of these random fluctuations that occurs at (or twice) the Larmor frequency is efficient at stimulating recovery of **M** back to the thermal equilibrium state. Decay of the transverse signal also occurs through spin-spin relaxation, which is sensitive to low-frequency random fluctuations in the local magnetic field.

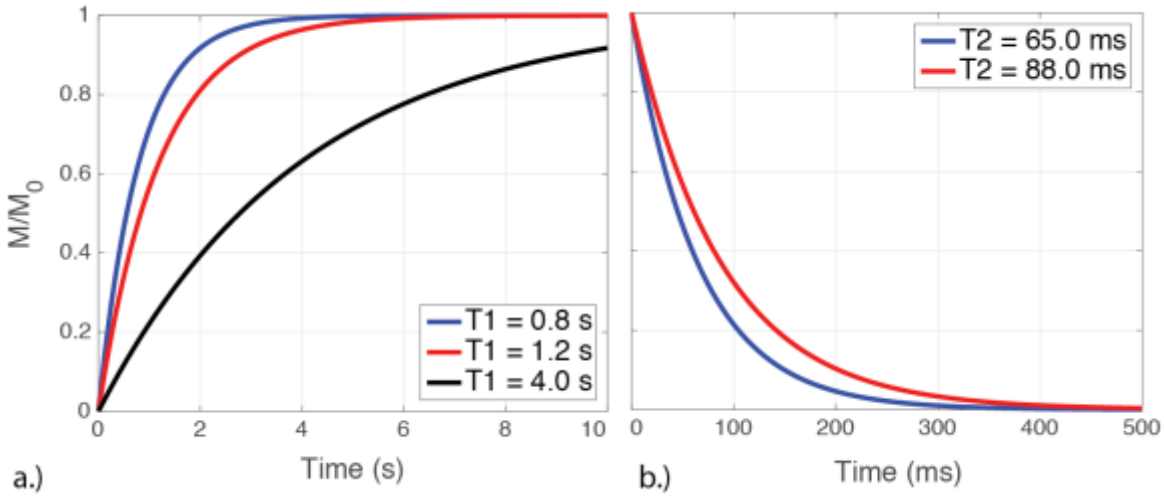

Figure 1.2. (a.) Recovery of longitudinal magnetization following a 90˚ pulse for white matter (blue, T_1 = 0.8 s), grey matter (red, T_1 = 1.2 s), and CSF (black, T_1= 4 s). Immediately after a 90˚ pulse, M = 0, and magnetization will regrow with relaxation time T_1. (b.) Dephasing of the transverse magnetization after a 90˚ pulse for white matter (blue, T_2 = 65 ms) and grey matter (red, T_2 = 88 ms). Initially, all of the spins are in phase, but will lose coherence with relaxation time T_2. Note that T_1 and T_2 values are taken from the literature at 3.0T (58), and the plots were created from simulations of Equations **1.9** and **1.10**.

After application of an RF field, the tipped magnetization will return to its equilibrium state by dissipating energy to the surrounding protons. As this process includes recovery of the z-component of **M** (see Figure 1.2a) it has been termed longitudinal relaxation and is governed by the relaxation constant T_1:

$$M_z(t) = M_0\left(1 - e^{-t/T_1}\right) \qquad 1.9$$

The transverse magnetic moment decays due to perturbations in the magnetic field due to random field fluctuations, dipole-dipole interactions, and exchange processes, which causes the transverse component of **M**, M_{xy}, to begin to lose coherence (see Figure 1.2b). Therefore, this process is called transverse relaxation, and is governed by the relaxation constant T_2:

$$M_{xy}(t) = M_0 e^{-\frac{t}{T_2}} \qquad 1.10$$

Combining both precession and relaxation into a single equation provides us with the seminal theory behind MRI: the Bloch Equations:

$$\frac{d\boldsymbol{M}}{dt} = \begin{bmatrix} -\frac{1}{T_2} & \gamma B_0 & 0 \\ -\gamma B_0 & -\frac{1}{T_2} & 0 \\ 0 & 0 & -\frac{1}{T_1} \end{bmatrix} \boldsymbol{M} + \begin{bmatrix} 0 \\ 0 \\ \frac{M_0}{T_1} \end{bmatrix} \quad 1.11$$

While T_2 is generally used describe transverse relaxation, the observed signal after a 90 degree RF pulse decays more rapidly than T_2. This is due to the fact that although we assume the main B_0 field is homogeneous, local variations due to susceptibility of the different tissues within a sample cause this signal to decay faster than T_2. This relaxation, called T_2*, is a combination of both spin-spin interactions (T_2) and inhomogeneities in the static field (T_2'):

$$\frac{1}{T_2^*} = \frac{1}{T_2} + \frac{1}{T_2'} \quad 1.12$$

Pure T_2 contrast can actually be obtained when a spin echo experiment is performed. Spin echo experiments refocus the static field inhomogeneities by employing a 180˚ refocusing pulse, and, thus, the signal intensity will decay as a function of T_2, similar to that shown originally in Equation 1.10. However, when using a gradient echo sequence – such as are the majority of the pulse sequences used in this dissertation – no refocusing pulse is used, and therefore the signal will decay with T_2*.

Acquiring an Image with NMR

Although we have described how to create an observable MR signal, we haven't described how these signals can be manipulated to create an image. Imagine we apply an RF pulse to a sample with frequency ω_0. The receiver coil that measures the resulting signal fluctuations will report a sinusoidal signal exponentially decaying with constant T_2*, and is called free induction decay (FID). If this sample consisted of a single proton moiety, the FID will be a single frequency oscillation at ω_o decaying with a single T_2* decay constant. However, if there are many protons in different environments in this sample, the FID will be a sum of all of these signals at all spatial locations. The spatial frequency dependence of these signals and their intensity is related by the Fourier transform. We can therefore write the signal of our MRI experiment as the contribution of the proton densities distributed in the volume:

$$S = \iiint_{Vol} \rho(x,y,z)dxdydz \tag{1.13}$$

Therefore, in order to gain spatial information about these different signals, we must apply linear magnetic field gradients to the sample to encode their frequency information in space. Varying these gradients over time will allow us to "sweep" our frequency space, building a map of our Fourier space (or k-space):

$$\begin{aligned} S(k_x,k_y,k_z) &= \iiint_{Vol} \rho(x,y,z)e^{-i2\pi(k_x x+k_y y+k_z z)}dxdydz \\ &= \mathcal{F}[\rho(x,y,z)](k_x,k_y,k_z) \end{aligned} \tag{1.14}$$

where k_x, k_y, and k_z are the areas of the gradient wave forms multiplied by γ. Once a frequency map S has been constructed, the inverse Fourier transform can be applied to give a 3D image of the bulk proton signal over the sample.

1.2.3. Magnetization Transfer Theory

While the previous section describes basic MRI theory, these are not the sole methods to elicit contrast from tissue. Magnetization Transfer (MT), the focus of this dissertation, has been developed to observe the exchange of information between bulk water and the surrounding tissue, as was qualitatively described in Section 1.2.1. To summarize, the MT effect is a phenomenon where proton spins residing in two (or more) magnetic environments transfer their spin information either through space (magnetic dipole exchange) (54) or physically (direct chemical exchange) (55). While this phenomenon occurs continuously, it can be exploited in an NMR environment to cause a visible attenuation in the observable signal by perturbing the system away from equilibrium. The MT effect is an umbrella term and generally thought to arise from the transfer of spin information from rotationally immobile protons, such as those found in semi-solid tissues or bound to macromolecules, to bulk water protons. Additionally, as these immobile proton species are rotationally restricted, their T_2 relaxation times occur on the order of microseconds and thus cannot be directly imaged using conventional MR methods (as data collection is on the order of milliseconds). However, due to this exchange of information, the semi-solid protons can be imaged indirectly through the MT effect.

The MT effect has been exploited in many different ways in MRI imaging (1,18,33,59-61). However, the focus of this dissertation incorporates using off-resonance (with respect to water) selective saturation of the semi-solid tissue to measure the MT effect. Selective saturation is made possible by the difference in line widths between the free water and semi-solid tissues: the line width is generally characterized as $1/T_2$. Thus, the much shorter T_2 in the semi-solid tissue will correspond to a line width much more broad than that of the free water, and which can therefore be selectively saturated. This selective saturation of the semi-solid tissue will then be transferred to the water pool through the MT effect, and will induce an appropriate signal decrease when imaged with normal imaging methods. This technique is similar to the saturation transfer experiments that have been performed in NMR (55).

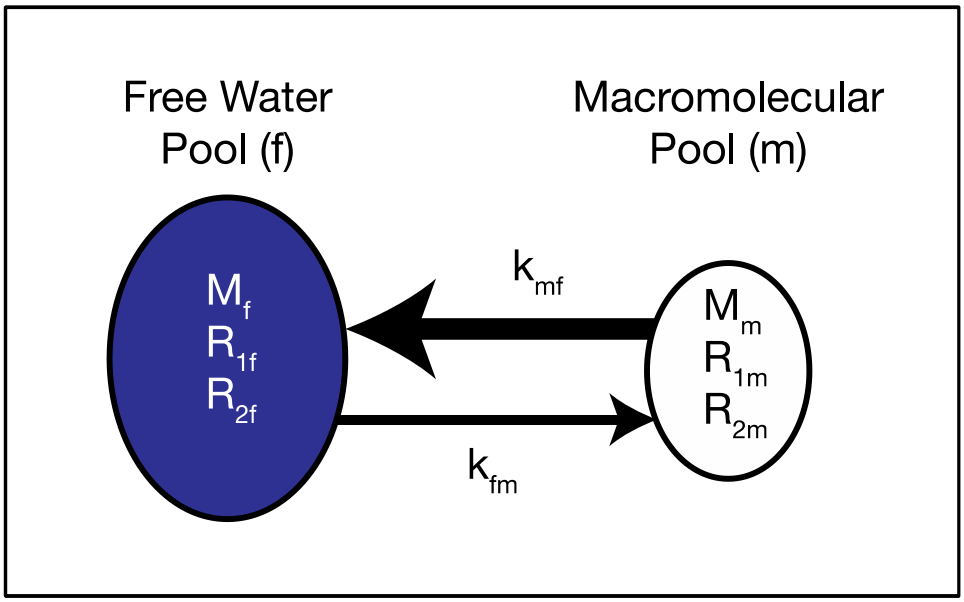

Figure 1.3. Two-pool model system describing exchange between the free water and a macromolecular pool. M is the pool size in each pool, R_1 and R_2 are the longitudinal and transverse relaxation constants in each pool, and k_{mf} and k_{fm} are the exchange rates between the (m) and (f) pools, and vice versa, respectively.

The Bloch-McConnell Equations

Due to the exchange of RF information between these different proton environments, the simple Bloch equations (Equation 1.11) are no longer sufficient to describe the interactions occurring between these two environments, as well as their implications for observed signal changes after application of RF irradiation. Therefore, a new model, first proposed by McConnell (52), and

further refined (1,18,19,34-36,60,62-64) since, has been developed to represent exchange-related MRI relatively accurately. Additionally, although the exchange dynamics between the water and semi-solid pool are much more complex, in practice it has been shown that a two-pool model (Figure 1.3) is well-suited to model the behavior between the semi-solid (referred to as the macromolecular pool, m) and the water (referred to as the free pool, f). The two-pool Bloch equations with exchange are (34):

$$\frac{d\boldsymbol{M}}{dt} = \begin{bmatrix} -\frac{1}{T_{2f}} & -\Delta\omega & 0 & 0 & 0 & 0 \\ \Delta\omega & -\frac{1}{T_{2f}} & 0 & 0 & -\omega_1 & 0 \\ 0 & 0 & -\frac{1}{T_{2m}} & -\Delta\omega & 0 & 0 \\ 0 & 0 & \Delta\omega & -\frac{1}{T_{2m}} & 0 & -\omega_1 \\ 0 & \omega_1 & 0 & 0 & -(R_{1f}+k_{fm}) & k_{mf} \\ 0 & 0 & 0 & \omega_1 & k_{fm} & -(R_{1m}+k_{fm}) \end{bmatrix} \boldsymbol{M} + \begin{bmatrix} 0 \\ 0 \\ 0 \\ 0 \\ R_{1f}M_0^f \\ R_{1m}M_0^m \end{bmatrix} \quad 1.15$$

where **M** is the magnetization components of the free and macromolecular spins (where $\boldsymbol{M} = \left[M_x^f, M_y^f, M_x^m, M_y^m, M_z^f, M_z^m\right]$), $T_{2f,m}$ are the transverse relaxation time constants of each pool (free and macromolecular, respectively), $R_{1f,m}$ are the longitudinal rate constants (defined as $R_1 = 1/T_1$) for each pool, $\Delta\omega$ is the RF pulse offset with respect to water in hertz, ω_1 is the amplitude of an RF pulse, $M_0^{f,m}$ is the equilibrium concentration of spins in each pool, and k_{fm} and k_{mf} are the exchange rates from the free to the macromolecular pool, and vice versa, multiplied by the size of the bound and free pools, respectively. Additionally, the exchange rates are related via mass balance by (65):

$$k_{fm} = \frac{M_0^m}{M_0^f} k_{mf} \quad 1.16$$

While Equation 1.15 will model the evolution of magnetization under two-pool exchange quite effectively, the very short T_2 relaxation time in the macromolecular pool will destroy any transverse coherence between the two pools very rapidly, therefore, it is more convenient to model all transverse contributions in the macromolecular pool as a set of line shapes (53,66,67). Additionally, because the free water pool is much larger than the macromolecular pool, M_0^f is generally set to 1 to normalize the experiment. Thus, we can reduce Equation 1.15 to:

$$\frac{d\boldsymbol{M}}{dt} = \begin{bmatrix} -\frac{1}{T_{2f}} & -\Delta\omega & 0 & 0 & 0 & 0 \\ \Delta\omega & -\frac{1}{T_{2f}} & 0 & 0 & -\omega_1 & 0 \\ 0 & \omega_1 & 0 & 0 & -(R_{1f} + k_{fm}) & k_{mf} \\ 0 & 0 & 0 & 0 & k_{fm} & -(R_{1m} + k_{fm} + R_{rfm}) \end{bmatrix} \boldsymbol{M} + \begin{bmatrix} 0 \\ 0 \\ R_{1f} \\ R_{1m} * PSR \end{bmatrix} \quad 1.17$$

where PSR = M_0^m / M_0^f, and R_{rfm} is the RF saturation rate for the macromolecular pool, and can be defined as:

$$R_{rfm} = \pi\gamma^2 B_1^2 g_m(\Delta\omega, T_2^m) \quad 1.18$$

where g_m is the line shape for the macromolecular pool for a given offset ($\Delta\omega$) and T_2. It has been shown that, while a Lorentzian line shape is adequate to model the free pool, a Lorentzian cannot be used to model the macromolecular pool due to the partially ordered nature of tissue; instead a super-Lorentzian line shape has been shown to adequately model the absorption line shape for the macromolecular pool in living nervous system tissue (3,19,68):

$$g(\Delta\omega, T_2^m) = \sqrt{\frac{2}{\pi}} \int_0^{\frac{\pi}{2}} \frac{T_2^m}{|3\cos^2\theta - 1|} \exp\left(-2\left(\frac{2\pi\Delta\omega T_2^m}{3cos^2\theta - 1}\right)^2\right) \sin\theta \, d\theta \quad 1.19$$

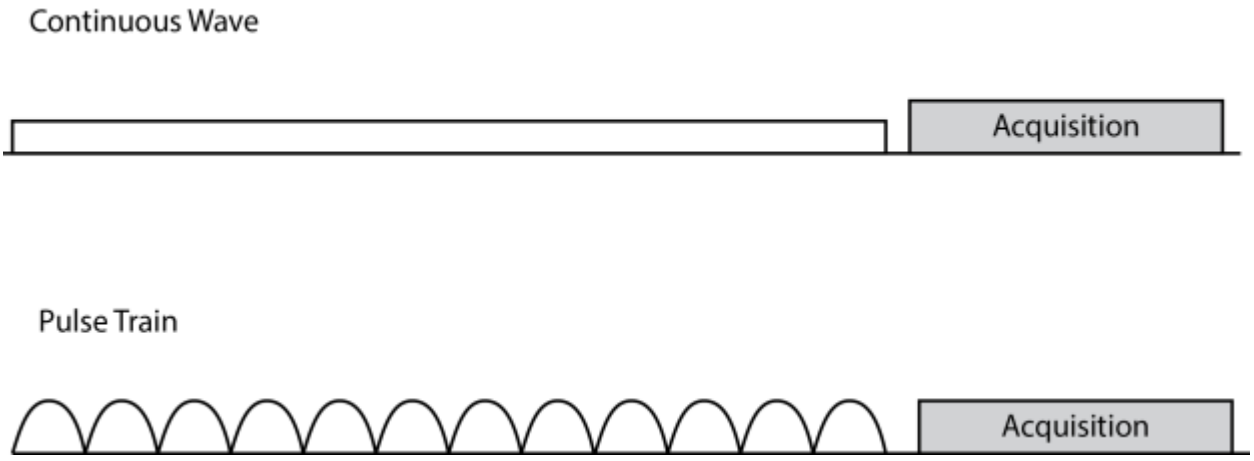

Figure 1.4. An example of a CW vs a pulse train acquisition. In a CW experiment, a long, hard RF pulse is played out over several seconds to saturate the macromolecular pool. Conversely, a pulse train uses a series of smaller, shaped RF pulses to achieve the same result. A pulsed experiment uses one or a few saturation pulses combined with an SPGR acquisition in order to build up to a steady state over several acquisitions.

MT Imaging in vivo

While the above equations describe how to effectively model the MT effect, they do not describe how to acquire the data that will be applied to this model. There are two main types of off-resonance MT experiments: Continuous wave (CW) and pulse train, shown visually in Figure 1.4. In a CW experiment, a long (on the order of seconds) saturation pulse is played out at various B_1 amplitudes and offset frequencies to saturate the macromolecular pool; this saturation will then be transferred between each pool. Applying a long, off-resonance pre-pulse is done with the purpose of establishing a steady state condition between the two pools, where the exchange rates have formed equilibrium saturation between the water and semi-solid pools that will remain constant even if more RF irradiation is applied. However, while CW pulses will provide robust MT contrast, they are plagued by several factors that limit their deployment in vivo. First, CW RF amplifiers are not widely available in clinically utilizable systems. Second, they also require large power deposition, which is useful in the NMR domain, but quickly runs into safety issues when applied in vivo. Third, while the advent of solid state amplifiers has decreased time required to reach full power, solid state amplifiers are also susceptible to "drooping," or a decrease in RF power from what is prescribed. This phenomenon has been seen to occur in as little as 100 ms, which prevents the long saturation pulses necessary in CW imaging from being employed in modern systems. Last, but most importantly, they cannot efficiently cover a large,

3D volume effectively. Indeed, it takes approximately 20 minutes to perform a CW experiment for minimal brain coverage at 1 offset frequency (69,70). To remove these barriers to imaging in vivo, a pulse or series of pulses at a low duty cycle can be played out to saturate the solid pool (35); the water is then imaged using conventional pulse sequences.

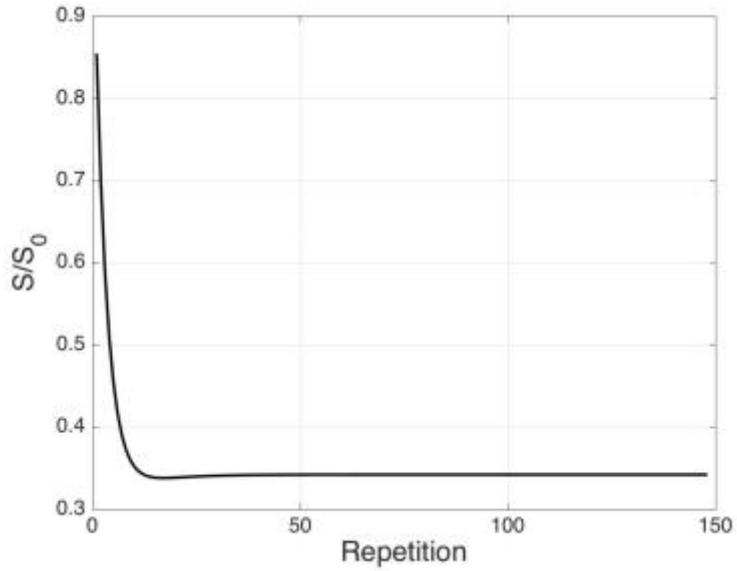

Figure 1.5. A simulation of the approach to steady state for an example data set. The normalized signal rapidly drops away from its equilibrium value, and reaches steady state after approximately 40 repetitions. Figure created using simulations from Equation **1.17**.

A more recent development involves the use of short pulses (around 10-40 ms) combined with a spoiled gradient recalled echo (SPGR) sequence to provide MT contrast (35,71). Thus, instead of creating a steady state condition by using a long CW or pulse train, a smaller set (down to a single pulse) of pulses are played out, after which one of more lines of k-space is acquired. This method utilizes the idea that the saturation created from the MT pulse will create more saturation than the longitudinal relaxation can regrow. A typical acquisition matrix for a reasonable resolution is around 150 – 200 pulses. However, as can be seen from the simulations in Figure 1.5, this condition is reached in only 40 repetitions, but depends on T_1, the repetition time (TR), and B_1 of the saturation. Thus, instead of needing to build up to a steady state before each pulse, and shortening the acquisition time by employing fast imaging methods, a steady state can be allowed to build up over several TR's. So long as steady state is achieved by the time

the k0 line of k-space is acquired, the contrast will be similar to that seen in a long pulse train. This greatly reduces the scan time required to perform MT imaging, and thus provides an opportunity to apply these pulses to large volumes in a much shorter scan time than can be achieved with a CW or a long pulse train.

However, because performing the MT experiment at enough offsets and RF irradiation powers to effectively utilize the model from Equation 1.17 would require a significant amount of time, the magnetization transfer ratio (MTR), developed by Wolff and Balaban (33), is typically used to quickly quantify the MT effect:

$$MTR = 1 - \frac{S(\Delta\omega)}{S_0} \qquad 1.20$$

where $S(\Delta\omega)$ and S_0 are the signals acquired with and without an RF irradiation at offset $\Delta\omega$, respectively. The MTR has been shown to relate to white matter myelin density in the nervous system (2,13,72). Unfortunately, research has shown that the MT effect is only semi-quantitatively characterized via the MTR, being sensitive to pulse sequence design, as well as B_1 and B_0 inhomogeneities (6) and other non-MT-specific NMR parameters (34,73).

If data are acquired over several offsets and RF irradiation powers, the normalized signal, $S(\Delta\omega)/S_0$, can be plotted as a function of offset, forming a so-called Z-spectrum (Figure 1.6). A quantitative model, such as the two-pool model in Equation 1.17, can then be applied to this data to estimate the model parameters over different tissue types, and as well as correct some of the sensitivities inherent in the MTR (36,38,73-75).

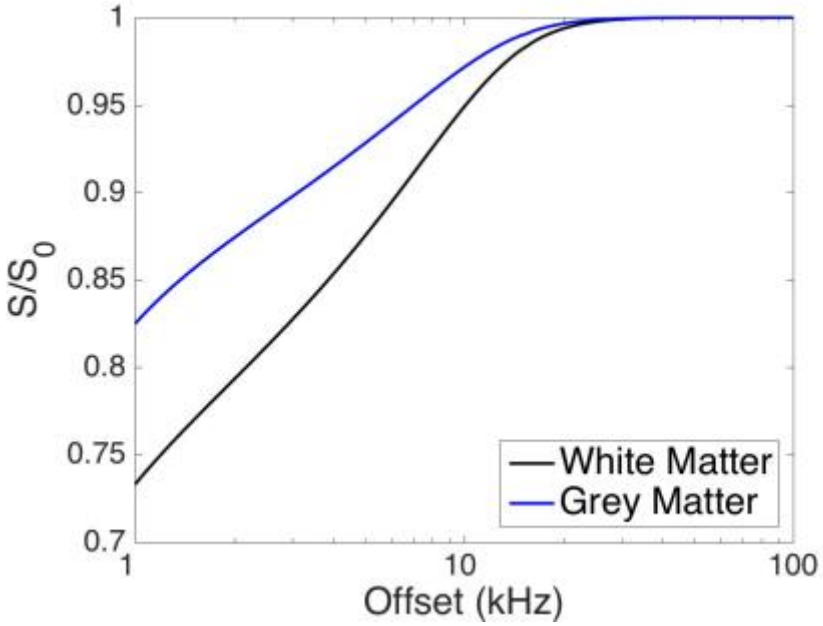

Figure 1.6. Example Z-spectra for white matter (red) and grey matter (blue). As the saturation pulse moves further away from the water resonance (the x-axis), the MT effect diminishes until it has no effect (around 100 kHz). Additionally, the MT effect is reduced for tissues with smaller semisolid components, such as in grey matter. Figure created using simulations from Equation **1.17**.

A Simplified Model

One model that has seen widespread use since its inception (37,76-81) is Yarnykh's model (78,82) of quantitative magnetization transfer (qMT) for pulsed SPGR. This models the pulsed SPGR sequence detailed above, and assumes that the direct effect on the free pool is negligible due to high offset frequency and low saturation pulse power, and that the sequence is ideally spoiled (83). The pulse sequence is then split into four distinct evolution periods, defined as the off-resonance saturation, spoiling, readout pulse, and relaxation. Using these assumptions, the pulsed steady state magnetization (which is a solution to Equation 1.17 for an SPGR acquisition) is defined as (82):

$$\boldsymbol{M_z} = (\boldsymbol{I} - \boldsymbol{E_s}\boldsymbol{E_m}\boldsymbol{E_r}\boldsymbol{C})^{-1}\{[\boldsymbol{E_s}\boldsymbol{E_m}(\boldsymbol{I} - \boldsymbol{E_r}) + (\boldsymbol{I} - \boldsymbol{E_s})]\boldsymbol{M_{eq}} + \boldsymbol{E_s}(\boldsymbol{I} - \boldsymbol{E_m})\boldsymbol{M_{ss}}\} \qquad 1.21$$

where $\mathbf{M}_{eq}$ and $\mathbf{M}_{ss}$ are the vectors of equilibrium and steady state longitudinal magnetization, $\mathbf{I}$ is the unit matrix, $\boldsymbol{C} = diag(\cos(\alpha), 1)$, which corresponds to an instantaneous rotation of M_z^f by an RF irradiation of flip angle α, $\boldsymbol{E_m} = \exp\big((\boldsymbol{R} + \boldsymbol{W})t_m\big)$ describes off-resonance saturation with a duration t_m, and the terms $\boldsymbol{E_r} = \exp(\boldsymbol{R}t_r)$, and $\boldsymbol{E_s} = \exp(\boldsymbol{R}t_s)$ describe relaxation during

the delays before (t_s) and after (t_r) the RF irradiation. The vectors $\mathbf{M}_{eq}$ and $\mathbf{M}_{ss}$, as well as **R** and **W**, are defined as follows:

$$\boldsymbol{M_{eq}} = \begin{bmatrix} 1 - MPF \\ MPF \end{bmatrix} \tag{1.22}$$

$$\boldsymbol{M_{ss}} = \frac{1}{D}\begin{bmatrix} (1 - MPF)\left(A + R_1^f R_{rfm}\right) \\ MPF\left(A + R_1^m R_{rff}\right) \end{bmatrix} \tag{1.23}$$

$$\boldsymbol{R} = \begin{bmatrix} -R_1^f - k_{fm} & k_{mf} \\ k_{fm} & -R_1^m - k_{mf} \end{bmatrix} \tag{1.24}$$

$$\boldsymbol{W} = -diag\left(R_{rff}, R_{rfm}\right) \tag{1.25}$$

where

$$A = R_1^f R_1^m + R_1^f k_{mf} + R_1^m k_{fm} \tag{1.26}$$

$$D = A + \left(R_1^f + k_{fm}\right)R_{rfm} + \left(R_1^m + k_{mf}\right)R_{rff} + R_{rff}R_{rfm} \tag{1.27}$$

The MPF is defined as the macromolecular pool fraction, and is expressed as:

$$\begin{aligned} MPF &= \frac{M_0^m}{M_0^m + M_0^f} \\ &= \frac{PSR}{1 + PSR} \end{aligned} \tag{1.28}$$

and R_{rff} and R_{rfm} are the effective saturation rates of the pools, where the free pool is modeled as a Lorentzian, while the macromolecular pool is defined as a super-Lorentzian.

This model is the solution of Equation 1.17 for an SPGR acquisition, and can thus be solved much more rapidly than the full model. Additionally, several iterations of this model have been developed which have decreased the number of independent MT observations in order to reduce scan time (37,79,82) to create a clinically viable qMT model. This was done by experimentally determining a set of constraints for most of the parameter estimates in this model, leaving the PSR as the only free parameter (37). Creating a robust, clinically relevant set of constraints to reduce scan time using Yarnykh's model is explored in more detail in Chapter 3 and Chapter 4.

CEST

Chemical exchange saturation transfer (CEST) imaging is a type of off-resonance saturation transfer imaging that relies on spectrally selective RF irradiation and exploiting a specific

exchange phenomenon. Similar to an MT experiment, CEST relies on the direct chemical exchange of protons between small, mobile solutes and water (rather than dipole-dipole exchange and spin diffusion). These small mobile solutes have protons that resonate at a frequency different from the bulk water protons (yet much closer to water than the bulk macromolecular spins), and thus can be selectively saturated using RF irradiation. This saturation will subsequently be transferred by direct chemical exchange, resulting in an attenuation of the water signal, similar to what is observed in an MT experiment (84).

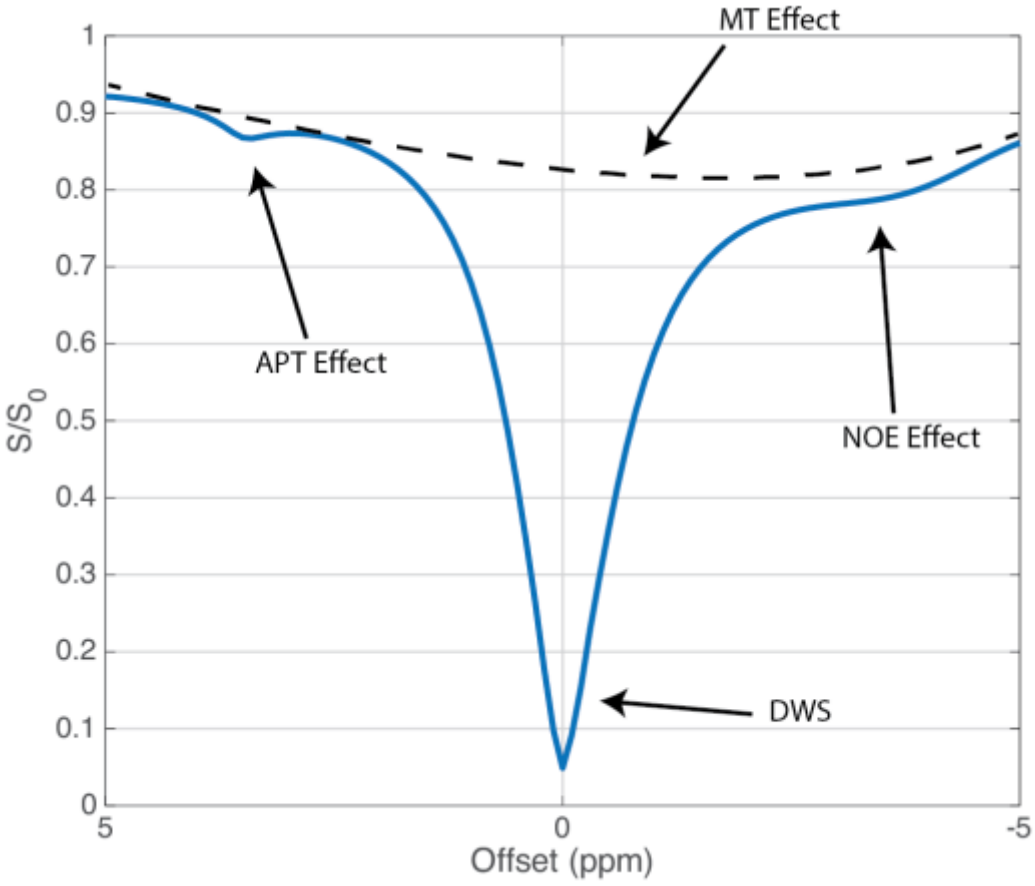

Figure 1.7. Sample CEST Z-spectrum. 0 ppm is assigned to water (as opposed to 4.75 ppm in NMR) to take advantage of the symmetry of direct water saturation. Additionally, an APT effect (centered at 3.5 ppm), MT effect, and an NOE effect (centered at -4 ppm) are present in this spectrum. Figure created using simulations based upon Equation **1.31**.

The effects of this saturation can be visualized similarly to MT as a Z-spectrum (Figure 1.7), with water centered at 0 ppm. Exchangeable protons downfield (higher frequency) from water are produced from endogenous hydroxyls, amides, and amines when they are saturated at appropriate RF power, while nuclear Overhauser enhancement (NOE) effects contribute to the contrast upfield (lower frequency) from water. Additionally, the MT effect confounds the entire spectrum due to its spectrally broad lineshape. Additionally, it is important to note that these mobile solutes have a saturation efficiency that can be defined as (85-87):

$$\alpha_{eff} \approx \frac{(\gamma B_1)^2}{(\gamma B_1)^2 + k_{sw}^2} \qquad 1.29$$

where γ is the gyromagnetic ratio, B_1 is the RF irradiation power of the saturation pulse, and k_{sw} is the exchange rate from the solute to bulk water. Therefore, rapidly exchangeable protons can only be saturated efficiently by applying more RF power, which is disadvantageous in vivo due to specific absorption rate (SAR) requirements. Therefore, in order to efficiently selectively saturate solute protons, the CEST often relies on the condition of slow exchange ($\Delta\omega >> k_{sw}$) on the MR time scale to be fulfilled, and the solute of interest must be present at a detectable concentration (84) (millimolar range). This situation is still favorable when studying amide protons in peptides and small tissue proteins, as they have relatively slow exchange and high concentrations (on the order of 1% of bulk water content) (86,88), however, amines and hydroxyls have much faster exchange rates, and are therefore, difficult to measure under normal clinical conditions (89).

Of particular clinical interest are endogenous CEST agents such as amide proteins on mobile proteins/peptides, which may relate to changes in protein concentrations and pH as seen in MS and other demyelinating diseases through protein accumulation in normal appearing white matter. This amide proton transfer (APT) CEST imaging (88,90-92) has shown sensitivity to pH and protein concentration in stroke (93) and cancer (94-96).

Most current research methods employ the MTR_{asym} to analyze CEST data (97):

$$MTR_{asym}(\Delta\omega) = MTR(\Delta\omega) - MTR(-\Delta\omega) = \frac{S(-\Delta\omega) - S(\Delta\omega)}{S_0} \qquad 1.30$$

Where S is the observed signal at each frequency offset, and S_0 is a reference measurement (in the absence of RF irradiation). This model works well because it requires only three independent CEST measurements, allowing for clinical deployment of the method. However, it also assumes

that all contributing exchange save for the CEST effect being studied are symmetric about 0 ppm, which is often incorrect, particularly in vivo (as can be seen in Figure 1.7). In addition to the CEST effect seen upfield of water, NOE effects can be found downfield. These effects are due to several different exchange mechanisms. Exchange-relayed intramolecular NOEs occur when saturation is transferred from the backbone of aliphatic protons through amides, amines, and hydroxyls to water. Direct intramolecular NOE also arise from direct exchange of the aliphatic protons with water (84). MT contrast is also particularly apparent due to the broad macromolecular resonances MT is composed of, as well as the high concentration of semi-solid tissues in vivo. Furthermore, MT is asymmetric with respect to water (at -2.34 ppm), which will bias MTR_{asym} measurements (90). MT effects will also increase with increasing RF irradiation amplitude, preventing higher powers from being used effectively to measure CEST effects with MTR_{asym} (40). Therefore, more sophisticated models that account for some (or all) of these effects must to be considered.

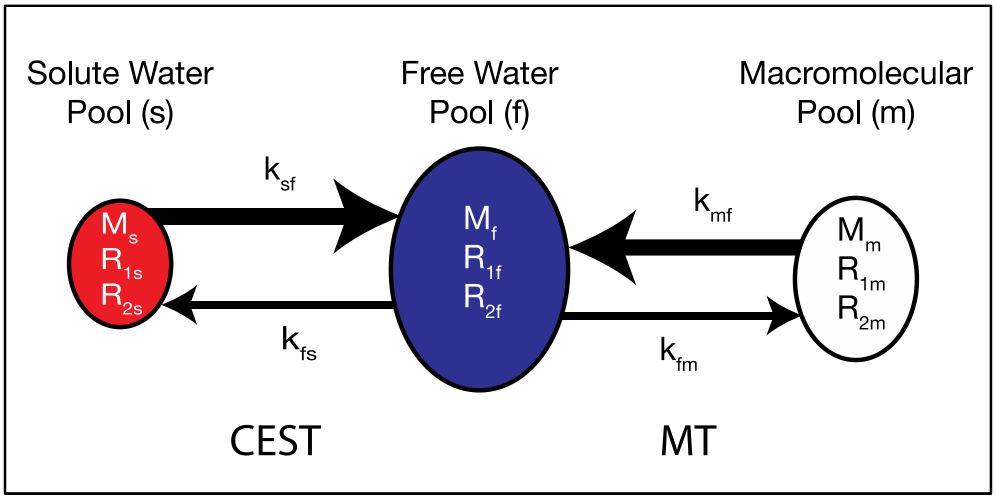

Figure 1.8. Three-pool model system describing exchange between free water (f) with a macromolecular pool (m), and free water with a solute pool (s). The (s) and (m) pools are independent of one another, occur simultaneously and constantly, and will exchange their information with the (f) pool only. Exchange with the (s) pool constitutes CEST, while exchange with the (m) pool consists of MT.

Like MT, CEST can be modeled by the Bloch-McConnell equations (40). In order to model exchange with a single CEST agent, such as amides, a separate solute pool (s) will be created that will be in exchange with water (Figure 1.8). The evolution of the magnetization between these

two pools can be modeled similar to Equation 1.15, with a small modification to the transverse magnetization:

$$\frac{d\boldsymbol{M}}{dt} = \begin{bmatrix} -\frac{1}{T_{2f}} & -\Delta\omega & 0 & 0 & 0 & 0 \\ \Delta\omega & -\frac{1}{T_{2f}} & 0 & 0 & -\omega_1 & 0 \\ 0 & 0 & -\frac{1}{T_{2s}} & -(\Delta\omega - \Delta\omega_s) & 0 & 0 \\ 0 & 0 & \Delta\omega - \Delta\omega_s & -\frac{1}{T_{2s}} & 0 & -\omega_1 \\ 0 & \omega_1 & 0 & 0 & -(R_{1f} + k_{fs}) & k_{sf} \\ 0 & 0 & 0 & \omega_1 & k_{fs} & -(R_{1s} + k_{fs}) \end{bmatrix} \boldsymbol{M} + \begin{bmatrix} 0 \\ 0 \\ 0 \\ 0 \\ R_{1f}M_0^f \\ R_{1m}M_0^s \end{bmatrix} \quad 1.31$$

where $\Delta\omega_s$ is the offset between the solute of interest and water, and the subscript *s* represents the solute pool. This can be further expanded by adding additional pools for different solutes, as well as the MT pool (see Figure 1.8), similar to that shown in Equation 1.17. However, adding more pools will complicate the model, as this will require more independent observations in order to properly estimate all of the parameters. Importantly, modeling the MT effect in the CEST domain necessitates including the MT asymmetry in the model, which was not shown in Equation 1.17.

While CEST can be effectively modeled by the Bloch-McConnell equations (40), successfully incorporating every source of saturation transfer into these equations makes this method of calculation increasingly complex and computationally intensive. However, it has been shown that direct water saturation (DWS) can be modeled using a Lorentzian lineshape (98,99) convolved with the pulse parameters of interest. Therefore, in a CEST experiment, it can be assumed that any deviation from a Lorentzian is caused by saturation other than water, avoiding the problems associated with the MTR_{asym}. Jones et al. (43) used low RF power to minimize MT contributions, and measured the mean Lorentzian difference from 3.3-3.7 ppm (the frequency shift associated with APT contrast) to study CEST effects in white and grey matter. They found that the MTR_{asym} and the Lorentzian difference analysis differed greatly, due to the presence of NOE effects upfield from water. Zaiss et al (42,45) created a multi-Lorentzian model which has allowed them to simultaneously map several different parameters at 7T. They were able to show that their new AREX mapping could fit the CEST and NOE effects without confounds due to the MT effect, and were able to apply this technique to image human glioblastoma (42) and acute

stroke in mice (45). However, the authors state that the AREX method can only be applied at high field strengths, and thus, cannot be utilized at 3T. In conclusion, Lorentzian models present a strong alternative to MTR_{asym} for analyzing CEST data. Utilizing these types of models to fit the MT component in CEST imaging is explored more in Chapter 6.

1.3. Clinical Significance of MT

1.3.1. The role of MT Imaging in the CNS

To fully understand the significance of these MT techniques, it is important to understand how these techniques have been employed to investigate pathology, particularly in the CNS. In the CNS, white matter is the primary target of MT, due the abundance of myelin in these tissues. Briefly, myelin is a lipid-protein lamellar membranous structure that envelopes the axons in the central and peripheral nervous system. Myelin in the CNS is produced by oligodendrocytes, which are wrapped around the axon in a concentric lamellar fashion. These axons are focally unmyelinated at regular intervals, forming nodes of Ranvier: these nodes and the myelin between them allow for signals in white matter to be relayed across the axon much more rapidly than could be achieved without them (about 10 to 100 times that of an unmyelinated axon). This speed is critical to allow the complex sensory, motor, and behavioral functions found in most vertebrates to occur (12). Additionally, studies have shown that myelin also helps regulate axonal transport (100), maintain axonal integrity (101-103), regulate pH (104), as well as to maintain fluid volume and ion composition (105). Thus, the integrity of myelin is of critical importance to maintaining neurological function. Unfortunately, diseases such as MS create areas of focal and diffuse edema, inflammation, demyelination, and axonal loss (106). However, the underlying mechanisms of this pathology are poorly understood, and current conventional MRI imaging techniques have difficulty identifying demyelination before it is widespread. Thus, much of the pioneering work in MT and imaging myelin in general has been with the goal of elucidating the disease processes associated with MS (12).

Several important studies have been published which demonstrate the importance of MT in imaging myelin. van Waesberghe, et al. (107) compared MTR and T_1-weighted images to axonal and myelin density in 17 MS subjects immediately postmortem. They found that the MTR and T_1 contrast correlate strongly with axonal density in lesions, while MTR alone correlated

strongly with axonal density in NAWM. Schmierer, et al. (13) also found that MTR and T_1 contrast correlate strongly with myelin content in 20 subjects immediately postmortem. However, they also determined that the primary MR correlate of myelination appeared to be the MTR. These and other studies have shown repeatedly that MT holds promise to help unravel the underlying pathophysiology surrounding myelin and pathologies which affect myelin.

1.3.2. MS in the Spinal Cord and Optic Nerve

The SC is linked to many CNS diseases, and in MS, it is hypothesized that SC damage is responsible for the bulk of clinical deficits (108). The SC is less than one tenth the size of the brain, and thus a small, 3mm lesion in the brain would involve 20% of the SC, which would be the neurological equivalent of a 40mm lesion in the brain. Indeed, a 3mm SC lesion in a white matter column can result in complete loss of function from that column. In addition to the small size of the SC, white and grey matter MRI contrast is poor due to the similar relaxation times between these two tissues (58), preventing conventional imaging methods from identifying white matter lesions.

The optic nerve is equally an integral part of the CNS and is indicated in the earliest manifestations of diseases such as MS, but due to the challenges associated with imaging the optic nerve, there has been little radiological development in this region. These challenges include: 1) the optic nerve is even smaller than the SC (< 4 mm), 2) is directly superior to the maxillary sinuses, and 3) is surrounded by a layer of orbital fat. Clinically, the optic nerve is commonly affected by optic neuritis, a sudden inflammation of the optic nerve marked by pain during eye movement, as well as a decrease in visual acuity, color vision, contrast, and visual field defects (109). Optic neuritis is the presenting symptom in 17 – 25% of all MS cases, while nearly two thirds of MS patients will experience optic neuritis in their lifetimes, and 40-60% will have visual deficits localized to the optic nerve (110). However, despite the prevalence of optic nerve pathology in MS, no radiological biomarkers have been developed in the optic nerve that predict eventual development of MS.

Thus, a significant portion of this dissertation has been focused on developing techniques that can accurately determine the myelin content within the optic nerve and SC. The development of these techniques is fundamental to elucidating some of the disease processes

associated with MS and other demyelinating diseases that affect the entirety of the CNS, and may help provide a noninvasive way to diagnose and monitor disease progression. These techniques are explored in more detail in Chapter 2, Chapter 3, and Chapter 4.

1.4. Outline of Dissertation

The overall goal of this dissertation is to develop a set of quantitative tools to probe tissue microstructure by exploiting the MT effect. Advancing these methods of characterizing tissues using MT will be valuable for understanding the underlying tissue microstructure, as well as characterizing pathologies at clinical field strengths.

The sensitivity of the MT effect to different neurological tissues will first be explored through the use of new techniques in the optic nerve and SC. The optic nerve is a difficult tissue to image, due to the fatty connective tissue which surrounds the optic nerve, and exhibits markedly different MT properties than the nerve tissue. Therefore, the qMT imaging protocol is modified to utilize the Dixon fat-water separation method (111) to reduce the influence of fat, and the MT effect was quantified in the nerve, and is summarized in Chapter 2. Next, a single-point methodology is applied to the SC to acquire high-resolution qMT in a clinically reasonable scan time. This protocol is developed in a healthy cohort (Chapter 3), then applied to a cohort of patients with MS to determine the sensitivity of these measures to MS-induced changes to white matter (Chapter 4). Lastly, this methodology is applied in the lumbar cord in controls to evaluate the sensitivity of this method over the entire spinal cord (Chapter 4).

The specificity of the MT effect to white matter is next evaluated. Recent experiments have demonstrated that white matter can be selectively highlighted using a set of pulse sequences sensitive to long fatty acid chains, such as those found in myelin (112,113). However, these sequences utilize a long (≈2 sec) pulse train to saturate the semisolid pool, and therefore, they can only apply this experiment in 2D. However, in this dissertation I have developed a method to utilize this technique in 3D, and show that this method is sensitive to white matter over the entirety of the brain (Chapter 5).

Once I have demonstrated an understanding of the sensitivity and specificity of the MT effect, I investigate how it affects the accuracy of a similar technique: CEST. I explore how to utilize the knowledge gained from previous chapters to remove the MT effect from a CEST

spectrum in order to more quantitatively evaluate both the CEST effect and effects due to aliphatic groups. This technique also presents more accurate values of the T_{2f} parameter, and thus provides more accurate qMT indices than have been acquired previously (Chapter 6).

Chapter 2: Incorporating Dixon Multi-Echo Fat Water Separation for Novel Quantitative Magnetization Transfer of the Human Optic Nerve In Vivo

Text for Chapter 2 adapted from:

Smith, AK, Dortch, RD, Dethrage, LM, Lyttle, BD, Kang, H, Welch EB, and Smith, SA. (2016). "Incorporating dixon multi-echo fat water separation for novel quantitative magnetization transfer of the human optic nerve in vivo." Magn Reson Med. Doi: http://dx.doi.org/10.1002/mrm.26164.

2.1. Introduction

The optic nerve (ON) is responsible for mediating visual information from the eyes to the optic chiasm and represents the sole pathway between the eyes and brain. The integrity of these nerves is imperative in maintaining visual function; consequently, diseases of the ON can have dramatic effects on daily function. One significant challenge in the management of patients with optic neuropathies (such as glaucoma, optic neuritis) has been the lack of robust, quantitative tools capable of characterizing the underlying pathophysiology. For example, conventional MRI scan contrasts, e.g. spin-density, T_1- and T_2-weighted, currently do not provide significant diagnostic (114) or prognostic value over conventional ophthalmologic exams in optic neuropathies.

Magnetization transfer (MT) imaging has emerged as an MRI technique capable of quantifying myelin density changes (2,13,72) brought about by neurodegenerative diseases affecting the brain, spinal cord, and peripheral nerves (38,115-123); it may therefore provide similar quantitative information in ON diseases. MT MRI exploits the fact that there are protons residing on immobile macromolecules in tissue in addition to the free water protons observed with conventional MRI (33). Conventional MRI cannot image these protons directly because their T_2 relaxation times are too short (≈10 μs) to be captured by typical readout schemes. However, these macromolecular protons communicate with the surrounding water and can be indirectly imaged by exploiting this exchange, which is referred to as the MT effect.

The contrast in an MT experiment is generated via application of a radiofrequency (RF) irradiation pulse at an offset frequency with respect to water ($\Delta\omega$) to selectively saturate the spectrally broad macromolecular proton resonance. This saturation is transferred to the free water pool via MT, resulting in an observed signal attenuation. The MT effect is semi-quantitatively characterized via the magnetization transfer ratio (MTR), which has been shown to correlate with myelin content (13). Unfortunately, the MTR is also sensitive to pulse sequence design, RF transmit field (B_1), and magnetic static field (B_0) inhomogeneity (6), as well as by tissue relaxation times and other non-MT-specific NMR parameters (34,73), limiting researchers and clinicians from creating a standard MTR metric to define pathology. To overcome some of these limitations and derive indices that are directly reflective of MT phenomena, quantitative MT (qMT) has been developed and implemented in the brain and spinal cord (36,73,74,76,78). qMT typically requires images to be acquired at multiple RF irradiation powers and/or frequency offsets, generating a so-called MT z-spectrum for each voxel (124). The resulting z-spectrum can be fit to a two (or more)-pool model to estimate quantitative indices, such as the pool size ratio (PSR), defined as the macromolecular pool size divided by the free pool size, the MT exchange rate from the macromolecular pool to the free pool (k_{mf}), and the transverse and longitudinal relaxation times for each pool (57,73). Often, the focus is on the PSR, as it has been shown to correlate well with white matter (WM) myelin density (13,125-127), and may offer a biomarker of demyelination and axonal loss in WM pathologies.

MT imaging of the ON, therefore, has the potential to report on microstructural changes preceding atrophy, potentially offering greater insight into changes that may persist after transient inflammation has subsided. Despite this promise, qMT applications in the ON have been limited to ex vivo studies (19,73), largely due to the technical challenges associated with quantitative imaging of the ON. First, qMT methods often require long scan times for accurate data fitting (37). The ON is approximately 3 mm in diameter (128), necessitating longer, higher-resolution scans for whole-nerve quantification. Short scan times are, however, often required for quantitative ON imaging, as eye fixation is advisable to reduce to impact of constant eye motion. Secondly, fatty connective tissue surrounds the ON and exhibits markedly different MT properties than nerve, requiring fat suppression techniques to accurately separate the nerve

from the surrounding anatomy. For conventional MRI, spectral fat suppression techniques, such as spectral presaturation with inversion recovery (SPIR) (129) or spectral attenuated inversion recovery (SPAIR) (130), are typically employed. Unfortunately, these approaches are often incompatible with qMT imaging because they are performed with an off-resonance pulse that can affect MT quantification. Short TI inversion recovery (STIR) methods have also been proposed (131), however, STIR results in significant water signal attenuation and a reduction in SNR. Lastly on-resonant fat suppression techniques such as binomial spatial-spectral excitation pulses can be applied, however, they require a large, 3-D field of view and increased gradient demands, which may not always be achievable in vivo.

We, therefore, propose a multi-echo Dixon fat-water separation approach (132-135) to remove the fat component from the MT images. The Dixon method takes advantage of the differences in precession rates between water and fat by acquiring data at multiple echo times to separate the fat and water components of the signal (111). While whole-brain fat and water images have been successfully implemented in slice locations that cover the ON (136), to the authors' knowledge, Dixon-separated qMT has not been studied. The importance of the work presented here is to evaluate the stability of qMT under multi-echo signal combinations and utilize this information to derive qMT indices reflective of myelination at resolutions that are typically prohibitive for qMT methods. Toward this end, we performed in vivo qMT in the brain and ON of healthy volunteers using a three-echo Dixon method, and evaluated this technique against traditional single-echo out-of-phase imaging data.

2.2. Methods

All numerical simulations and data analyses were performed with scripts written in MATLAB 2014a & 2015a (The MathWorks, Inc.; Natick, MA).

2.2.1. Simulations

To predict the effect from fitting a two-pool (water + MT) qMT model to a tissue that contains three effective pools (water + MT + fat), data were numerically generated from a three-pool model based on the equations from Portnoy and Stanisz (39). A set of typical parameters for WM and fat (WM: $R_{1obs} = 0.9\ s^{-1}$, $T_{2f} = 30$ ms, $T_{2m} = 11$ µs, $k_{mf} = 10\ s^{-1}$, PSR = 0.15; Fat: $R_{1obs,fat} = 0.365\ s^{-1}$, $T_{2,fat} = 133$ ms) (137) were used to model the tissue, and the sampling scheme included two

saturation powers at nominal flip angles (α_{MT}) of 900˚ and 1200˚, with frequency offsets ($\Delta\omega$) of 1, 1.5, 2, 2.5, 8, 16, 32, and 100 kHz. The fat fractions were varied between 0.0 and 0.95, stepped by 0.05. Gaussian noise was added to the data to simulate an SNR of 100 at thermal equilibrium (to match experimental parameters), and the two-pool model described by Yarnykh and Yuan (82) & Yarnykh (37), which does not account for the effect of fat on the observed signal fraction, was used to fit the noisy signal data at each fat fraction over 10,000 noise realizations per fat fraction. The mean and standard deviation of the fitted qMT parameters were plotted as a function of fat fraction and used to predict the effect of an un-modeled fat component on the qMT analysis.

2.2.2. Experimental Data

Subjects

Eight healthy controls were recruited and imaged for this study (mean age 29.4 ± 5.4, 4 female). The local Institutional Review Board approved this study, and signed informed consent was obtained prior to the examination.

Data Acquisition

All data was acquired on a 3.0 tesla Philips Achieva scanner (Philips Healthcare, Best, The Netherlands). A 2-channel, multi-transmit body coil was used for excitation and an 8–channel head coil was used for signal reception. The MT acquisition consisted of a single-slice with the field-of-view (FOV) centered along the ethmoid bone (using high-resolution T_2 images (128)), perpendicular to both ONs, and spanned, at minimum, the width of the head in all subjects. Parallel imaging with sensitivity encoding (SENSE) and second-order shimming over both ONs was used to minimize image artifacts arising from susceptibility differences between bone, tissue, and air. All images had an FOV of 150 x 150 mm^2, a slice thickness of 3 mm, and included both the ON and the brain (see Figure 2.1a,b). MT-weighted images were acquired using a 2D MT-prepared, three-echo spoiled gradient echo sequence (SPGR) (36). Nominal in-plane resolution was 1 x 1 mm^2, (reconstructed to 0.3 x 0.3 mm^2) with 2 signal averages, and a SENSE factor of 2. MT weighting was achieved using a 20 ms, single-lobed sinc-Gauss pulse, and the parameters listed in Table 2.1. The water (W), in-phase, out-of-phase (OP), and fat images were reconstructed using the seven peak fat spectrum, multi-echo mDixon option in the Philips

scanner software (133,134). Optic nerve motion artifacts were minimized by employing fixation every other dynamic using the Psychophysics Toolbox MATLAB extensions (138-141), resulting in 32 dynamics with two full sets of (fixated and non-fixated) qMT data. This consisted of an "on" dynamic, where subjects were asked to fixate on a white cross against a black background, and an "off" dynamic, where there was a black screen. To help address eye fatigue, the subjects were encouraged to not focus during the "off" dynamics.

Table 2.1 Scan parameters and MT prepulse parameters for the MT, B_1, B_0, and T_1 scans.

Scan:	Scan Parameters:	MT Prepulse Parameters: $\Delta\omega$ (kHz)	MT Prepulse Parameters: Powers	Scan Time (m:ss)
MT	TR/TE_1/ΔTE/α: 78/5.8/3.1 ms/10˚	1, 2, 2.5, 4, 8, 16, 32, 100	900˚, 1200˚	6:32
B1	TR_1/TR_2/TE/α: 30/130/5.7 ms/60˚	—	—	0:21
B0	TR/TE_1/TE_2/α: 50/5.8/8.1 ms/25˚	—	—	0:34
T1	TR/TE: 20/5.7 ms α: 5, 15, 20, 25, 30˚	—	—	2:00
			Total Time:	**9:27**

To correct for B_1 and B_0 inhomogeneities present in the imaging volume, B_1 (using the dual-TR actual flip angle GRE method (142)) and B_0 (using dual-TE GRE) maps were acquired using fast 3D techniques over 3 slices, centered on the MT acquisition. T_1 mapping was performed using a multiple flip angle (MFA) acquisition over 3 slices, centered on the MT acquisition. Fixation was not employed for the B_1, and B_0 acquisitions because it was assumed that B_1 and B_0 inhomogeneities will be slowly varying over the volume, while the T_1 acquisition did not utilize fixation in order to save time on the acquisition due to eye fatigue. Detailed scan parameters and acquisition times are listed in Table 2.1.

2.2.3. Data Postprocessing

Brain Data

To determine the effects of the Dixon method on MT data, we first considered the W and OP data in the brain regions for all subjects. Using the Brain Extraction Tool (BET (143,144)) and

FLIRT (145,146) packages from FSL (147), the skull and ONs were removed, and the data was co-registered to the first MT offset for each image type, respectively. Large ROIs were drawn in the WM of the right hemisphere of the brain using the $\Delta\omega$ = 1000 kHz offset (see Figure 2.1a,b), and these were propagated to the MT-weighted, T_1, B_1, and B_0 images. OP data was used to approximate a normal out-of-phase acquisition, and to ensure user error during ROI selection did not contribute to differences in parameter values.

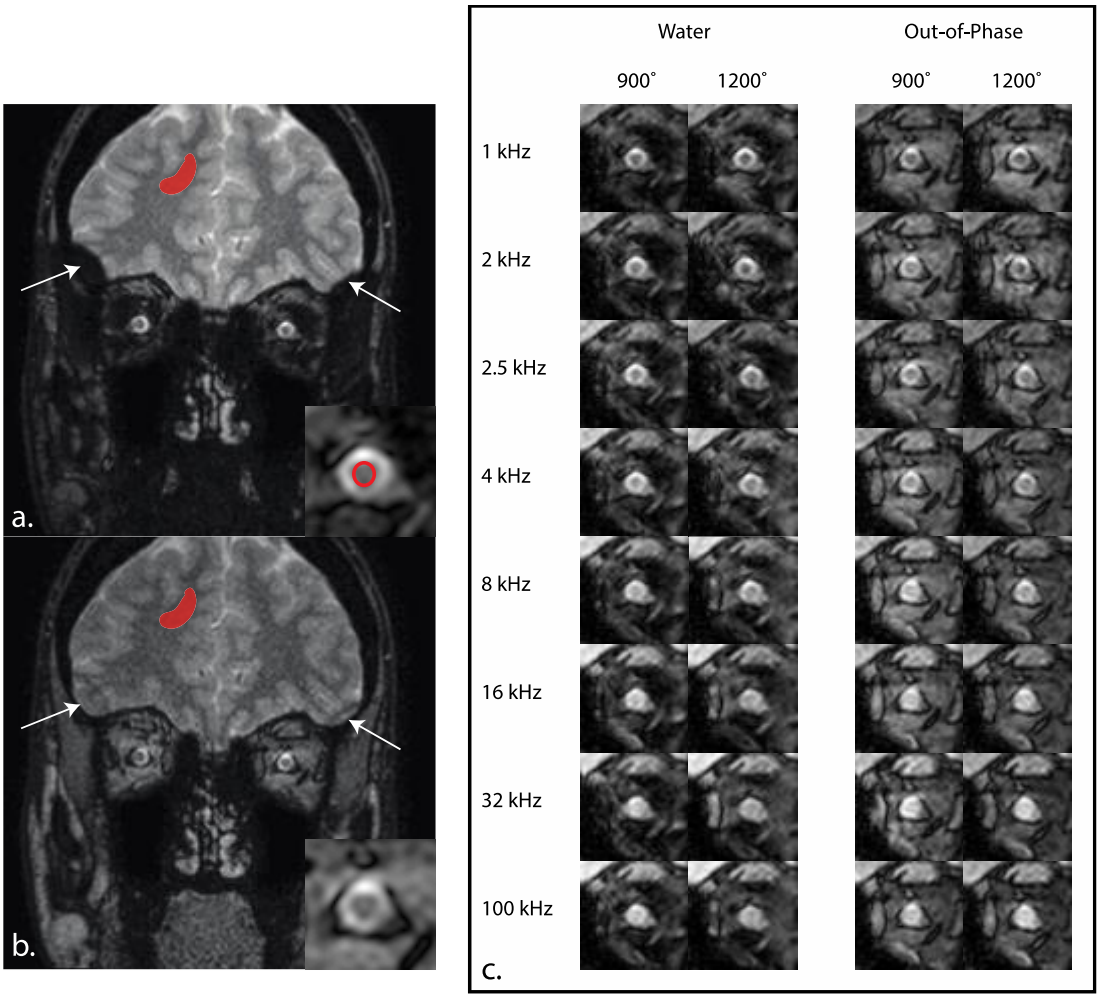

Figure 2.1. Panels (a.) and (b.) illustrate the MT effect at 1000 kHz with a saturation power of 900˚ for the (a.) water and (b.) out-of-phase images for a slice immediately posterior to the globe (proximal retrobulbar). The cutoff area of the brain on the outer edges of the volume in the water image is indicative of poor shimming in these regions, and thus, a mislabeling effect of the Dixon method (see arrows). The ROIs in (a.) and (b.) display the area used to compare the water and out-of-phase qMT parameters in the brain and optic nerve. The optic nerve ROI in (a.) is propagated to (b.) for analysis in the out-of-phase images. (c) Example MT-weighted data in the optic nerve for the water and out-of-phase images. Notice the increased conspicuity of the optic nerve against the surrounding tissue in the water images compared to the out-of-phase images.

Optic Nerve Data

ROIs were drawn in the W only images for each offset of the MT-weighted data of the ON (see Figure 2.1a) in each eye, as well as for the T_1, B_1, and B_0 data. As the W and OP images were taken from the same acquisition, the ROIs in the W images were also propagated to the OP

images. Following the ROI selection, W and OP qMT parameters were generated in both ONs for each volunteer using the methods described above.

Parameter Generation

The resulting data was used to generate qMT parameters for each volunteer using the qMT model described in Yarnykh (78) & Yarnykh and Yuan (82). This model contains six independent parameters: R_{1m}, R_{1f}, T_{2m}, T_{2f}, PSR = M_{0m}/M_{0f}, and $k_{mf} = k_{fm}/PSR$. The R_{1obs} ($1/T_{1obs}$) maps were independently reconstructed by regressing MFA data to the SPGR signal equation in the steady-state (148); these maps were used during MT parameter estimation (below) to estimate the parameter R_{1f} (78,82). Henkelman, et al. (34) & Morrison and Henkelman (19) showed that the signal dependence on R_{1m} is weak; therefore, it was set equal to the R_{1f} as well (37). The remaining MT parameters (PSR, k_{mf}, T_{2f}, and T_{2m}) were estimated for the W and OP brain data by fitting the qMT data to the two-pool model (78,82). For all fitting, the nominal offset frequency and RF amplitudes were corrected using B_0 and B_1 maps, respectively (74).

Statistical Analysis

The mean and standard deviation for each image type (W and OP) were calculated for each qMT-derived index in the brain and ONs. Statistical variations between the left and right ON (for both W and OP image types) and between the W and OP brain data were evaluated using the non-parametric Wilcoxon signed rank test, with a threshold for significance of $p < 0.05$, for each qMT parameter (PSR, k_{mf}, T_{2f}, and T_{2m}).

MAD Analysis: While the statistical analysis above is straightforward in the brain, due to the relatively homogeneous ROIs taken in each image type, the Wilcoxon signed rank test in the ON is more complicated (see Results), because this approach does not capture the potential for nested variance structures or an asymmetric number of voxels between eyes, and thus may potentially underestimate the true variance between each image type. Therefore, we also computed the mean absolute difference (MAD) of all possible left and right ON voxel pairs drawn from an empirically determined distribution (below). If there are *n* voxels in the right and *m* voxels in the left ON for a single subject, then the MAD is given by

$$MAD = \left(\frac{1}{mn}\right)\sum_{k=1}^{m}\sum_{l=1}^{n}|h_k(Left) - h_l(Right)| \qquad 2.1$$

where $h_k(Left)$ denotes a measure (e.g., PSR) on the k^{th} voxel in the left ON, and similarly, $h_l(Right)$ denotes the same measure (e.g., PSR) on the l^{th} voxel of the right ON. The distribution of data for each qMT parameter was empirically constructed via the bootstrap method with 3000 iterations (149). For each iteration, the subject-level MT data were resampled with replacement to generate a Z-spectrum, and qMT parameter maps were determined from this sampled MT data. The ROI-derived values for the T_1, B_1, and B_0 data from each subject was used in each case to avoid biases due to the variance that could occur from these parameters. The data for each subject was then combined, and a total MAD score was calculated. The empirical 95% confidence interval of the MAD for each parameter of interest was computed and examined for statistical significance.

We assumed no differences would exist in healthy subjects for each qMT parameter between the left and right ON, and that a low MAD indicates a greater symmetry between the right and left ON for a given qMT parameter and image type. Comparing across image types, we calculated the ΔMAD% as the difference in MAD values for each technique relative to the MAD for the OP acquisition as summarized in the following equation:

$$\Delta MAD\% = \frac{MAD(W) - MAD(OP)}{MAD(OP)} \times 100 \qquad 2.2$$

A negative ΔMAD% indicates a lower W MAD score compared with the OP MAD, and the ΔMAD% is an estimate of the relative improvement (or worsening) when using the Dixon method relative to using an OP image.

2.3. Results

2.3.1. Simulations

Figure 2.2 illustrates the effect of fat on the qMT parameters where the qMT-derived indices (from simulation) are shown against the fat fraction. Note the dotted black line is the true, expected value and the blue line shows the fit results for each parameter, with the error bars representing one standard deviation over 10,000 noise iterations at each point. The PSR never significantly diverges from the true PSR value (larger than one standard deviation from the true value); however, the k_{mf} and T_{2f} parameters significantly diverge from the true value for fat fractions greater than 0.3 and 0.1, respectively. Furthermore, the variance in the PSR and T_{2m}

increase as a function of fat fraction, which can generally be assumed as instability in the fitting algorithm at higher fat fractions.

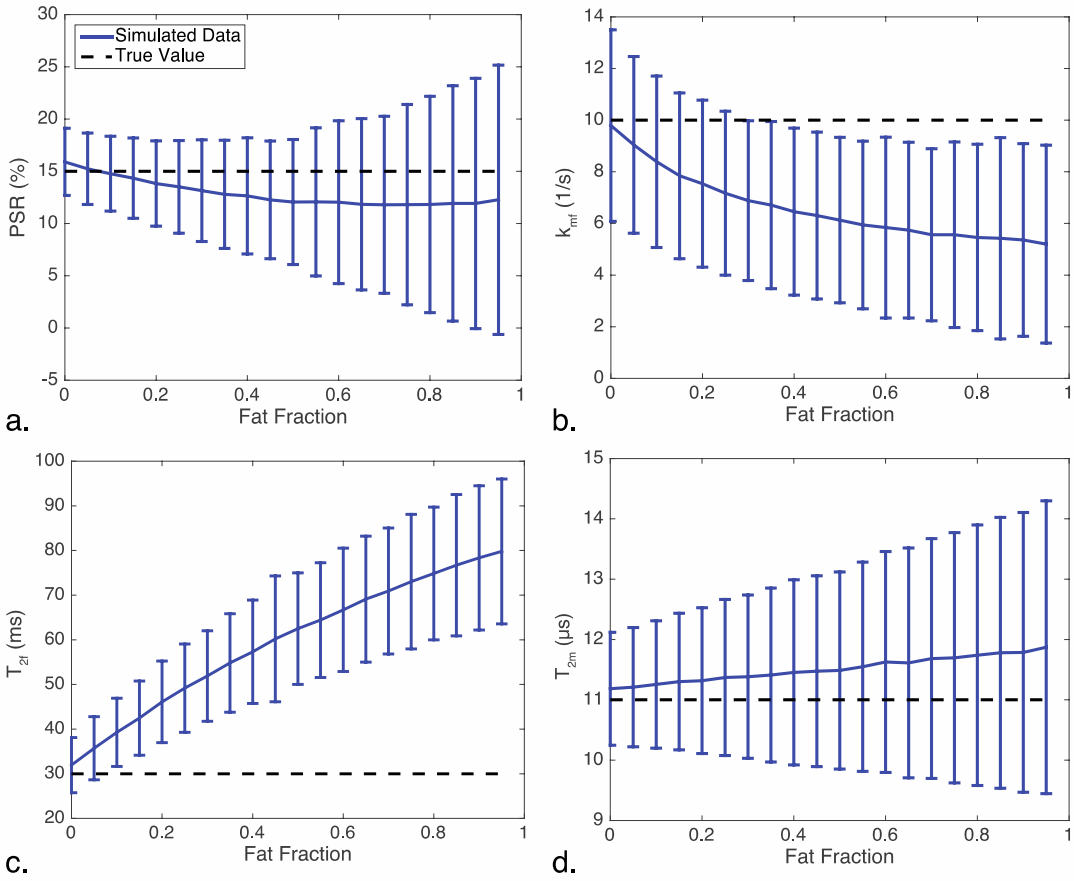

Figure 2.2. Results of the numerical simulations of the qMT parameters as a function of fat fraction, focusing on (a.) PSR, (b.) k_{mf}, (c.) T_{2f}, and (d.) T_{2m}. Notice that (a.), (b.), and (d.) all show increased variance with increasing fat fraction, while (b.) and (c.) show significantly different deviations from the true value at relatively low fat fractions (20% and 30% fat, respectively).

2.3.2. Experimental Data

Representative MT data for the W and OP image types are displayed in Figure 2.1. The conspicuity between the ON and surrounding tissue increases dramatically in the W images compared to the OP images (Figure 2.1c). Furthermore, fixation provides a marked increase in ON visualization, as can be seen in Figure 2.3a.

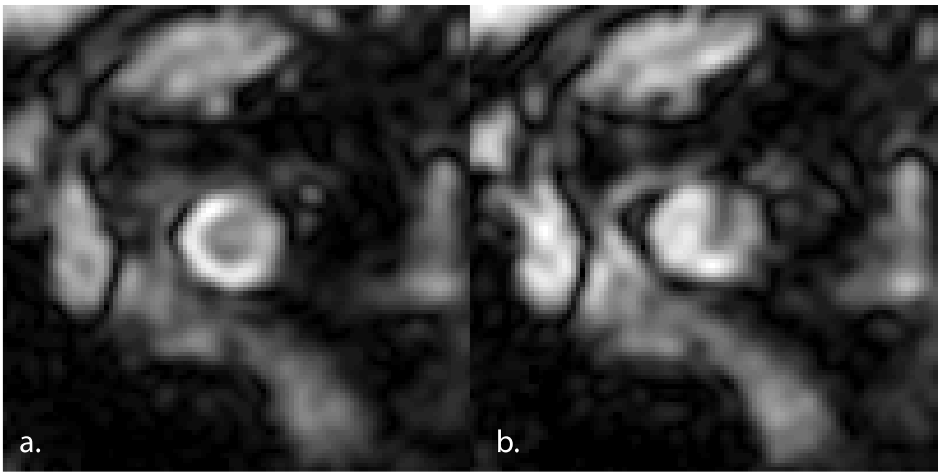

Figure 2.3. Example MT data with (a.) and without (b.) fixation. The nerve is much more clearly delineated when using fixation. An example ROI is also presented in (a.) to illustrate the area used to quantify the MT data.

Brain Data

The results comparing the qMT-derived indices between the W and OP image types in the brain are shown in Table 2.2. The mean values across methods are indistinguishable indicating no effect from combining multiple echoes for all qMT-derived indices. Further, all parameter p-values are well above the threshold for significance (p-values: PSR = 0.64, k_{mf} = 0.95, T_{2f} = 0.38, T_{2m} = 0.25), indicating there is no statistical significance between the W and OP images when no fat is expected to be present. Therefore, the Dixon method does not alter the MT-weighted observations and resulting fits during the multi-echo reconstruction.

Table 2.2 Mean and Standard Deviation of qMT Parameters in the Brain.

	PSR (%)	k_{mf} (1/s)	T_{2f} (10^{-2})	T_{2m} (μs)	R_{1obs} (1/s)
Water	17.0±1.7	17.2±5.2	1.8±0.2	11.1±0.8	1.15±0.17
Out-of-Phase	17.6±3.7	17.6±7.1	1.9±0.3	11.3±1.3	

Optic Nerve: W vs OP Data

qMT-derived indices for the ON are presented in Table 2.3, with an example of the fits displayed in Figure 2.4. Compared to the brain, the qMT-derived indices from the W ON data are different in the ON (lower for PSR, k_{mf}, and T_{2m}, higher for T_{2f}), which may be driven by differences in the

neurological tissue between the brain and ON (as is seen in the spinal cord (76)), or minor partial volume effects from cerebrospinal fluid (CSF).

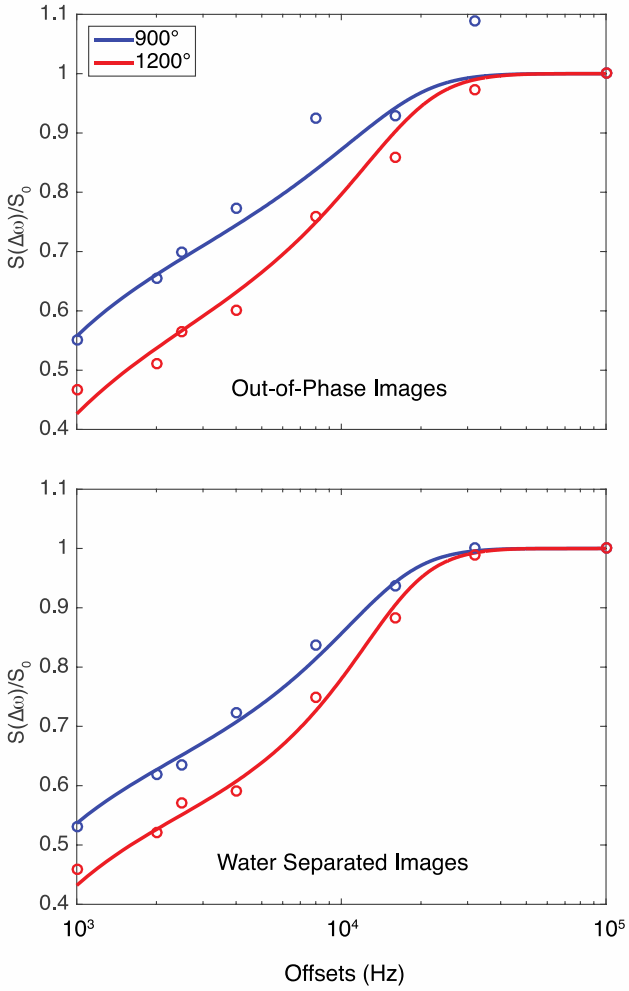

Figure 2.4. Example optic nerve Z-spectra for the out-of-phase and water images for a single subject. The water images (normalized residual = 0.0035) show better goodness of fit, and visually performed better compared to the out-of-phase images (normalized residual = 0.0228).

However, the k_{mf} in the OP data has a much higher mean and standard deviation than the W data (Table 2.3). Although the OP images have approximately $\sqrt{2}$ more noise than the W images, this does not fully account for the larger standard deviation seen in the OP images relative to the W images, as can be seen in Figure 2.5, which displays a box plot of the qMT parameters. This is important, as the PSR, T_{2f}, and T_{2m} seem to be relatively consistent across image types, indicating that the k_{mf} may be sensitive to the unmodeled fat components in the

tissue. When considering the MT-weighted data and the resulting fits (Figure 2.4 and Figure 2.5), the fits for the OP data were worse than those for the water separated data, indicating that some fat may be influencing the OP image data (see Figure 2.4 for representative residual values).

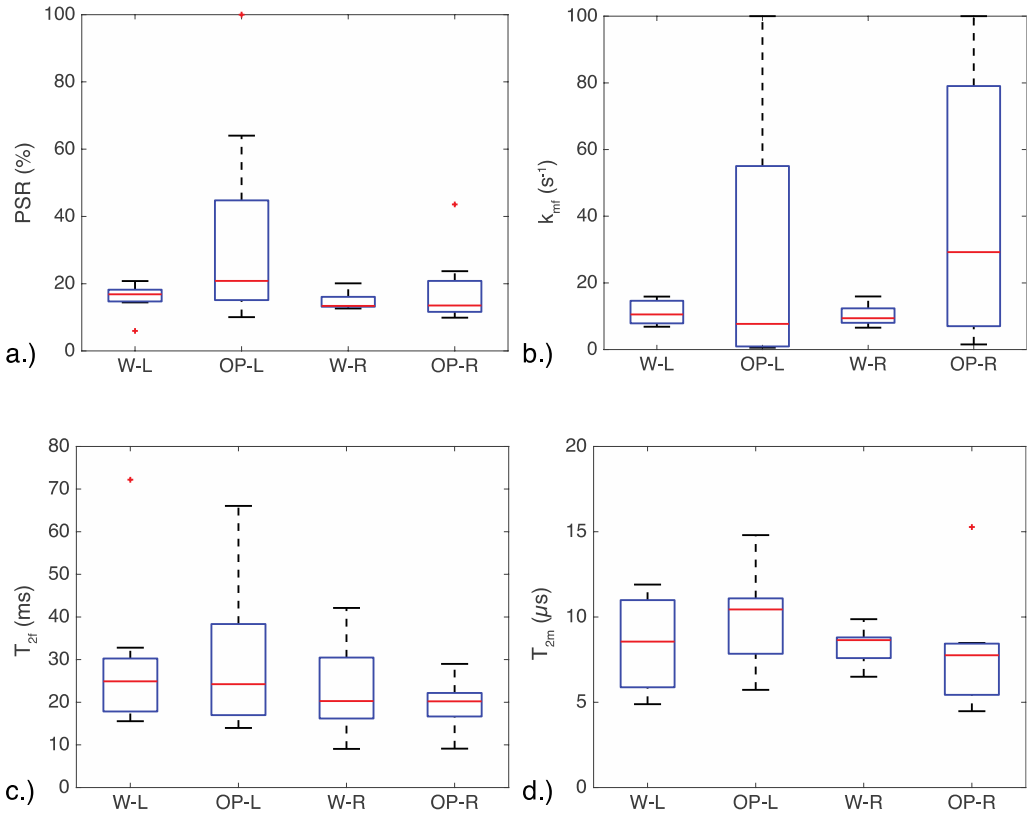

Figure 2.5. Box plots illustrating the variance in the a.) PSR, b.) k_{mf}, c.) T_{2f}, and d.) T_{2m} for the left (L) and right (R) optic nerves in both the water (W) and out-of-phase (OP) images. The k_{mf} shows a large amount of variation in the OP images, and small variation in the W images. A similar trend is seen in the PSR, indicating that the two-pool qMT model used here did not fit the OP data well.

Table 2.3 Mean and Standard Deviation of qMT Parameters for Left and Right Optic Nerves.

	PSR (%)		k_{mf} (1/s)		T_{2f} (10^{-2})		T_{2m} (μs)		R_{1obs} (1/s)	
	Left	Right	Left	Right	Left	Right	Left	Right	Left	Right
Water	15.8±4.4	14.7±2.7	11.1±3.6	10.2±3.2	2.9±1.8	2.3±1.0	8.5±2.7	8.3±1.1	0.94±0.19	0.82±0.12
Out-of-Phase	34.0±31.6	18.2±11.2	28.5±44.3	41.5±41.6	2.9±1.8	2.0±0.6	9.9±2.8	7.9±3.4		

Table 2.4 MAD Between Left and Right Optic Nerves at the Initial Point and 95% CI (MAD) and relative improvement (-) or Worsening (+) of Dixon Water Images Versus Out-of-Phase Images.

	PSR (%)			k_{mf} (s^{-1})			T_{2f} (ms)			T_{2m} (μs)		
	MAD	95% CI	ΔMAD%	MAD	95% CI	ΔMAD%	MAD	95% CI	ΔMAD%	MAD	95% CI	ΔMAD%
Water	7.69	[7.11, 7.83]	-4.46	9.16	[8.92, 9.57]	-6.76	6.50	[5.99, 7.08]	-5.63	1.24	[1.13, 1.27]	-11.32
Out-of-Phase	8.05	[7.40, 8.04]		9.83	[9.80, 10.19]		6.88	[6.24, 7.35]		1.40	[1.22, 1.40]	

Optic Nerve: Left vs. Right Data

Comparing the left and right ON data for each method, no significant differences can be seen for either method (p-values range from 0.11-0.95). This is expected, as the ONs in healthy subjects should not be significantly different from one another. We used this result to increase the power of the statistical test between image types (W versus OP) by combining the left and right ON data. Evaluating the mean qMT-derived indices in the W and OP data, there were no significant differences between any of the qMT parameters when employing the Wilcoxon signed rank test (p-values: PSR = 0.13, k_{mf} = 0.44, T_{2f} = 0.64, T_{2m} = 0.92). However, this is most likely due to the large variances found in the OP parameters (as seen in Figure 2.5), which ensures a high likelihood that each image type will be determined to be from the same distribution. The k_{mf} in particular displayed a large variance in the fitting derived from the OP images (L/R = 28.5±44.3/41.5±41.6 s^{-1}), implying that the OP images did not always yield high-quality fits to the data (see Table 2.3).

MAD Analysis

Table 2.4 provides the results of the MAD calculation (mean absolute difference between the left and right ONs drawn from an empirically determined distribution). We report the initial MAD value, the 95% CI for MAD from 3000 bootstrap iterations, and the ΔMAD%, which is the relative difference between the W and OP parameter values (note a negative value indicates improved MAD in the W images relative to the OP images). Recall that the MAD is a reflection of the variation across eyes rather than a variation of the mean qMT-derived index of interest. The variation across eyes for each qMT parameter are approximately the same between image types, and indeed, most of the 95% CI overlap one another (PSR, T_{2f}, T_{2m}). However, the k_{mf} 95% CI for each image type (W and OP) do not overlap, indicating that they may be drawn from separate distributions, and thus, these image types may show significantly different fits.

We next assessed the ΔMAD%, which is a reflection of the relative improvement (a negative ΔMAD%) or worsening (a positive ΔMAD%) of the variability across ONs (assumed to be small) when considering two different techniques. The ΔMAD% is negative for each qMT-derived index, indicating a general reduction in the variation across eyes derived from the W images

compared to the OP images. Therefore, the W imaging data from which we derive our qMT-indices outperform the same data considered from only OP images.

2.4. Discussion

The goal of this study was to demonstrate that qMT techniques will not be adversely affected by the use of the Dixon method. Furthermore, when considering regions, like the ON, where fat may influence the image, Dixon qMT imaging may derive higher fidelity fits and more accurate quantitatively derived indices. We compared the impact of fat on qMT-derived PSR, k_{mf}, T_{2f}, and T_{2m} via simulations (indicating the importance of accurate fat removal), and across healthy volunteers in the brain, where there is no fat, and in the ON, which is surrounded by a fatty sheath. Lastly, we evaluated the statistical impact of removing fat contamination from qMT data in difficult anatomies. We show that the OP images do not provide robust estimations of qMT-derived indices in the presence of fat, and that the Dixon method can be employed to reliably separate fat and water without altering the ability to characterize the MT effect using a two-pool qMT model. The ability to generate accurate qMT parameter maps while utilizing the Dixon method may increase the clinical applicability of qMT, as it provides a method to apply MT saturation in anatomies where fat may be in abundance, such as in the muscle (20), breast (150), or even the peripheral nervous system where fat is interlaced within the nerves (116).

2.4.1. Strength of Dixon Method

While on-resonant fat separation methods exist, they do not have the same advantages as the Dixon method. Binomial pulses may be used for fat suppression, however, clinically available gradient strengths/slew rates require implementation of large 3D volumes, which may not be suitable in anatomies prone to significant amounts of motion, such as the ON or abdomen, and may also significantly increase scan time. While echo planar imaging trains can be used to reduce scan time, employing these sequences in anatomies with large B_0 inhomogeneities, such as the ON and parts of the abdomen, may cause undesirable image distortion artifacts (151). The Dixon method, however, can be employed over any chosen (i.e. smaller) volume, reducing scan time, to accurately separate fat and water images. It should also be noted that the Dixon method is relatively robust to B_0 inhomogeneities, which can be problematic across different anatomies (132).

2.4.2. Statistical Implications

While the Wilcoxon signed rank test failed to statistically quantify the differences between the W and OP images in the ON, several conclusions can be drawn from the data itself. The k_{mf} parameter has a much higher variance in the OP images compared with the W images (Figure 2.5), suggesting that k_{mf} is sensitive to the underlying distribution. Therefore, if there are tissue components in a voxel that are not accounted for in the model, k_{mf} will be difficult to characterize, thus producing inaccuracies in the other qMT parameters. This is further confirmed utilizing the MAD data (Table 2.4). The ΔMAD% illustrates an improvement in the consistency of each qMT-derived index between eyes when the W only images are considered relative to the OP images. Furthermore, although there is a factor of $\sqrt{2}$ difference in SNR between the OP and W images, the MAD utilizes empirical data, which reduces the influence of nested variance and differences in noise between image types. Particularly important to this argument is the fact that our results from the brain indicate these differences are not due to variations driven by the different reconstruction methods (Dixon vs. non-Dixon) (see Table 2.2), suggesting the k_{mf} in tissues where voxels have a combination of tissue types is poorly characterized.

2.4.3. Simulations

Considering the simulations further (Figure 2.2), T_{2f} and k_{mf} deviate significantly as the fat fraction increases. Additionally, the PSR and T_{2m} show larger variance in their fit as the fat fraction increases, indicating greater instability in the fitting algorithm due to the presence of fat. This indicates that the errors from the k_{mf} and T_{2f} may be influencing the stability of the PSR and T_{2m}. This may also be the case in the OP ON images: although the PSR, T_{2f}, and T_{2m} are not significantly different from the W images, the k_{mf} is significantly different, indicating there may be errors present within the other OP qMT parameters as well. Therefore, ensuring all parameters in the qMT model are well determined is important to accurately model the MT effect, particularly in tissues where there may be significant partial volume effects present.

2.4.4. Data Reduction Strategies

While this study utilized a single slice acquisition to explore the Dixon method for fat suppression, an expanded 3D volume may be considered. However, scan time cannot be disregarded with any qMT method due to the number of powers and/or offsets that are required for appropriate

fitting. A single-point qMT model (1 MT-weighted volume with the addition of T_1, B_1, and B_0 maps) has been introduced to reduce the scan time to a clinically appropriate length, and has been applied to the brain (37), spinal cord (76) and muscle (152). However, the assumption for single-point qMT is that the parameters k_{mf}, T_{2f}, and T_{2m} are well-determined from prior scans utilizing a full qMT acquisition. Therefore, without adequate fat suppression, variance in the assumed model parameters may result in a poorly constrained model and will be hampered in tissues where fat cannot be excluded such as the ON, peripheral nerves, and muscle. Importantly, these experiments utilized out-of-phase images to perform the T_1 mapping. However, this may introduce fat signal into the T_1 data, confounding the results. While the observed T_1 does not seem to be adversely affected by the presence of fat here, this will potentially limit the scan if appropriate fat suppression techniques are not employed.

This study used a fixation cross to help minimize motion across dynamics, due to the large saturation and readout times for each MT dynamic (approximately 10 seconds), which resulted in large amounts of motion blur (Figure 2.3). To minimize tiring during fixation, we utilized a 1-on and 1-off acquisition scheme (one dynamic under fixation and the next dynamic without), which effectively doubles the scan time. Requiring fewer dynamics would significantly alleviate these challenges.

2.4.5. Limitations

While fat was the target of this study, the CSF surrounding the ON may also influence the signal from nerve tissue due to partial volume effects. CSF will reduce the MT effect within the nerve and thus partial volume effects will result in an underestimation of the PSR, k_{mf}, and T_{2m} and overestimation of T_{2f} (Table 2.2 and Table 2.2). Researchers have investigated the use of inversion recovery pulses in diffusion imaging for CSF suppression (153,154) however, this would add significantly to the scan time and may introduce extraneous off-resonance effects for nearby slices. Additionally, while techniques such as DANTE (155) may provide advantages over inversion recovery methods, they would still introduce extra off-resonance saturation effects, which would alter the observed MT effect and would need to be incorporated into the model.

Therefore, to preserve the fidelity of the observed MT effect in tissue, alternative techniques can be considered to accurately suppress CSF. A three-pool model (2 MT pools, and

1 non-exchanging pool) was recently introduced by Mossahebi, et al. (156) to fit the CSF pool (non-exchanging) in the brain. Their results suggest that the PSR can be accurately quantified even in the presence of significant amounts of CSF contamination. Research has also been performed to separate the CSF sheath from the ON using a model derived using T_2-weighted 3-D spin echo sequences with a turbo spin echo readout (128). These sequences have similar contrast to the small offset MT scans, and thus may be applicable to the MT-weighted data. Thus, further research is warranted to address the removal of the CSF sheath from the ON.

2.5. Conclusions

The results of this study demonstrate the ability to successfully remove the fat component from MT images using the Dixon fat-water separation method. The development of this technique provides a method to perform qMT while in the presence of significant B_0 inhomogeneities, and over small imaging volumes. Future work includes further investigation of this technique in the presence of disease, and application of this method in other anatomies with large fat components.

Chapter 3: Rapid, High-Resolution Quantitative Magnetization Transfer MRI of the Human Spinal Cord

Text for Chapter 3 adapted from:

Smith, AK, Dortch, RD, Dethrage, LM, and Smith, SA. (2014). "Rapid, high-resolution quantitative magnetization transfer MRI of the human spinal cord." NeuroImage 95: 106-116.

3.1. Introduction

The spinal cord (SC) is responsible for mediating neurological function between the brain and the peripheral nervous system and is somatotopically organized — sensory information is conveyed through the dorsal columns, while the lateral columns convey a significant fraction of motor function. The integrity of these organized columns is vital to preserving specific neurological function; therefore, even small SC lesions (e.g. multiple sclerosis (MS)) can result in severe neurological impairment. While the absolute mechanism of the pathophysiology of MS and nervous system tissue deterioration remains challenging to unravel, there is a body of evidence that suggests that axonal loss resulting in SC atrophy may relate to clinical impairment (157,158). Conventional MRI (i.e. spin-density, T_1- and T_2-weighted) can be used to measure atrophy or determine the location of inflammatory lesions in the spinal cord, but the relationship between conventional MRI indices (e.g. atrophy, lesion burden) and nervous system function and disease progression over time tends to be poor (159).

More quantitative MRI measurements, such as magnetization transfer (MT) and diffusion tensor imaging (DTI) metrics have been applied to the cervical spinal cord to investigate the relationship between neurological function and SC microstructure (38,115,117-123,160). Importantly, as these measurements report on microstructural changes that may precede atrophy, they potentially offer greater prediction of SC function than conventional methods. While quantitative MRI methods have shown promise for characterizing SC damage in diseases such as MS (161,162), widespread adoption has been challenged by the low signal to noise ratio (SNR), long acquisition times, and sensitivity to motion.

The focus of this work is on magnetization transfer (MT) imaging. Briefly, in addition to free water protons observed with conventional MRI, there are protons residing on immobile

macromolecules in tissue (33). Conventional MRI cannot image these protons directly because their T_2 relaxation times are too short (≈10 μs) to be captured by typical readout schemes. However, these macromolecular protons communicate with the surrounding water and, thus, can be indirectly imaged by exploiting this exchange, which is referred to as the MT effect. Importantly, MT imaging can serve as a surrogate marker for white matter myelin density in nervous system tissue (2,13,72) and, therefore, may be a more specific biomarker of disease evolution. Despite this promise, MT imaging has faced significant challenges in the spinal cord.

The contrast in an MT experiment is generated via application of a radiofrequency (RF) irradiation pulse at an offset frequency with respect to water ($\Delta\omega$) to selectively saturate the spectrally broad macromolecular protons. This saturation is then transferred to the free water pool via MT, resulting in an observed signal attenuation. The MT effect is often semi-quantitatively characterized via the MTR, which has been shown to correlate with myelin content (13). Unfortunately MTR is also sensitive to pulse sequence design, B_1 and B_0 inhomogeneity (6), as well as by tissue relaxation times and other non-MT-specific NMR parameters (34,73). This limits the ability of researchers and clinicians to create a standard MTR metric to define pathology. To overcome some of these limitations and to derive indices that are directly reflective of MT phenomena, quantitative MT (qMT) has been developed and implemented in the brain, but rarely in the spinal cord (36,38,73-75). qMT typically requires images to be acquired at multiple RF irradiation powers and/or offsets, generating a so-called MT z-spectrum for each voxel (124). The resulting z-spectrum can then be fit to a two (or more)-pool model to estimate quantitative indices, such as the macromolecular proton fraction (MPF), defined as the macromolecular pool size divided by the sum of the macromolecular and free pool sizes, or f, as reported by Yarnykh (37), the MT exchange rate from the macromolecular pool to the free pool (k_{mf}), and the transverse and longitudinal relaxation times for each pool (73). Often, the focus is on the MPF as it has been shown to correlate well with white matter myelin density (13,125-127), and may offer a biomarker of demyelination and axonal loss in white matter pathologies.

While qMT offers indices reflective of tissue physiology, translation of this methodology into the spinal cord within a clinically feasible scan time has proven to be a challenge. Even in the brain, collection of multi-power, multi-offset, high SNR, voxel-wise MT z-spectra can result in

scan times as long as 30-45 minutes for whole-brain coverage at low resolution (37). As the cord is small (only 1.5 cm in diameter at the cervical levels), with its component white and grey matter groups on the order of millimeters, even higher resolution is necessary, exacerbating the scan time problem. Additionally, at these high-resolutions, transverse SC motion resulting from cardiac and respiratory cycles, as well as cerebrospinal fluid pulsation, can lead to substantial artifacts. Lastly, the SC is surrounded by large bones that create spatially varying susceptibility gradients. Importantly for qMT, these susceptibility gradients can alter the effective B_1 and B_0 fields, leading to spatially dependent RF powers and offset frequencies. Fortunately, when performing qMT in the spinal cord, the model incorporates both B_1 and B_0 corrections, which can minimize the impact of spatially varying B_1 and B_0 errors in the estimated MPF value.

A new method to perform a qMT analysis using only a single MT-weighted acquisition and a reference measurement (no RF saturation) has been recently proposed for the brain (37). This method imposes constraints on the two-pool model in order to derive quantitative maps of the MPF in tissue from a single offset measurement (n.b., additional T_1, B_1, and B_0 measurements are also performed). Using this model, improved resolution or reduced sensitivity to motion can potentially be realized in clinically relevant scan times, making it a viable approach for the SC. Thus, the goal of this study was to determine the feasibility of translating this single-point approach to the cervical SC as a means of performing high resolution, rapid qMT imaging. Toward this end, we performed in vivo qMT in the cervical spinal cord of healthy controls and MS patients using (i) a low-resolution, multi-offset and power MT acquisition with a full model fit (the gold-standard); and (ii) high-resolution, single-point fits using the optimal offset and power from numerical simulations (c.f. *Methods)*. We evaluated the robustness of the single-point methods and sensitivity for disease in patients with MS. Additional numerical studies were performed to assess the effect of the constraints on the single-point qMT parameters. Lastly, the reproducibility of the acquisition and analysis methods was experimentally studied.

3.2. Materials and Methods

3.2.1. Data Acquisition

The local Institutional Review Board approved this study, and signed informed consent was obtained prior to the examination. Data were obtained from ten healthy volunteers (5 male, age range 23 – 28 years, mean age 25.6±1.7 years) and two female relapsing-remitting MS (RRMS) patients (31 and 25 years) on a 3.0 tesla Philips Achieva scanner (Philips Healthcare, Best, The Netherlands). A quadrature body coil was used for excitation and a 16-channel neurovascular coil was used for signal reception. A second acquisition was acquired on five of the volunteers after a minimum of two weeks to address reproducibility. The field-of-view (FOV) was centered between the C3 and C4 vertebral bodies, and spanned, at minimum, the C2 to C5 vertebral levels in all subjects. Parallel imaging with sensitivity encoding (SENSE) and second-order shimming was used to minimize image artifacts arising from susceptibility differences between bone and tissue.

Two MT protocols were performed: 1) a low spatial resolution acquisition (1 x 1mm^2) at 8 offsets ($\Delta\omega$) and 2 powers (α_{RF}) with a "full-fit" analysis (78,82) and 2) a high-resolution acquisition (0.65 x 0.65 mm^2) at 1 offset and power with a "single-point" analysis (37). For the full-fit qMT experiment, MT-weighted images were acquired using a 3D MT-prepared spoiled gradient echo sequence (36) with a GRE readout, TR/TE/α = 50 ms/2.3 ms/6˚, and SENSE acceleration factor = 2. Nominal resolution was 1 x 1 mm^2 in-plane (reconstructed to 0.6 x 0.6mm^2) over 12 slices (5 mm reconstructed slice thickness). Other parameters were: FOV = 150 x 150 mm^2, and 2 signal averages. MT weighting was achieved using a 20-ms, single-lobed sinc pulse with Gaussian apodization, α_{RF} = 360˚ and 820˚, and offset frequencies ($\Delta\omega$) = 1, 1.5, 2, 2.5, 8, 16, 32, 100 kHz (chosen to approximately logarithmically sample the expected MT z-spectra (37)). The total scan time for the low-resolution, full-fit acquisition was 12 minutes, 15 seconds. High-resolution, single-point MT-data were acquired using the same parameters, except: nominal in-plane resolution = 0.65 x 0.65 mm^2, and six signal averages. It should be noted that six signal averages for the single-point scan were chosen to approximate the SNR of the full-fit acquisition while also minimizing blurring due to intra-scan motion. MT weighting was achieved using the same pulse as the full-fit experiment but at $\Delta\omega$ = 2.5 and 100 kHz, and an α_{RF} of 820˚.

The single point RF irradiation offset was chosen based on numerical simulations to minimize bias in the MPF estimate (c.f. *Results*). The total scan time for the high-resolution, single-point acquisition was 7 minutes.

To correct for B_1 and B_0 inhomogeneities across the spinal cord, B_1 and B_0 maps were acquired using fast 3D techniques — B_0: dual-TE GRE with $TR/TE_1/TE_2$ = 50/4.6/6.9 ms and α = 60˚; B_1: dual-TR actual flip angle (AFI) GRE method (142) with $TR_1/TR_2/TE$ = 30/130/2.8 ms and α = 60˚. T_1 mapping was performed using a multiple flip angle (MFA) acquisition with TR/TE = 20/4.6 ms and α = 5, 10, 15, 20, 25, 30˚. A high-resolution multi-echo gradient echo (mFFE) scan was also performed and all echoes were averaged to generate a high contrast reference image for registration (163). The mFFE was obtained with TR/TE/ΔTE = 700/7.2/8.8 ms and α = 28˚. Nominal in-plane resolution was 0.65 x 0.65 mm^2. Acquisition times were 45 seconds for the B_0 map, 1 minute 12 seconds for the B_1 map, 1 minute 30 seconds for the T_1 map, and 5 minutes 30 seconds for the mFFE, resulting in a total acquisition time of ≈32 minutes.

3.2.2. Image Processing

All data analyses were performed in MATLAB R2013a (MathWorks, Natick, MA). Prior to data fitting, all images were cropped to an area immediately around the spinal cord and co-registered to the mFFE volume using the FLIRT package from FSL v5.0.2.1 (FMRIB, Oxford, UK) (145,146). The co-registration was limited to translation and rotation (±5˚) in-plane only (i.e. translation in x and y, and rotation about the z-axis). Following co-registration, qMT parameter maps were generated for each volunteer and patient using the full-fit qMT model described in Yarnykh (78) & Yarnykh and Yuan (82). This model contains six independent parameters: R_{1m}, R_{1f}, T_{2m}, T_{2f}, MPF = $M_{0m}/(M_{0f} + M_{0m})$, and $k_{mf} = k_{fm}*(1\text{-MPF})/\text{MPF}$. It has been shown that the signal dependence on R_{1m} is weak (19,34); therefore, it was set to 1 s^{-1} for fitting purposes. R_{1obs} ($1/T_{1obs}$) maps were reconstructed by regressing MFA data to the spoiled gradient echo signal equation in the steady-state (148). The resulting maps were then used to determine the parameter R_{1f}, as described by Yarnykh (78) & Yarnykh and Yuan (82). The remaining parameters were estimated for each voxel by fitting the full-fit qMT data to the two-pool MT model (78,82). For all fitting, the nominal offset frequency and RF amplitudes were corrected in each voxel using B_0 and B_1 maps, respectively.

It has been shown that T_{2m}, k_{mf}, and the product $T_{2f}R_{1f}$ can all be fixed during the fitting process because they all exhibit relatively constant values across tissues (82). Note that T_{2f} can be determined from the constrained $T_{2f}R_{1f}$ value and an R_{1f} estimate from the MFA data, while k_{fm} can be determined using the first-order mass action kinetics (127). Thus, these constraints result in a model where MPF is the only free parameter.

To estimate reasonable fixed parameter values for the single-point qMT analysis, histograms of $T_{2f}R_{1f}$, k_{mf}, and T_{2m} were created over the spinal cord for all slices and healthy volunteers from the full-fit analysis, and the median value of each histogram was chosen to enter into the single-point qMT analysis. Then, using the median values of the constraints and the optimal offset and power (determined from the numerical analysis below), the high-resolution, single-point data were analyzed to generate high-resolution MPF maps.

To numerically evaluate the error from only using a single offset to calculate MPF, Monte Carlo simulations were performed. For the simulations, we chose to study white matter, but also considered the case where the MPF and T_1 may be altered to model changes that may be experienced in pathologic conditions such as MS (so-called "lesion" in the *Results*). We do note, however, that modeling a lesion in this manner underestimates the complexity of the disease process, but nevertheless provides an estimate of the bias in the MPF that may be encountered in vivo in patient populations. All data were numerically generated from the equations provided in Portnoy and Stanisz (39). Gaussian noise was added to the data (SNR = 70 at thermal equilibrium to match experimental studies), and a single-point analysis was performed over 10,000 noise realizations for each of the following: (i) at each sampled offset and power to numerically evaluate the optimal sampling parameters for the single-point analysis, and (ii) over a range for fixed values for k_{mf}, $T_{2f}R_{1f}$, and T_{2m} to evaluate the potential bias generated by the incorrect assumptions about these values. For the first set of simulations, the relative root mean square (RMS) error (Relative RMS Error=$\frac{\sqrt{\overline{MPF_{act}-MPF_{est}}^{2}}}{MPF_{act}} * 100\%$, where MPF_{act} and MPF_{est} are the actual and estimated MPF values, respectively) was calculated in order to assess the combined effect of noise and bias for each combination of offset and power. For the second set of simulations, only the bias (Relative Bias = $\frac{|MPF_{act}-MPF_{est}|}{MPF_{act}} * 100\%$) resulting from the

constrained parameters was assessed.

3.2.3. Statistical Analysis

Mean MPF values for the single-point and the full-fit scans were calculated in the following regions of interest (ROI) for each slice: dorsal column, left lateral column, right lateral column, and grey matter, as shown in Figure 3.1b. ROIs were placed manually using MIPAV (NIH, Bethesda, MD) for each slice of each subject. In subjects with MS lesions, lesion ROIs were placed fully circumscribing lesions identified on the mFFE, while white matter and grey matter ROIs were placed in normal appearing regions in a similar fashion as the healthy volunteers. Statistical comparisons were performed on the mean MPF values from each ROI i) between the left and right lateral columns, ii) between the lateral and the dorsal columns, iii) between white matter and grey matter, iv) across slices and across subjects, and v) across time. Non-parametric Wilcoxon rank-sum tests were performed for the difference tests and the Kruskal-Wallis (non-parametric ANOVA) test was performed to evaluate differences across slices and volunteers. To avoid confounds of multiple-comparisons, we chose the significance threshold to be $p < 0.01$. Reproducibility and variability across time was assessed using Bland-Altman analysis (164). For each time point, each volunteer contributed a single MPF value for white matter (WM) and grey matter (GM), which were averaged over the entire cord. As part of this analysis, the normalized Bland-Altman difference (D_{BA}), 95% confidence interval for the difference, and the limits of agreement (1.96*SD of the difference across scans) were calculated.

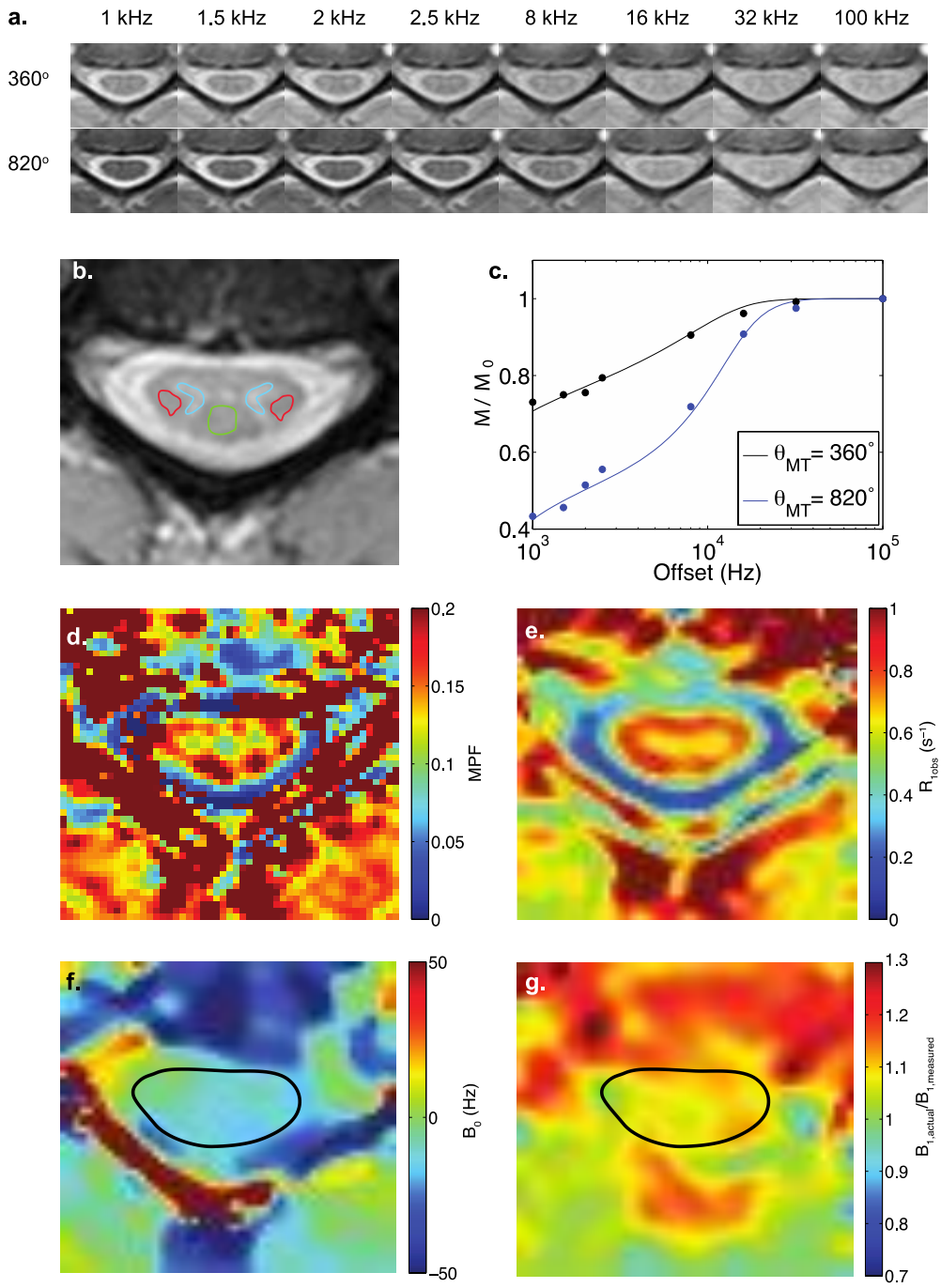

Figure 3.1. Full fit qMT data for a representative subject at C3/C4. (a.) Raw qMT data cropped to be centered around the spinal cord. (b.) The high-resolution anatomical image used to co-register the images, with ROIs drawn indicating the left and right lateral columns (red), the dorsal column (green) and the grey matter (blue). (c.) Z-spectra fit to experimental data taken from the dorsal column between C3 and C4. (d.) Representative full fit MPF map determined from the qMT data shown in (a.). (e.) Example $R_{1,obs}$ map of the spinal cord. (f. & g.) Example B_0 and B_1 maps of the SC, respectively.

3.3. Results

3.3.1. Data Acquisition

Representative MT-weighted images in a healthy volunteer at the level of C3/4 are shown in Figure 3.1a, and corresponding high-resolution mFFE data are given in Figure 3.1b. Note that the cropped images shown in Figure 3.1a and Figure 3.1d-g are derived from the registration process (c.f. *Methods*). Figure 3.1c shows mean ROI data (circles) placed in the lateral column white matter of a healthy volunteer at powers = 360° (black) and 820° (blue). The solid lines denote the full-fit qMT analysis, which agrees well with the experimental data ($\chi^2 = 0.005$, $p < 0.001$). Figure 3.1d shows the derived MPF map at the same level. Note that in the MPF (and $R_{1,obs}$) map, the grey matter is clearly delineated from the surrounding white matter as indicated by lower MPF (and $R_{1,obs}$) values in general. Note also the poor quality of the fitting near tissue interfaces (such as the spinal cord bordering the CSF), which may be related to a poor estimation of k_{mf} in these regions due to partial volume effects with CSF, and may be further exacerbated by the choice of motion correction strategies, spatial interpolation and within scan motion. For comparison, R_{1obs}, B_0, and B_1 maps are shown in Figure 3.1e, f, and g respectively. The average $T_{1,obs}$ values for the lateral columns, dorsal column, and grey matter were found to be 1.24±0.20, 1.24±0.23, and 1.33±0.19 seconds, respectively.

Figure 3.2 shows whole cord histograms for each single-point constrained parameter (k_{mf}, $T_{2f}R_{1f}$, T_{2m}) derived from the full-fit analysis approach over all healthy volunteers for white matter and grey matter. All histograms have a single peak for each tissue type, although k_{mf} and $T_{2f}R_{1f}$ are left-skewed with long tails at high values, and each histogram has similar peaks across tissue types. The median values of each parameter used for single-point fitting constraints were: $k_{mf} = 8.95\ s^{-1}$, $T_{2f}R_{1f} = 0.0232$, $T_{2m} = 10.8\ \mu s$.

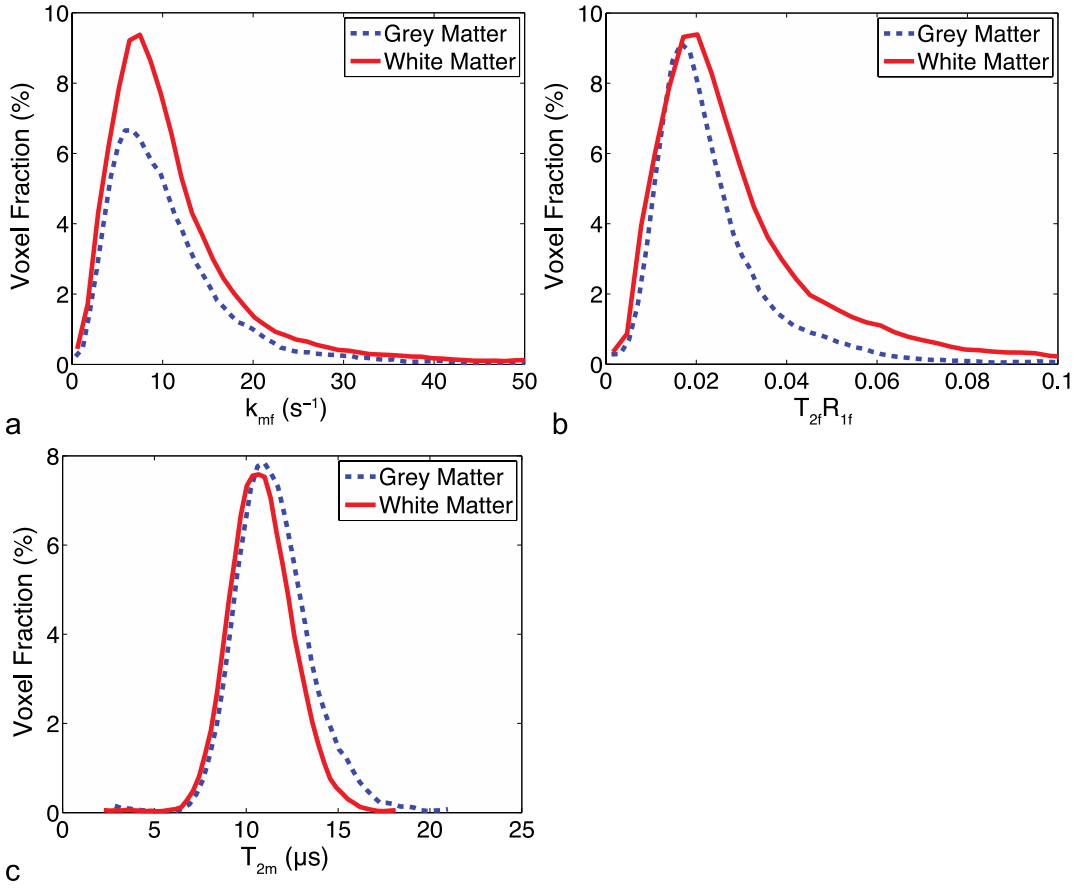

Figure 3.2. Histograms of the full fit model parameters for the control group subjects for (a) the exchange rate constant k_{mf}, (b) $T_{2f}R_{1f}$, and (c) T_{2m}, normalized to the total number of voxels and computed with the bin sizes 0.78 s^{-1}, 0.0031, and 0.37 μs for k_{mf}, $T_{2f}R_{1f}$, and T_{2m}, respectively.

3.3.2. Numerical Error Analysis

Figure 3.3 shows the numerical analysis of errors comparing full-fit qMT estimates of the MPF to the single-point methods. The MPF relative RMS error as a function of RF offset and power is shown in Figure 3.3a for simulated healthy white matter (dashed) and lesion data (solid). For healthy white matter, a minimum RMS error is seen for MT offsets between 1.5 and 3 kHz for both α_{RF} values. The lesion has a slightly greater RMS error over all offsets and powers, but tracks with the healthy (dashed) values at intermediate offset values. In fact, lesion and white matter RMS error were statistically indistinguishable at offsets = 1.5 to 3 kHz at α_{RF} = 820˚.

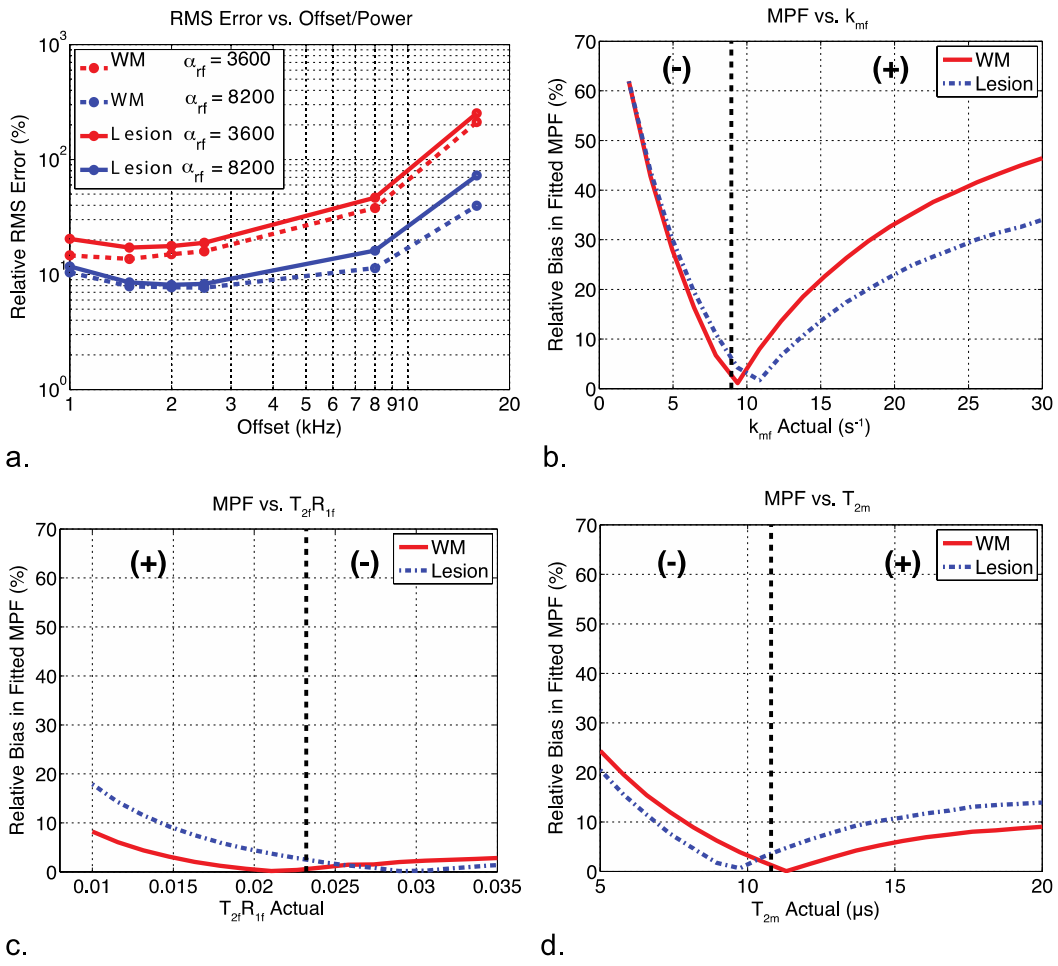

Figure 3.3. Analysis of the errors associated with the single-point analysis of MPF. (a) The RMS error associated with each offset and power for white matter and a lesion. (b, c, & d) The relative bias associated with inaccurate fixed values for k_{mf}, $T_{2f}R_{1f}$, and T_{2m}, respectively. The dotted line represents median value for each parameter over all healthy subjects, which was the fixed value for all analyses, and the (+) and (-) represent the sign of the bias on either side of the inflection point for each plot. When not varied, parameters were set to: $\Delta\omega$ = 2.5 kHz, RF power = 820˚, T_{2m} = 10.8 μs, $T_{2f}R_{1f}$ = 0.0232, and k_{mf} = 8.95 s^{-1}.

The bias in the estimated MPF value associated with incorrect parameter choices for k_{mf}, $T_{2f}R_{1f}$, and T_{2m} are shown in Figure 3.3b, c, and d, respectively. Note that $T_{2f}R_{1f}$ and T_{2m} stay below 20% for all constrained parameter values and tissue types indicating that incorrect assumptions for $T_{2f}R_{1f}$ and T_{2m} values do not introduce a significant source of bias in the MPF estimate. Incorrect assumptions about k_{mf} can result in a significant level of MPF bias in some cases, however, a 50% increase/decrease in k_{mf} will result in a 20% bias in the observed MPF, or an over-/underestimation of only 0.02 for an MPF of 0.1. While the k_{mf} chosen for this analysis is chosen

via histogram analysis derived from healthy control data, simulations predict that the slightly elevated k_{mf} in lesions biases estimates of the MPF by less than 10%. The estimates for the other median MT parameters values in the MS patients are similar to the healthy controls (k_{mf} = 8.54 s^{-1}, $T_{2f}R_{1f}$ = 0.0311, and T_{2m} = 10.3 μs); therefore, we do not expect assumptions regarding these parameters to be a significant source of bias in lesions.

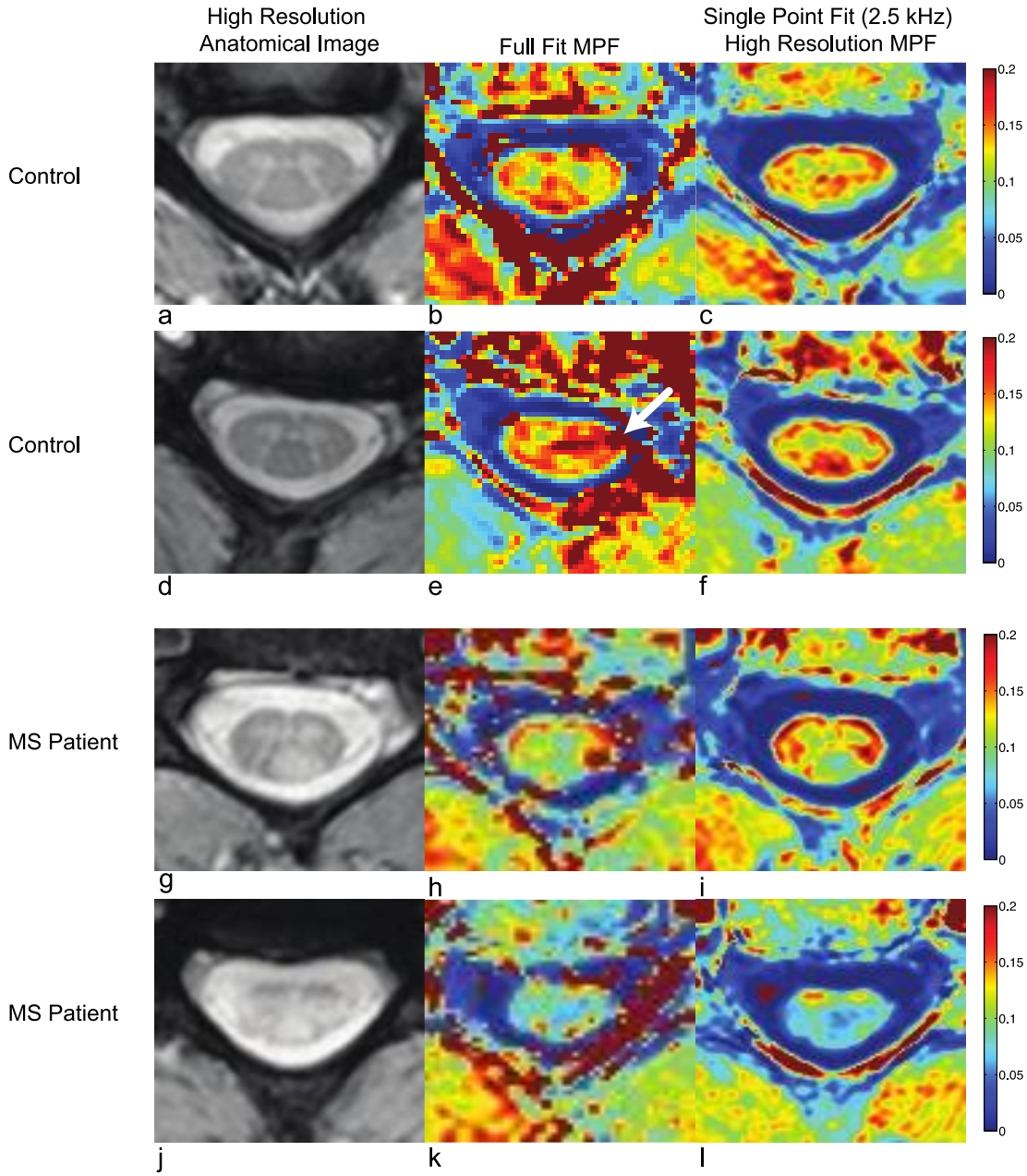

Figure 3.4. Comparison of full-fit and high-resolution single-point MPF maps for two controls (a-f) and high-resolution single-point MPF maps for two MS subjects (g-j).

3.3.3. Comparison to MS

Anatomical mFFE and MPF maps are displayed in Figure 3.4. Figure 3.4a-c and Figure 3.4d-f illustrate results in two different healthy volunteers at the level of C3/4 with full-fit and high-resolution single-point maps taken at $\Delta\omega$ = 2.5 kHz and α_{RF} = 820˚. Note that the contrast is such that dense white matter regions (lateral, dorsal, and ventral columns) have a higher MPF value

(red) compared to the grey matter (green), while the CSF exhibits little to no MT effect (blue). The single-point maps show contrast between white and grey matter more clearly than the full-fit MPF maps, and agreed with the size and location of the anatomical definition shown in the mFFE. Additionally, the single-point MPF shows more consistent values in the CSF and at the boundary between the spinal cord and CSF. Note the artifact in Figure 3.4e (arrow), which is not seen in the single-point method. Since the constraints are applied rather than calculated for each slice, aberrant data points (due to motion, or pulsation) may have a smaller impact on the overall quality of the fit. Additionally, the application of median values also reduces the artifacts that arise due to poor fitting at tissue interfaces. Lastly, at higher resolution, the detail of the grey matter butterfly can be appreciated in Figure 3.4f. Figure 3.4g shows an mFFE at the level of C3/4 in a patient with relapsing-remitting MS who presented with sensory deficits localized to lesions in the dorsal column (Figure 3.4g). The high-resolution, single-point MPF map (Figure 3.4i) shows a reduced MPF value (0.09±0.01) in the lesion compared to the lateral and ventral columns (red, 0.17±0.02) and compared to healthy control white matter (0.16±0.01). Importantly, the single-point MPF maps show similar MPF values to the full-fit maps even when pathology is present. While simulations (Figure 3.3) predict an underestimation of the MPF of approximately 5% due to the decrease in k_{mf} of approximately 0.5 s^{-1}, this does not solely explain the large decrease in MPF observed in the lesion. For example, if the normal white matter MPF = 0.16, this underestimation would change this MPF estimate to 0.15, which is still within one standard deviation of the normal white matter MPF. This is also the case when looking at the MPF maps for the second MS patient (Figure 3.4j-l). This patient presented with difficulty walking, sensory and motor impairment; examination of the mFFE reveals lesions in both lateral columns, and fasciculus gracilis of the dorsal column, but the ventral columns appear intact. The MPF (Figure 3.4k,l) corroborates the location of tissue damage and the high-resolution single-point MPF map more clearly delineates intact ventral columns (0.14±0.01) even though the majority of the cord shows a substantially lowered MPF (0.07±0.01) compared to healthy volunteers.

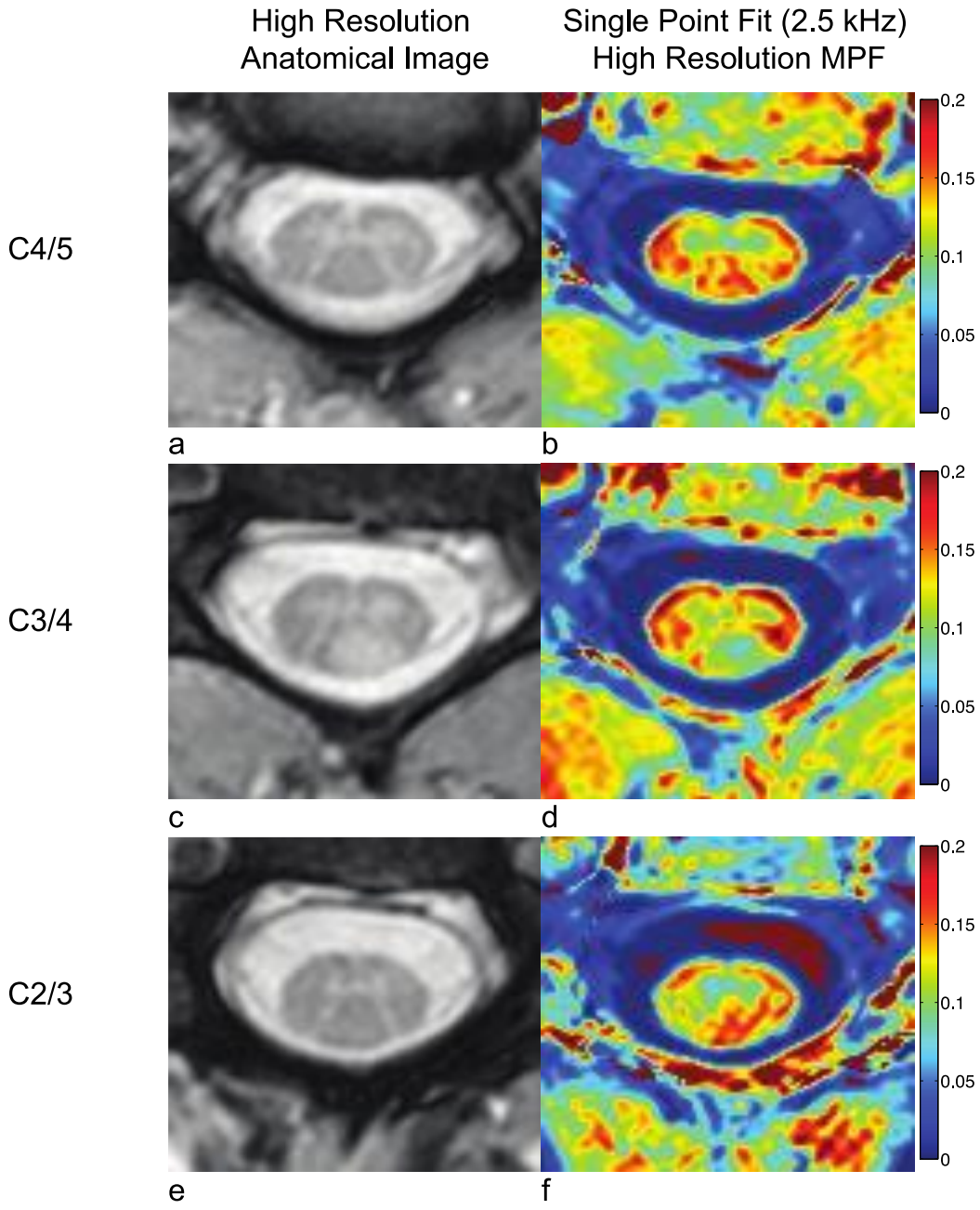

Figure 3.5. MPF maps caudal (a-b) and rostral (e-f) to the lesion (c-d) shown for the first MS patient (shown in Figure **3.4**g-i).

Figure 3.5 shows images of the MPF and the mFFE at spinal cord levels caudal to (Figure 3.5a, b), at the level of (Figure 3.5c, d), and rostral to the dorsal column lesion (Figure 3.5e, f) in the first MS patient. The MPF of the dorsal column lesion seen in Figure 3.5d appears to not be well visualized at more rostral and caudal levels. At the level of C2/3 (rostral to the dorsal column lesion), the right lateral column appears to be normal on the mFFE, and this is confirmed by the

MPF values (C2/3:0.16±0.01, C3/4:0.09±0.01, C4/5:0.15±0.01), which indicates the white matter MPF returns to normal values rostral and caudal to the lesion.

Table 3.1 Mean MPF and Wilcoxon rank-sum tests for the difference between the full-fit and the high-resolution single-point fit for the dorsal column (DC), lateral columns (LC), and grey matter (GM).

	Mean MPF		**Wilcoxon Rank-Sum**
	Full Fit	Single Point	p-value
DC	0.16±0.01	0.15±0.01	0.79
LC	0.16±0.02	0.16±0.01	0.57
GM	0.14±0.01	0.13±0.01	0.06

3.3.4. Statistical Analysis

Table 3.1 shows mean column wise MPF (±SD) values over healthy controls and the p-value for the Wilcoxon rank-sum comparison between the full-fit and single-point derived MPF. Importantly, there is no significant difference between the MPF estimates from each method for white matter ($p > 0.5$), but a trend is noted for grey matter ($p = 0.06$), which is likely due to the quality of the full-fit near tissue boundaries and especially in the small grey matter structures.

Table 3.2 shows the p-values for Wilcoxon Rank-Sum comparisons across columns (Left vs. Right Lateral Column, Dorsal Column vs. Lateral Column, and white matter vs. grey matter) and Kruskal-Wallis comparisons across volunteers. There were no statistical differences between left and right lateral columns ($p = 0.39$, $p = 0.57$) or between lateral and dorsal columns ($p = 0.43$, $p = 0.52$) for either the single-point method or the full-fit analysis, respectively. However, the MPF was significantly different between white and grey matter for both the full-fit ($p = 0.001$) and the single-point fit ($p < 0.001$). When comparing across volunteers and slices, there were no significant differences across slices and volunteers in both the full-fit and single-point fit for all tissue types, indicating the ability for both single- and full-fit analyses to robustly generate similar MPF values throughout the cervical spinal cord. It should be pointed out that the Kruskal-Wallis

test shows a trend towards significance when comparing across volunteers with the single-point method.

Table 3.2 P-values for the Wilcoxon rank-sum test and the Kruskal-Wallis test for full-fit and high-resolution single-point MPF maps. Tests were performed to evaluate the lateral column left vs right column differences (Left/Right), dorsal column vs lateral column differences (DC/LC), and white matter (lateral column and dorsal column) vs grey matter (WM/GM) differences.

Wilcoxon Rank-Sum			**Kruskal-Wallis**		
	Full Fit	Single Point		Full Fit	Single Point
Left/Right	0.57	0.39	WM	0.15	0.04
DC/LC	0.52	0.43	GM	0.75	0.05
WM/GM	0.001	<0.001			

Table 3.3 The 95% confidence intervals, and limits of agreement for the Bland-Altman test for the full-fit and high-resolution single-point fit in white matter and grey matter in 5 volunteers. The table also displays the p-values for the paired t-test.

	White Matter		**Grey Matter**	
	Full Fit	Single Point	Full Fit	Single Point
Mean Difference	-0.02±0.03	-0.008±0.016	-0.005±0.018	-0.001±0.008
95% Confidence Intervals	(-0.06,0.02)	(-0.03,0.01)	(-0.03,0.02)	(-0.01,0.008)
Limits of Agreement	(-0.08,0.05)	(-0.04,0.02)	(-0.04,0.03)	(-0.02,0.01)
p-value	0.29	0.34	0.56	0.76
D_{BA} (%)	10.26	5.33	3.84	0.90

Table 3.3 shows the Bland-Altman analysis of reproducibility of the MPF values for white and grey matter. The confidence intervals for white and grey matter overlap zero for both the full-fit and the single-point MPF and, thus, are not significantly different from time point one to time point two. Interestingly, in white and grey matter, the single-point, high-resolution images have approximately 2-fold smaller limits of agreement and 95% confidence intervals, and also

display lower D_{BA} values, indicating that the MPF derived from single-point methods are less variable across time compared to the lower resolution scans.

3.4. Discussion

The goal of this study was to demonstrate the feasibility of high-resolution MPF mapping of the human spinal cord in vivo. We compared the MPF across volunteers, between left and right lateral columns, between lateral and dorsal columns, between white and grey matter, and evaluated the slice-wise variability as well as the test-retest reliability for white and grey matter in the cervical SC. We show that the MPF can be consistently obtained in healthy volunteers, and that the MPF is significantly decreased in the lesions of patients with MS. The ability to generate MPF maps from only a single qMT measurement may increase the clinical applicability of SC qMT imaging because of the opportunity to obtain either high-resolution quantitative mapping, or rapid estimation (46 seconds/offset at 1x1x5 mm^3) of the MPF at lower resolution.

Currently, qMT of the spinal cord at 3.0-T has been limited (15), although several semi-quantitative measurements using the MTR (6) and MTCSF (14) have been reported (11,24,115,165,166). One challenge facing the MTR and MTCSF is that they are sequence and scanner dependent (6,34,73) and, therefore, cannot readily be used to quantitatively study tissue changes in the spinal cord across sites. In contrast, qMT-derived MPF values have been shown to be scanner independent and correlated with myelin content (13,125-127), but typically suffer from long acquisition times. Utilizing a single-point qMT measurement (with appropriate constraints) estimates of the MPF can be obtained in less time and at higher resolution. As can be seen from Figure 3.4, the higher resolution gained from only utilizing one off-resonance measurement provides benefits in characterizing the MPF at tissue interfaces in the spinal cord. The increased resolution also provides more accurate delineation of white and grey matter in healthy tissue, and additionally allows for straightforward lesion detection in demyelinating diseases such as MS. It should be pointed out that other novel methods have been presented to obviate the long acquisition times and derive MT indices that quantitatively reflective the magnitude of the MT effect (75). They differ from the method proposed in this manuscript by employing a fit to the signal equation for an MT-prepared FLASH sequence rather than imposing constraints on the two-pool model for MT.

It is important to note, that while MPF mapping of the human spinal cord in vivo has also been limited (15), MPF measurements of SC white matter in this study agree well with previously published MPF data in the brain (37) for the single-point methodology as well as the multi-point acquisitions (28). The lack of significant differences between the lateral and dorsal columns could be related to the fact that in the healthy cord, there are only subtle differences between the myelin density of the dorsal and lateral column. The qMT-derived MPF values for grey matter are also in good agreement with literature reports of grey matter in the brain.

Interestingly, when comparing the single-point and full-fit estimates of the MPF, a trend towards significance is seen from the former when evaluating the MPF across healthy volunteers. The complete analysis is shown in Table 3.2, which displays the results of the Kruskal-Wallis (non-parametric ANOVA) test. When examining controls across slices and across subjects, the full-fit displayed no significant variation across subjects ($p > 0.1$), whereas the single-point MPF trended towards significance at the $p = 0.01$ level ($p = 0.04$ and $p = 0.05$, respectively). This is intriguing because it offers the possibility that the single-point method may be sensitive to subtle differences between volunteers; or it may be that an improvement in the resolution minimized sensitivity to tissue interfaces.

The test-retest values of the model also did not demonstrate significant bias, indicating the model may be able to allow one to follow the MPF over time. Furthermore, as can be seen from the Bland-Altman analysis shown in Table 3.3, the single-point analysis displayed less variability over time than the full-fit analysis. This suggests that the temporal variability in the single-point method is less susceptible to day-to-day variations in the scanner as well as patient motion, potentially due to the constraints that are applied to generate the MPF index. We should point out, however, that differences in resolution, SNR, and CNR play a role in test-retest reliability, making it difficult to compare across protocols. Another confound is that for high-resolution scans, the within scan motion can be greater and is challenging to correct post-hoc, especially in the cord. Nevertheless, both the full-fit and single-point methods provide relatively robust test-retest reliability, which may have important implications for tracking pathology.

When choosing constraints for the one-point analysis, care must be taken when choosing the value for k_{mf}, as substantially erroneous estimates of k_{mf} can lead to large variations in the

MPF estimates (Figure 3.3). The median k_{mf} in the MS patients (k_{mf} = 8.54) was slightly different from that observed in the controls (k_{mf} = 8.95), which may have led to some of the observed differences in the MPF when lesions are present. According to Figure 3.3, this k_{mf} error would lead to an inflation of the estimated MPF of < 5% in patients. This is also seen experimentally in Figure 3.4h, j, k, and l, where, although there are minor differences between the full-fit and single-point MPF maps, the overall spatial correspondence of the lesion and magnitude of the estimated MPF are similar. When comparing the single-point MPF map of the patients to the anatomical images, the single-point, high-resolution MPF image more accurately depicts the pathology seen in the anatomical image, indicating that any small inaccuracies in the MPF do not change the impression of decreased MPF in lesions and are tolerable when considering trade-offs with respect to motion artifacts, etc. This is also the case when examining the areas around the lesion, where the MPF does not show appreciable partial volume effects.

Additionally, it is important to consider when the single point method may fail. The central theory behind the single point method is that the constraints chosen for k_{mf}, $T_{2f}R_{1f}$, and T_{2m} represent the majority of the tissue parameters present in a given tissue type. Therefore, from this theory, it is assumed that the variations (as seen in Figure 3.2) within these parameters are due primarily to parameters, such as noise, that are independent of the tissue. However, in pathology, these parameters may be seen to vary; Tozer, et al. (167) demonstrated that T_{2m} changes significantly in patients with glioma when compared with healthy controls. Therefore, it is important to ensure the constrained parameters do not change when applying the single point model in pathology.

The current clinical gold standard for visualizing white matter pathology is the MTR, however, it has been shown to be sensitive to B_1 and B_0 effects, pulse sequence design, hardware limitations, and scanner field strength (6,34,73). Nevertheless, it is important to cast the findings of our single-point method in light of the conventional MTR. To compare the single-point qMT-derived MPF to the MTR, we calculated the MTR using the high-resolution single-point MT data (α_{RF} = 820°, $\Delta\omega$ = 2.5kHz) which is defined as: MTR = 1-S($\Delta\omega$)/S_0, where S($\Delta\omega$) and S_0 are the signals obtained with and without RF irradiation, respectively. Similar to the MPF, the MTR in healthy controls shows no differences between dorsal (0.45±0.02) and lateral (0.45±0.02)

columns (p=0.68), but significant differences between white (0.45±0.02) and grey (0.42±0.02) matter (p = 0.009) are noted and expected. However, the MTR across slices and volunteers shows significant differences (Kruskal-Wallis, $p < 0.001$). While it is difficult to assume that either the MPF or MTR should (or should not) be different across volunteers, it has been shown that over a small segment of the spinal cord, tissue relaxation and myelin density should not vary significantly. Thus, we hypothesize that a measure sensitive to these phenomena should also not be different. Since the MTR varies over slices for healthy volunteers whereas the MPF does not, we postulate that the B_1, B_0, and T_1 correction applied to generate the MPF minimizes the impact of slice-wise, periodic fluctuations that can directly impact the accuracy of the estimate of MT-derived indices.

When considering reproducibility, the MTR shows no significant differences over time for both white (p = 0.63) and grey (p = 0.21) matter. However, Bland-Altman analysis shows that the MTR has a larger LOA and 95% confidence interval span (MTR LOA white matter = (-0.06,0.07), gray matter = (-0.03,0.06); 95% CI white matter = (-0.03,0.05), gray matter = (-0.01,0.05)), which underscores the importance of correcting both B_1 and B_0 in the MPF calculation.

In the two patients studied, we found that the MPF and MTR show different sensitivities. For the first patient (Figure 3.4g-i), the MPF in the lesion shows approximately a 50% reduction in the MPF value (0.09±0.01) compared to the lateral and ventral columns (0.17±0.02), and compared to healthy control white matter (0.16±0.01). The MTR, however, shows a 7% reduction (0.41±0.02) in the lesion compared to the lateral and ventral columns (0.44±0.06). For the second patient (Figure 3.4j-l), the MPF in the ventral columns (0.14±0.01) is slightly reduced (by 9%) yet it is still similar to the healthy control average in the ventral columns; the majority of the cord, however, is substantially lower (0.07±0.01). The MTR for this patient in the same regions shows a larger reduction (0.31±0.02) over the bulk of the cord compared to the ventral columns (0.44±0.01), and compared to healthy volunteers but still a smaller relative change than the MPF. We hypothesize that the change in T_1 between lesion types may play a role in the observed sensitivity of the MTR to different lesions, which are removed in the single-point MPF calculation. In summary, the MPF in well-delineated (Figure 3.4g-i) and diffuse (Figure 3.4j-l) lesions show a greater relative signal reduction than the MTR, yet neither the MPF nor the MTR reveals rostral-

caudal reductions at vertebral levels above and below the lesion (MTR C2/3:0.44±0.02, C3/4:0.41±0.02, C4/5: 0.43±0.03).

It should be pointed out that for both the single-point and full-fit MPF calculations, motion correction is important in determining the fidelity of the derived indices. In this work, we chose to use a standard motion correction package, FLIRT (FSL, FMRIB, Oxford UK), and the resulting images were transformed using linear interpolation. While visually this resulted in excellent spatial agreement between the target and the MT-weighted scans, alternative methods for spatial interpolation could be considered. Indeed, the interpolation choice may have an impact on the magnitude of partial volume effects at the cord boundary. A future study could examine the impact of motion correction on the derived maps. Additionally, motion within the scan cannot be overlooked. For high-resolution scans, the spinal cord will move more rapidly than the time it takes to sample the full k-space for our 3D acquisition and may result in blurring at the interfaces. Ideally cardiac and/or respiratory triggering could be used, but the dynamic change in the TR with each trigger may influence the assumption of a steady state magnetization. The findings herein suggest that while this motion may result in blurring, the constraints of the single-point model minimize the impact of motion on the estimated MPF values, especially at tissue interfaces.

While the scan times were within the clinical domain, this study did not pursue fast imaging methods such as segmented EPI to further accelerate scan times. These methods could be utilized to further decrease scan times, although additional considerations (e.g., susceptibility effects) need to me made when employing EPI readouts. This study also did not optimize the excitation flip angle in the qMT sequence. While the small flip angle was chosen to reduce T_1 effects that may be present at larger flip angles, a larger flip angle would provide more signal and, therefore, may be necessary in order to provide balance between scan time and SNR.

3.5. Conclusions

The results of this study demonstrate the feasibility of performing qMT imaging in human spinal cord in vivo. The development of this technique allows for a higher resolution quantitative scan of the spinal cord in less time than is needed for a conventional full-fit qMT acquisition. In healthy subjects, intra-subject reliability (i.e. test-retest) and through cord similarities were

demonstrated for both full-fit and single-point acquisitions. This method was also performed on patients with multiple sclerosis with well-described spinal cord lesions, providing preliminary evidence that this method can be utilized to illustrate pathology in vivo. Future work includes further investigating the effects of pathology on the k_{mf}, and high field applications of this methodology.

Chapter 4: qMT Characteristics of Multiple Sclerosis in the Cervical Spinal Cord and Single Point qMT Application to the Lumbar Cord

4.1. Influence of Multiple Sclerosis on the Constraints of the Single Point model in the Cervical Spinal Cord

4.1.1. Introduction

The spinal cord (SC) is involved in many central nervous system (CNS) diseases, and in multiple sclerosis (MS), it is hypothesized that SC damage is responsible for the bulk of clinical deficits (108,168). The SC is less than one tenth the size of the brain, and thus a small, 3mm lesion in the brain would encompass approximately 20% of the SC; the neurological equivalent of a 40mm lesion in the brain. Importantly, a 3mm SC lesion in a white matter column can result in complete loss of function from that column due to the somatotopic organization of the SC. Radiologically, conventional T_1 and T_2 methods are sensitive to necrosis, inflammation, or atrophy (169), while axonal damage and neurological disease progression occurs largely independently of changes in T_2 (170). Several studies have shown that SC pathology may provide a more direct indicator of disease progression and clinical disability than the brain can provide alone (171,172).

Magnetization transfer (MT) imaging has emerged as a viable alternative to conventional structural MRI indices, and has been shown to be remarkably sensitive to changes in myelin associated with pathologies such as MS (2,13,72). In particular, several studies have shown that MT may be able to estimate the severity of meningeal inflammation, which has been associated with axonal loss in postmortem SC studies (173,174). Furthermore, MT imaging may show abnormalities near the pia mater of the outer cord early in the disease course, before the development of significant atrophy, suggesting that the outer cord may be involved in disease progression (175)

Thus, employing MT contrast in MS and other demyelinating pathologies may provide a more sensitive biomarker of disease evolution than conventional MRI. MT is the biophysical phenomenon whereby free water protons observed with standard MRI methods (T_1 and T_2-weighted imaging) are in exchange with protons associated with immobile macromolecules in tissue (33). While conventional MRI cannot detect the protons associated with macromolecules

due to their short (≈ 10 μs) T_2 relaxation time, they are in constant exchange with water through dipole-dipole and direct chemical exchange; this exchange has been called the MT effect. Contrast in an MT experiment is generated via application of a radiofrequency (RF) irradiation pulse at an offset frequency with respect to water ($\Delta\omega$) that selectively saturates the spectrally broad macromolecular proton resonance. This saturation is then transferred to the free water pool via the MT effect, resulting in an observed water signal attenuation. MT has traditionally been quantified through the use of the magnetization transfer ratio (MTR), and has been used in several studies to show that MT is correlated with myelin content (11-13). However, the MTR is dependent on the acquisition parameters, as well as B_1 and B_0 inhomogeneities (6) and other non-MT-specific NMR parameters (34,73).

Some of the limitations of the MTR have been rectified by modeling (often via a two-pool model) the signal changes resulting from MT contrast (35,36) and deriving quantitative indices, which is referred to as quantitative MT (qMT). qMT typically requires the acquisition of several images at multiple RF irradiation powers and/or offsets, from which a so-called MT Z-spectrum can be generated for each voxel (124). The resulting Z-spectrum can be fit to estimate several indices, including the macromolecular (m) to free (f) pool size ratio (PSR) (15,59), MT exchange rate from the macromolecular to pool to the free pool (k_{mf}), and the transverse and longitudinal relaxation rates for each pool (73). Interest in estimating the PSR in particular has been driven by several studies (13,125,127,176-178), which have shown a strong correlation between the PSR and white matter myelin density. Indeed, several studies of MS have already incorporated the improvements of qMT, and have shown associations between the PSR and myelin (25,28,179). However, these studies have been limited by long acquisition times due to the need to collect multiple MT-weighted images, and thus, are hindered for clinical application.

Recently, fast whole-brain mapping of the PSR between the macromolecular and free pools using only a single MT-weighted image (and a reference image) (37) has been developed, and was subsequently applied in the SC (76) and the thigh (152) in healthy volunteers. This fast qMT estimation procedure (so-called single-point qMT) is accomplished by imposing constraints on the two-pool model, providing an opportunity to utilize the scan time savings for improved resolution or reduction of the sensitivity of the model to motion. Single-point qMT has also been

applied in the brain in MS patients (180) utilizing constraints derived from healthy volunteers. I seek to further this work by addressing whether or not a healthy-cohort derived set of constraints will hold true in patient populations, specifically in the cervical spinal cord of patients with MS. Therefore, my goal is to test whether or not single-point qMT model constraints need to be adjusted for measured model inputs from a patient population, and the impact these assumptions have on the estimation of the PSR in patients with MS. Toward this end, I i.) acquired low-resolution MT data in vivo in the cervical SC of healthy controls and MS patients, ii.) imposed a full two-pool model fit in both cohorts, and iii.) derived constraints to apply in a single-point model of the data. These constraints were then compared across cohorts to determine which set of parameters were more appropriate to use in the patient cohort. Lastly, I iv.) estimated PSR indices in each cohort for each set of constraints.

4.1.2. Materials and Methods

Data Acquisition

The local Institutional Review Board approved this study, and signed informed consent was obtained prior to examination. Data were obtained from two cohorts: 1.) thirteen healthy volunteers (8 male, age range 24 – 33 years, mean age 25±2.5 years), and 2.) eight relapsing-remitting MS (RRMS) patients (4 male, age range 30 – 49 years, mean age 40.5±5.37 years, mean EDSS score = 0.5±1.17) and a primary progressive MS (PPMS) patient (male, 60 years old, EDSS score 5) on a 3.0 tesla Philips Achieva scanner (Philips Healthcare, Best, The Netherlands). A quadrature body coil was used for excitation and a 16-channel neurovascular coil was used for signal reception. The field-of-view (FOV) was centered between the C3 and C4 vertebral bodies, and spanned, at minimum, the C2 to C5 vertebral levels in all subjects. Parallel imaging with sensitivity encoding (SENSE) and second-order shimming was used to minimize image artifacts arising from susceptibility differences between bone and tissue.

The same MT protocol from Chapter 3 was used here: two MT protocols were performed: 1) a low spatial resolution acquisition (1 x 1mm^2) at 8 offsets ($\Delta\omega$) and 2 powers (α_{RF}) with a "full-fit" analysis (78,82) and 2) a high-resolution acquisition (0.65 x 0.65 mm^2) at 1 offset and power with a "single-point" analysis (37). For the full-fit qMT experiment, MT-weighted images were acquired using a 3D MT-prepared spoiled gradient echo sequence (36) with a GRE readout,

TR/TE/α = 50 ms/2.3 ms/6˚, and SENSE acceleration factor = 2. Nominal resolution was 1 x 1 mm^2 in-plane (reconstructed to 0.6 x 0.6mm^2) over 12 slices (5 mm reconstructed slice thickness). Other parameters were: FOV = 150 x 150 mm^2, and 2 signal averages. MT weighting was achieved using a 20-ms, single-lobed sinc pulse with Gaussian apodization, α_{RF} = 360˚ and 820˚, and offset frequencies ($\Delta\omega$) = 1, 1.5, 2, 2.5, 8, 16, 32, 100 kHz (chosen to approximately logarithmically sample the expected MT z-spectra (37)). The total scan time for the low-resolution, full-fit acquisition was 12 minutes, 15 seconds. High-resolution, single-point MT-data were acquired using the same parameters, except: nominal in-plane resolution = 0.65 x 0.65 mm^2, and six signal averages. MT weighting was achieved using the same pulse as the full-fit experiment but at $\Delta\omega$ = 2.5 and 100 kHz, and an α_{RF} of 820˚. The total scan time for the high-resolution, single-point acquisition was 7 minutes.

To correct for B_1 and B_0 inhomogeneities across the spinal cord, B_1 and B_0 maps were acquired using fast 3D techniques — B_0: dual-TE GRE with $TR/TE_1/TE_2$ = 50/4.6/6.9 ms and α = 60˚; B_1: dual-TR actual flip angle (AFI) GRE method (142) with $TR_1/TR_2/TE$ = 30/130/2.8 ms and α = 60˚. T_1 mapping was performed using a multiple flip angle (MFA) acquisition with TR/TE = 20/4.6 ms and α = 5, 10, 15, 20, 25, 30˚. A high-resolution multi-echo gradient echo (mFFE) scan was also performed and all echoes were averaged to generate a high grey/white matter contrast target image for registration (163). The mFFE was obtained with TR/TE/ΔTE = 700/7.2/8.8 ms and α = 28˚. Nominal in-plane resolution was 0.65 x 0.65 mm^2. Acquisition times were 45 seconds for the B_0 map, 1 minute 12 seconds for the B_1 map, 1 minute 30 seconds for the T_1 map, and 5 minutes 30 seconds for the mFFE, resulting in a total scan time of ≈32 minutes.

Image Processing

All data analyses were performed in MATLAB R2016a (MathWorks, Natick, MA). Prior to data fitting, all images were cropped to an area immediately around the SC and co-registered to the mFFE volume using the FLIRT package from FSL v5.0.2.1 (FMRIB, Oxford, UK) (145,146). The co-registration was limited to translation and rotation (±5˚) in-plane only (i.e. translation in x and y, and rotation about the z-axis). Following co-registration, qMT parameter maps were generated for each volunteer and patient using the full-fit qMT model described in Yarnykh (78) & Yarnykh and Yuan (82). This model contains six independent parameters: R_{1m}, R_{1f}, T_{2m}, T_{2f}, PSR = M_{0m}/M_{0f},

and $k_{mf} = k_{fm}/PSR$. The R_{1obs} ($1/T_{1obs}$) maps were independently reconstructed by fitting the MFA data to the SPGR signal equation in the steady-state (148); these maps were used during MT parameter estimation (below) to estimate the parameter R_{1f} (78,82). Henkelman, et al. (34) & Morrison and Henkelman (19) showed that the signal dependence on R_{1m} is weak; therefore, it was set equal to the R_{1f} (37). The remaining parameters were estimated for each voxel by fitting the full-fit qMT data to the two-pool MT model (78,82). For all fitting, the nominal offset frequency and RF amplitudes were corrected in each voxel using B_0 and B_1 maps, respectively.

The single-point method has demonstrated that k_{mf}, T_{2m}, and the product $T_{2f}R_{1f}$ can all be fixed during the fitting process because they all exhibit relatively constant values across tissues (37,76). To estimate reasonable fixed parameters values for the single-point qMT analysis, histograms of k_{mf}, T_{2m}, and $T_{2f}R_{1f}$ were created (see section Comparison of Control Data and Patient Data below), and the median value of each parameter was chosen to enter into the single-point qMT analysis; the high-resolution MT-weighted images were then analyzed to estimate high-resolution PSR maps.

Comparison of Control Data and Patient Data

To determine whether the healthy control-derived constraints (assumptions) were similar to those from the MS patient cohort, mean parameter values for $S_{qMT} = [T_{2f}R_{1f}, k_{mf}, T_{2m}]$ were calculated over each slice for each subject, and the non-parametric Kruskal-Wallis (non-parametric ANOVA) test was performed to evaluate if differences exist between cohorts for all S_{qMT} parameters. Next, to estimate reasonable fixed parameter values to enter for the single-point qMT analysis, histograms of S_{qMT} that were derived from the full-fit analysis were created over the SC for all slices and for each cohort of subjects. Lastly, the median value of each parameter from S_{qMT} in each cohort was determined. The calculated constraints (assumptions) from the control cohort were applied to the high-resolution qMT data to derive the PSR maps. The results of the Kruskal-Wallis test above (see section 4.1.3) were used to determine the constrained S_{qMT} parameters to estimate the high-resolution PSR maps for the patient cohort.

Tissue Segmentation

The WM and GM in the control cohort were segmented from the mFFE images using the multi-atlas segmentation tool (181,182) previously developed for mFFE acquisitions. Each GM/WM

ROI was eroded using the imerode tool from MATLAB to ensure only WM and GM were selected, and the mean PSR values from the single-point data were calculated from each volunteer.

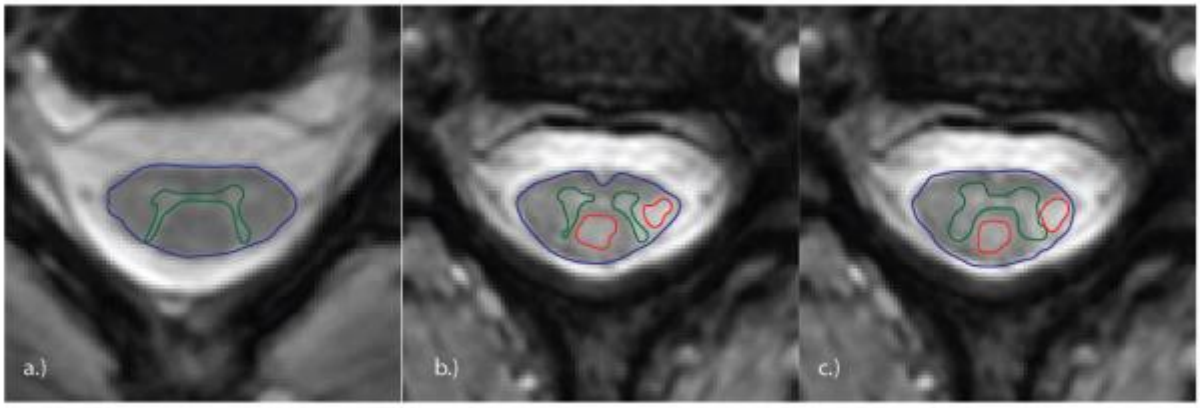

Figure 4.1. High-resolution anatomical images in a healthy control (a.), and an MS patient for rater #1 (b.) and rater #2 (c.) with ROIs drawn for WM (blue), GM (green), and lesions (red). The WM ROIs encompassed all SC data that was not labeled GM, central canal (see (b.), or lesion.

Since the multi-atlas procedure does not account for lesions, in the patient cohort, ROIs were drawn manually by two independent raters for each slice in the GM, NAWM, and lesions on the high-resolution mFFE image (shown in Figure 4.1b and c). ROIs were placed manually using MIPAV (NIH, Bethesda, MD) for each slice of each subject. Lesion ROIs were defined by areas of increased signal intensity relative to the surrounding white matter. The ROIs were then eroded as for the multi-atlas method to ensure only the WM, GM, and Lesion were identified and that partial volume effects were minimized. The mean single-point PSR was calculated for each subject and tissue type (white matter (normal appearing), grey matter, and lesion).

Statistical Analysis

Statistical comparisons were performed on the mean PSR values i) between raters for the patient cohort, ii.) between each tissue type in the patient cohort (NAWM, GM, and lesions), and iii) between the healthy control cohort (WM and GM) and the patient cohort for each tissue type. We chose the significance threshold to be $p < 0.05$ for all statistical comparisons. The Wilcoxon rank-sum test was used for comparisons ii) and iii), while the Bland-Altman analysis (164) was used for the inter-rater comparisons.

4.1.3. Results

Comparison of Control and Patient Parameter Data

The histograms derived from the low-resolution, full fit qMT analysis for k_{mf}, $T_{2f}R_{1f}$, and T_{2m} over the whole cord are shown in Figure 4.2 for both the control and patient groups. Although not significant, the k_{mf} was found to be lower in the patients (7.54 s^{-1}) relative to the controls (8.45 s^{-1}, p-value: 0.059). All histograms are single-peaked and are skewed in a similar manner between cohorts – the k_{mf} and $T_{2f}R_{1f}$ are skewed to the left with long tails at high values, while the T_{2m} presents little to no skew. The median values for the control and patient cohorts are: [8.45, 7.54] s^{-1}, [0.0239, 0.0279], and [10.66, 10.3] µs for the k_{mf}, $T_{2f}R_{1f}$, and T_{2m}, respectively, and are also shown in Table 4.1.

There were no significant differences found between the control and patient cohorts for any of the calculated constraints, however, k_{mf} is approaching a significant difference ($p = 0.059$). This suggests that, while not significant, there may be some differences in the assumed values between cohorts that need to be accounted to accurately model the single-point qMT data. Therefore, going forward, all patient data utilized the patient-derived full-fit constraints to calculate the high-resolution, single-point PSR data.

Table 4.1 Median estimated parameter values for the k_{mf}, $T_{2f}R_{1f}$, and T_{2m} in the control and patient cohorts, and the p-value from the Kruskal-Wallis test comparing each parameter in each cohort over all slices.

	Control	**Patient**	**p-value**
k_{mf} (s^{-1})	8.45	7.54	0.059
$T_{2f}R_{1f}$	0.0239	0.0279	0.102
T_{2m} (µs)	10.66	10.3	0.656

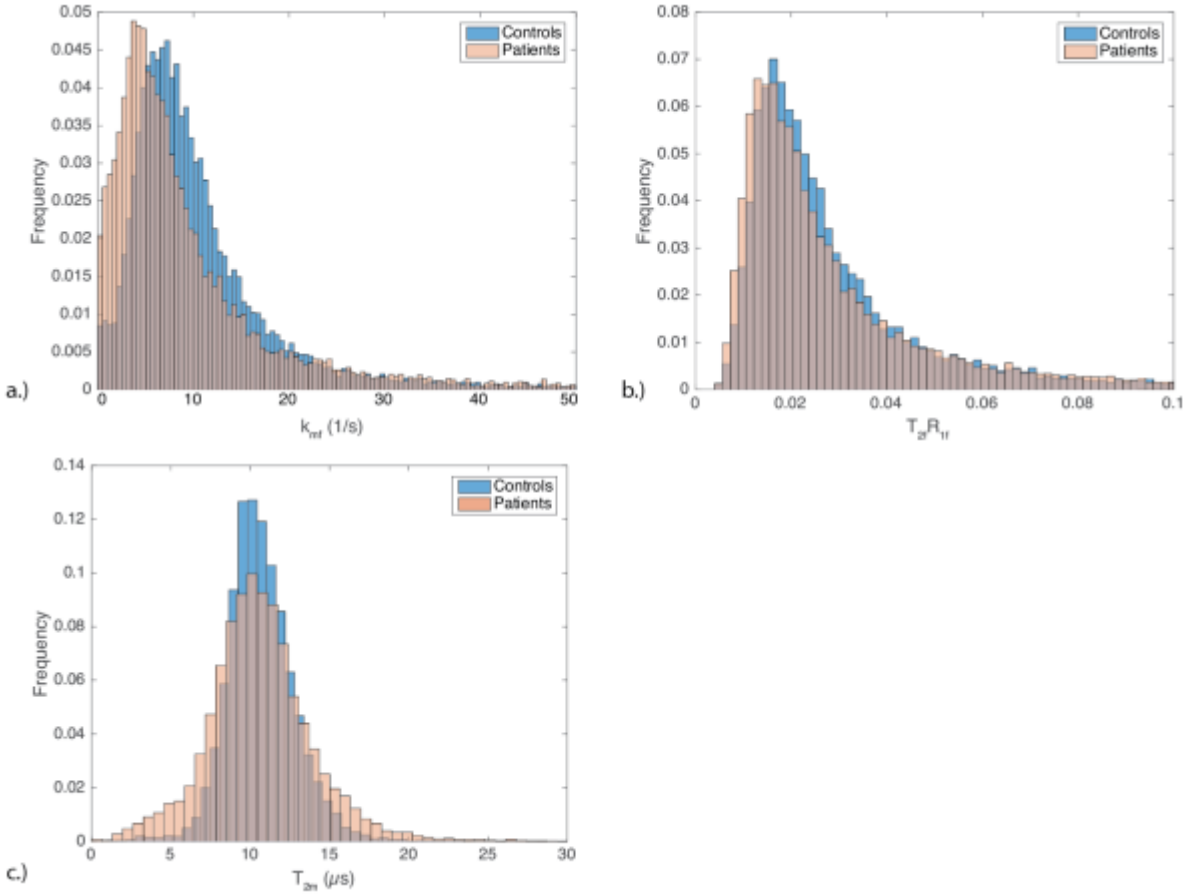

Figure 4.2. Parameter histograms over the whole SC for the healthy controls (blue) and patients (red) derived from (a.) the exchange rate, k_{mf}, (b.) the $T_{2f}R_{1f}$, and (c.) the T_{2m}.

High-Resolution Single Point Data

Anatomical images, R_{1obs} maps, and PSR maps are displayed in Figure 4.3 for a healthy control and a patient with MS, and mean single-point PSR values for the healthy controls and MS patient groups are shown in Table 4.2. Note that the contrast in the PSR is such that WM areas have a higher PSR value (yellow-red) than GM (green), while the CSF exhibits little to no MT effect (dark blue). The average T_{1obs} values for the healthy GM and WM are [GM: 1.37±0.08 s, WM: 1.28±0.08 s], while the average T_{1obs} values in the patient GM, NAWM, and lesions are: [GM: 1.49±,0.16 s, NAWM: 1.38±0.14 s, Lesions: 1.49±0.19 s]. Importantly, several differences can be appreciated when the PSR in the healthy control and patient are compared. In areas associated with a lesion on the anatomical image, we see a concurrent decrease in the PSR of the patient (0.11±0.03).

Importantly, this is reduced compared to the NAWM (0.14±0.04), and the control WM (0.16±0.03).

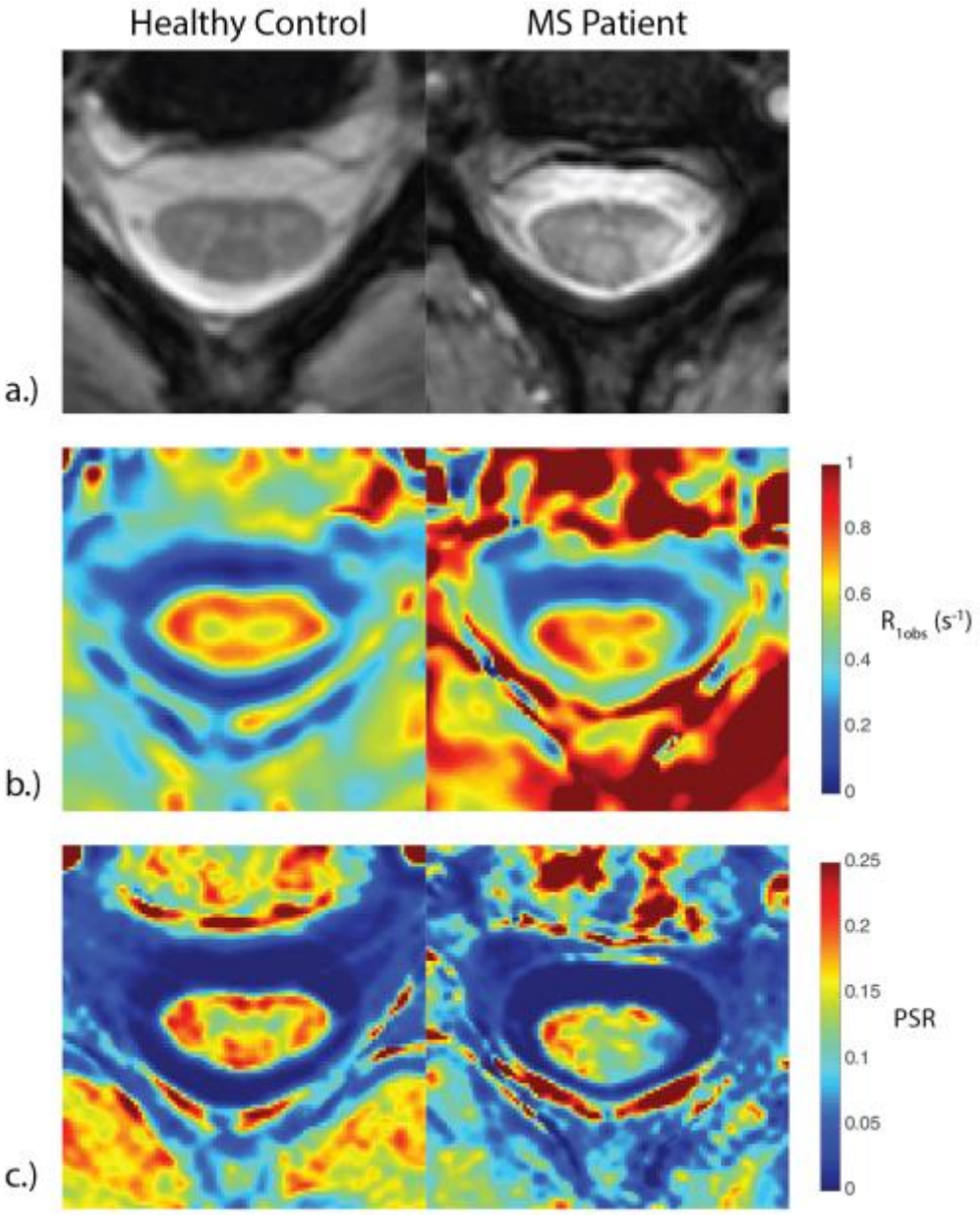

Figure 4.3. Anatomical data (a.), R_{1obs} (b.), and PSR (c.) data for a typical healthy control and patient with MS. Notice the decreased PSR over areas where a lesion is present, and in the areas surrounding these lesions.

Table 4.2 Mean PSR values for white matter (WM), grey matter (GM) and lesion data.

		WM	GM	Les
Controls		0.18±0.01	0.15±0.01	N/A
Patients	Rater 1	0.17±0.03	0.14±0.02	0.14±0.03
	Rater 2	0.16±0.03	0.15±0.03	0.13±0.03

Table 4.3 The 95% confidence intervals, mean difference, Bland-Altman difference, and limits of agreement for the Bland-Altman test for the inter-rater reproducibility in the normal appearing white matter (NAWM), grey matter (GM), and lesion values in the MS patients. The table also displays the p-values for the paired t-test.

	NAWM	GM	Lesion
Mean Difference	0.0006±0.002	0.006±0.01	0.007±0.002
95% Confidence Interval	(-0.003,0.001)	(-0.01,0.0006)	(-0.009,0.02)
Limits of Agreement	(-0.006,0.005)	(-0.02,0.011)	(-0.03,0.05)
p-value	0.480	0.07	0.355
D_{BA}(%)	0.398	3.975	5.267

Table 4.4 Statistical comparisons between the healthy (WM and GM) and patient (NAWM, GM, and Lesions) cohorts using the Wilcoxon rank-sum test for a single rater. Bolded values are considered significant results.

	Healthy WM	Healthy GM	NAWM	Pat GM	Lesion
Healthy WM	1	**<0.001**	0.161	**0.006**	**0.005**
Healthy GM		1	0.052	0.689	**0.046**
NAWM			1	0.094	**0.015**
Pat GM				1	0.139
Lesion					1

The Bland-Altman analysis for the inter-rater comparison is displayed in Table 4.3. The 95% confidence intervals for all tissues overlap zero, indicating there are no significant differences between raters; this is further confirmed by the p-values. Interestingly, the lesions had the largest D_{BA} and limits of agreement, indicating that description of lesion boundaries varied among the raters.

The statistical comparisons between the healthy and patient cohorts from the Wilcoxon rank-sum test displayed in Table 4.4. The WM in the healthy controls was significantly different from both the GM and lesions (p-values <0.01 in all cases). The NAWM was also significantly different from the lesion data (p-values = 0.015), however, the NAWM was not shown to be significantly different from either the healthy WM or the patient GM.

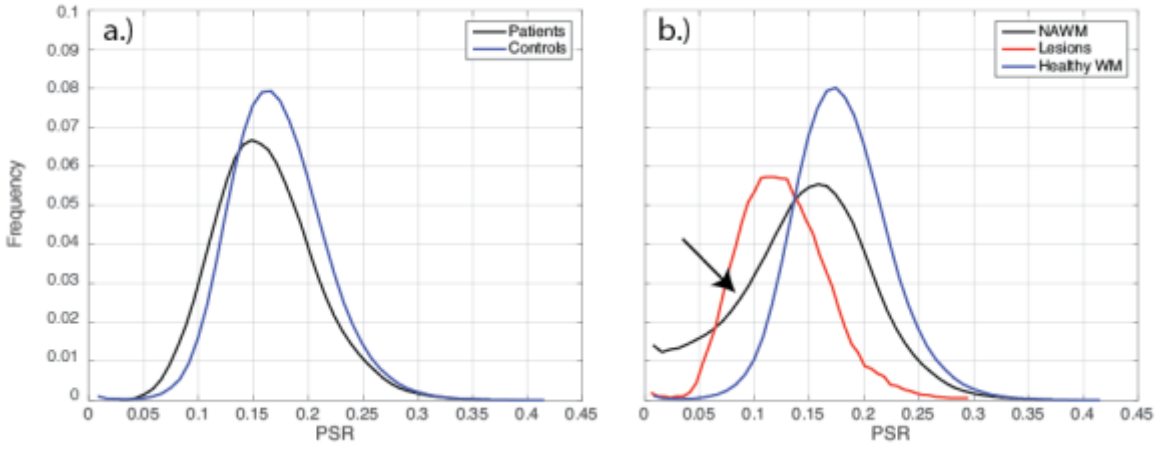

Figure 4.4. Histograms of the high-resolution qMT data for (a.) the whole cord PSR, and (b.) PSR in the healthy WM, NAWM, and lesions (using the ROIs from rater 1). When taken as a whole, the PSR in the controls shows a small, non-significant difference from the control data. However, separating this data into (NA)WM and lesions shows there are marked differences between the control and patient data. In particular, the NAWM appears to have a significant tail on the lower part of the PSR spectrum (arrow).

Figure 4.4 shows histogram of the calculated PSR data derived from the single-point, high-resolution data in the healthy controls and MS patients. The PSR over the entire cord (Figure 4.4a) shows no significant differences between healthy controls and patient with MS, although there is a left shift in the patients. Subdividing the PSR values into healthy WM, NAWM, and lesion data (Figure 4.4b), elucidates several significant differences. First, the lesion PSR values (red line) are shifted (lesion median: 0.121, healthy WM median: 0.173) left, and statistically different from healthy controls (p-value = 0.008). Second, while the NAWM and healthy WM showed no significant differences (p-value = 0.16) the NAWM has an apparent left-skewed tail for lower PSR (arrow), which may indicate that the PSR may be sensitive to WM damage that was

not observed in the anatomical mFFE. Furthermore, removing individual patients did not reduce this tail, indicating a systemic low PSR seen over multiple patients.

4.1.4. Discussion

The goal of this study was to evaluate how applying assumed constraints derived from a full qMT analysis and applied to a single-point qMT method are different in pathology, such as in MS. We compared the calculated constraints for each patient population and evaluated the PSR across patients (using patient-centric assumptions) in the NAWM, GM, and MS lesions, as well as between MS patients and healthy controls. We demonstrate that it is important to evaluate the constraints necessary to perform a data-reduction single-point qMT strategy in a cohort of patient data in order to determine how the parameter maps obtained in a disease model may vary from those obtained in healthy controls.

Even though the constraint estimates were not significantly different between cohorts, k_{mf} approached a significant different (p-value = 0.059) and needs to be considered further. Based on the difference in k_{mf} histogram shapes and apparent downward shift shown in Figure 4.2 we considered the validity of using patient-derived parameter constraints in the patient cohort (rather than those derived for healthy cohorts) for the high-resolution single point analysis. When constraining a model, it is important to understand how these constraints may be biased in pathological conditions. For instance, although the T_{2m} parameter is relatively consistent across controls and patients in MS (37), it has been shown to differ in other disease models. Tozer, et al. (167) , demonstrated that T_{2m} is just one of the parameters that changes significantly in glioma in vivo – PSR was also shown to change significantly. Applying a constrained model, such as the single point method presented here, would suffer from inconsistencies in the assumptions in this disease model. Thus we propose that it is important to evaluate the difference in the assumed constraints when applying them to a patient cohort.

A downward bias was observed in the patient single point PSR data when utilizing the constraints derived from the control population. While this wasn't shown to be significant in this population (p-values ≈ 0.12, one-sided Wilcoxon rank-sum test), this may be attributed to the relatively low EDSS scores present over the patient cohort (mean EDSS: 1.06±1.88). However, comparing the PPMS patient (EDSS score = 5) PSR histogram data between the control-derived

and patient-derived single point data demonstrated a trend towards lower PSR data in the control-derived data set. Therefore, utilizing the control-derived single point PSR may lead to inaccurate estimates of the white matter integrity in the patient population, and thus, may reduce the sensitivity of these measurements to true changes associated with MS. However, before this can be definitively answered, more data in a larger patient cohort with varying levels of clinical deficits is necessary.

Comparing the cohorts using the high-resolution single-point PSR data yielded some interesting insights into the tissue changes resulting from MS. Since most of the patients presented with low neurological deficits (mean EDSS: 1.06±1.88) the manifestation of damage in the spinal cord is expected to also be low. The low-moderate impact on the spinal cord is reflected in the whole-cord PSR histograms, which did not show significant differences between healthy volunteers and patients with MS. However, when separating lesion and NAWM in the patient cohort, differences with healthy control volunteers was noted. In Figure 4.4b, we can see that the NAWM has a long tail towards low PSR. The low PSR in in the NAWM may indicate sub-radiological disease processes such as non-inflammatory processes, which is not observed in the anatomical mFFE. Indeed, it has been shown in animal models that PSR and myelin content are well-correlated (125-127,176). This lower PSR is further illustrated in Table 4.4: the NAWM is trending towards significance when compared with both the control and patient WM, which may indicate both "normal" and demyelinating NAWM.

Magnetization Transfer Ratio

Performing the same analyses as that in Table 4.4 provides significant differences between all control data and all patient data ($p < 0.01$). However, as was stated previously, the MTR is strongly affected by B_1 and B_0 inhomogeneities (6), as well as changes in T_1 (73). When subjected to the same Kruskal-Wallis test as the S_{qMT} (similar to that reported in Table 4.1), it was found that B_1 (p-value: <0.001), B_0 (p-value: 0.047), and R_1 (p-value: <0.001) were all significantly different between the control and patient cohorts, which may account for at least part of the significance seen between the control and patient cohorts. Therefore, it is not possible to derive true estimates of the differences between the control and patient cohorts using the MTR in this study.

Limitations

Although the patients in this study presented with multiple focal lesions, their clinical disability scores were fairly low. While the highest Expanded Disability Status Scale (EDSS) score in the patient cohort was >6, most of the patients had EDSS scores of 1 or 0, which biases correlations that could be performed. Yarnykh, et al. (180) performed a larger study of MS patients with a range of clinical deficits, and although the correlation between brain involvement in MS and clinical disability has been shown to be low (183), they found significant correlations between clinical disability and PSR. In the SC, radiological findings have been shown to be well-correlated with clinical deficits, providing strong indications of clinically isolated syndrome transitioning to MS (171). Therefore, a larger study of the patient population that includes a wider range of disability scores should provide strong correlations between clinical disability and PSR.

4.1.5. Conclusions

This study demonstrated that a patient model of the single point method should be developed independently from a control cohort in order to accurately map PSR data in patients. Our results also demonstrate that the PSR is an important tool to quantify MS, and may provide a more stable measure of the effects of demyelination and axonal damage than can be provided through the MTR or conventional imaging alone. Developing clinically-oriented metrics to quantify tissue pathologies may offer additional insights into disease diagnosis and progression.

4.2. The Lumbar Cord

4.2.1. Introduction

While the spinal cord (SC) is somatotopically organized in cross-section, it is also organized into distinct levels: the cervical, thoracic, and lumbar. Furthermore, each of these areas of the cord interact with specific regions of the body. For instance, the cervical cord interfaces with the neck, arms, and hands, while the lumbar cord controls many lower body functions including the bowel, bladder and legs. As each area of the cord is responsible for sensorimotor interactions at specific dermatome levels, damage to a specific segment can be devastating to the processes that depend upon that area of the cord. MS is one such pathology, and thus will cause increasing clinical impairment over the course of the disease (157,158,184,185). However, while MS has been found to be an increasingly systemic pathology, most studies of MS have been limited to

the brain and cervical spinal cord, with only a few studies in the thoracolumbar spinal cord (TLC). Dorenbeck, et al. (186) showed that MRI provides an accurate, less invasive way to evaluate lumbar spine degeneration. Mori, et al. (187) demonstrated that the lumbar cord (at L5) is one pathway where immune cells may enter the nervous system in a mouse model of MS. They also found indications of inflammation in the mouse model, as well as lactic acid buildup when carried over to human imaging. Another study by Wujek, et al. (188) found that increasing axonal loss throughout the spinal cord was correlated with disability in a mouse model of MS. Overall, as the lumbar cord controls many functions such as bowel/bladder, lower limb, and sexual function, providing an early assessment is vital to preserving patient quality of life.

One challenge associated with characterizing the lumbar cord is translating MRI sequences from the brain and cervical spinal cord to the lumbar regions. This challenge is due to the unique anatomy present in the lumbar cord: the lumbar cord is approximately 1 cm across, and has a higher ratio of GM to WM, requiring high resolution to visualize tissue properties. The difficulties associated with imaging the TLC are further due the unique anatomy whereby the TLC quickly tapers into the conus medularis and cauda equina, separating into the component nerves of the sacral cord and lower limbs.

Quantitative magnetization transfer (qMT) imaging has the potential to quantify the underlying tissue macromolecular structure (2,13,72), and conventional MRI poorly characterizes disease progression over time (159). However, qMT suffers from long scan times; in the brain, collection of multi-power, multi-offset, high SNR, voxel-wise MT z-spectra can result in scan times as long as 30-45 minutes for whole-brain coverage at low resolution (37). As the TLC is smaller than the cervical spinal cord, even higher resolution is necessary, exacerbating the scan time problem. Recently, a new method (37) has been developed that reduces the number of independent MT observations to a single off-resonance observation and a reference measurement (with no RF saturation) by constraining the two-pool qMT model. We have previously shown this approach can be utilized in the cervical spinal cord (see Chapter 3 and Smith, et al. (76)) to provide high-resolution (sub-millimeter in plane) estimates of the macromolecular to free pool size ratio (PSR). Transitioning to the TLC provides information about the tissue properties in this area relevant to disease processes. Thus, the goal of this study was

to translate the single point qMT approach to the TLC to offer high-resolution, rapid estimates of the lower thoracic and lumbar cord. Specifically, I performed in vivo qMT of the TLC in healthy controls using a low-resolution, multi-offset and power MT acquisition, and a second high-resolution, single-point acquisition, similar to what was described in Smith, et al. (76). Next, I imposed a full two-pool model fit in the low-resolution acquisition, and derived constraints to apply in a single-point model of the data. Last, PSR values were compared between the low-resolution and high-resolution data, as well as between the high-resolution data TLC and the high-resolution cervical spinal cord data from section 4.1.

4.2.2. Materials and Methods

The local Institutional Review Board approved this study, and signed informed consent was obtained prior to the examination. Data were obtained from four healthy volunteers (1 male, mean age 26.5±5.5 years) on a 3T Philips Achieva scanner (Philips Healthcare, Best, The Netherlands). A quadrature body coil was used for excitation and a 6 channel CTL whole spine clinical standard phased array was used for signal reception. The field-of-view (FOV) was centered on the thoracolumbar bulge between the T12-L1 vertebral bodies (see Figure 4.5), and spanned, at minimum, the T11 to L2 vertebral levels in all subjects.

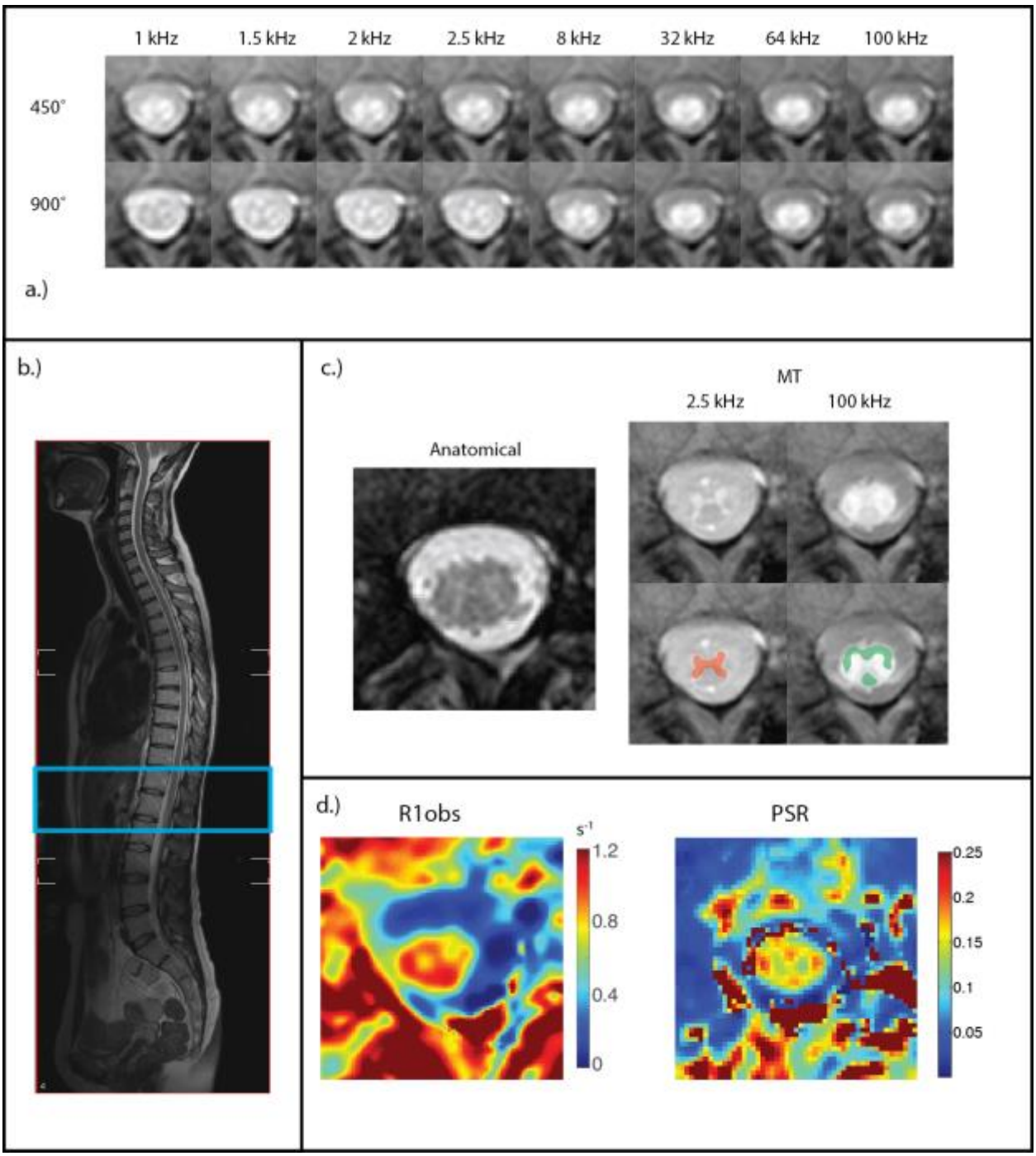

Figure 4.5. (a.) Low-resolution, multiple RF power raw MT-weighted data for the middle slice of the FOV (b.) in a single volunteer. (b.) A T_2-weighted sagittal slice over the full spinal cord. The blue box indicates the scan volume for all quantitative data. (c.) Anatomical mFFE and high-resolution MT-weighted data at the same slice as that in (a.). Notice improved GM/WM contrast. MT-weighted images with ROIs for the GM (red) and WM (green) are shown as well. (d.) R_1, and associated full fit PSR from the data in (a.).

Two MT protocols were performed: 1) a low spatial resolution acquisition (1.5 x 1.5mm^2) at 8 offsets ($\Delta\omega$) and 2 powers (α_{RF}) with a "full-fit" analysis (78,82) and 2) a high-resolution acquisition (0.65 x 0.65 mm^2) at 1 offset and power with a "single-point" analysis (37). For the qMT experiments, MT-weighted images were acquired using a 3D MT-prepared spoiled gradient echo sequence (36), and TR/TE/α = 55 ms/4.5 ms/15˚, with oversampling in the P/A direction of 30/60 mm. Nominal resolution for the low resolution, full model acquisition was 1.5 x 1.5 mm^2 in-plane (reconstructed to 0.6 x 0.6mm^2), and 0.65 x 0.65 mm^2 for the high-resolution, single-point acquisition, over 8 slices (5 mm reconstructed slice thickness). Other parameters were: FOV = 150 x 150 mm^2, and 3 and 4 signal averages for the full-fit and single point acquisitions, respectively. MT weighting was achieved using a 20-ms, single-lobed sinc pulse with Gaussian apodization, α_{RF} = 450˚ and 900˚, and offset frequencies ($\Delta\omega$) = 1, 1.5, 2, 2.5, 8, 16, 32, 100 kHz (chosen to approximately logarithmically sample the expected MT z-spectra (37)). MT weighting for the high-resolution, single-point data was achieved using the same pulse as the full-fit data, but at $\Delta\omega$ = 2.5 and 100 kHz, and an α_{RF} of 900˚. The total scan time for the low-resolution, full-fit acquisition was 19 minutes, 20 seconds, and the scan time for the single-point acquisition was 7 minutes, 23 seconds.

To correct for B_0 inhomogeneities across the spinal cord, B_0 maps were acquired using fast 3D techniques: dual-TE GRE with TR/TE$_1$/TE$_2$ = 50/4.6/6.9 ms and α = 60˚. T_1 mapping was performed using a multiple flip angle (MFA) acquisition with TR/TE = 20/4.6 ms and α = 5, 10, 15, 20, 25, 30˚. A high-resolution multi-echo gradient echo (mFFE) scan was also performed and all echoes were averaged to generate a high contrast reference image for registration (163). The mFFE was obtained with TR/TE/ΔTE = 700/7.2/9.3 ms and α = 33˚, with a slice thickness of 3 mm, and a gap of 2 mm. Nominal in-plane resolution was 0.65 x 0.65 mm^2. Acquisition times were 34 seconds for the B_0 map, 2 minute 30 seconds for the T_1 map, and 5 minutes 30 seconds for the mFFE, resulting in a total acquisition time of ≈36 minutes.

Image Processing

All data analyses were performed in MATLAB R2015b (MathWorks, Natick, MA). Prior to data fitting, all images were cropped to an area immediately around the spinal cord and co-registered to the mFFE volume using the FLIRT package from FSL v5.0.2.1 (FMRIB, Oxford, UK) (145,146).

The co-registration was limited to translation and rotation (±5˚) in-plane only (i.e. translation in x and y, and rotation about the z-axis). Following co-registration, qMT parameter maps were generated for each volunteer and patient using the full-fit qMT model described in Yarnykh (78) & Yarnykh and Yuan (82). This model contains six independent parameters: R_{1m}, R_{1f}, T_{2m}, T_{2f}, PSR = M_{0m}/M_{0f}, and $k_{mf} = k_{fm}/PSR$. It has been shown that the signal dependence on R_{1m} is weak (19,34); therefore, it was set to R_{1f} for fitting purposes. R_{1obs} ($1/T_{1obs}$) maps were reconstructed by regressing MFA data to the spoiled gradient echo signal equation in the steady-state (148). The resulting maps were then used to determine the parameter R_{1f}, as described by Yarnykh (78) & Yarnykh and Yuan (82). The remaining parameters were estimated for each voxel by fitting the full-fit qMT data to the two-pool MT model (78,82). For all fitting, the nominal offset frequency was corrected in each voxel using B_0.

It has been shown that T_{2m}, k_{mf}, and the product $T_{2f}R_{1f}$ can be fixed during the fitting process because they exhibit relatively constant values across tissues (82). Note that T_{2f} can be determined from the constrained $T_{2f}R_{1f}$ value and an R_{1f} estimate from the MFA data, while k_{fm} can be determined using the first-order mass action kinetics (127). Thus, these constraints result in a model where PSR is the only free parameter. To estimate reasonable fixed parameter values for the single-point qMT analysis, $T_{2f}R_{1f}$, k_{mf}, and T_{2m} were estimated over all voxels from all subjects, and histograms were created over the spinal cord for all slices from the full-fit analysis. The median of each histogram was chosen to enter into the single-point qMT analysis. Then, using the median values of the constraints and the optimized offset and power (determined in Chapter 3), the high-resolution, single-point data were analyzed to generate high-resolution PSR maps.

Mean PSR values for the single-point and the full-fit scans were calculated from regions of interest (ROI) for each slice in the GM and WM, as shown in Figure 4.5c. ROIs were placed manually using MIPAV (NIH, Bethesda, MD) for each slice of each subject. The mean values from each ROI were then compared between the full fit and single point data, and between the lumbar cord and cervical cord data (see Chapter 3).

4.2.3. Results

Data Acquisition

Representative MT-weighted images in a single volunteer at the L1 level are shown in Figure 4.5a, with the corresponding PSR maps and R_1 shown in Figure 4.5c. All quantitative imaging was performed in a volume centered around the thoracolumbar bulge, as shown in Figure 4.5b. High-resolution MT-weighted data is shown in Figure 4.5c at the same level as that in Figure 4.5a. Note that the cropped images in Figure 4.5a and Figure 4.5c-d are derived from the registration process (c.f. Section 4.2.2). Figure 4.5c shows ROI placement for white matter (green) and grey matter (red). The PSR and R_{1obs} are shown in Figure 4.5d: notice that the GM and WM are clearly distinguishable in the PSR map, with the GM containing a lower PSR (and R_{1obs}) in general. However, also note that the fitting near interfaces (such as the SC and CSF interface) is poor, which was also seen in the cervical cord (Chapter 3).

Full Fit Constraints

Figure 4.6 shows whole cord histograms for each estimated qMT index derived from the full-fit analysis over all healthy controls. All histograms display a single peak, with all histograms outside of the T_{2m} parameter displaying a left-skewed profile. Interestingly, the PSR has a peak near 0.12, which is more normally associated with GM. This peak can either be due to the increased GM to WM ratio in the lumbar cord, compared to the cervical cord, or it could arise from partial volume effects associated with the low-resolution of the full fit data. In order to perform the single point analysis, median values were taken for each parameter to be constrained (k_{mf}, $T_{2f}R_{1f}$, and T_{2m}): k_{mf} = 7.37 s^{-1}, $T_{2f}R_{1f}$ = 0.024, and T_{2m} = 12.5 µs. Table 4.5 displays the median parameter values from the TLC and the cervical spinal cord median parameter values from the control cohort from section 4.1. The k_{mf} and T_{2m} are different between levels, however, this may be just due to the lower number of volunteers in the TLC, and thus, more data must be collected to fully evaluate these differences.

Table 4.5 Median parameter values derived from the full fit analysis to be used as constraints for the single point analysis in the TLC and cervical spinal cord. Cervical spinal cord values were taken from the control cohort from section 4.1.

	k_{mf} (1/s)	$T_{2f}R_{1f}$	T_{2m} (μs)
TLC	7.37	0.024	12.5
Cervical spinal cord	8.45	0.024	10.66

Single Point qMT

The high-resolution MT-weighted data, and full fit and single point PSR for two volunteers are shown in Figure 4.7 at the L1 level. Note that the contrast in the WM regions displays higher PSR values (orange-red) compared to that in the GM regions (green-yellow), while the CSF exhibits little to no MT effect (blue). The single point high resolution PSR shows contrast between the WM and GM more clearly than the full fit PSR maps, and also agrees relatively well with the size and location of the anatomical definition shown in the MT-weighted data (left panel). In control one, the full fit PSR appears lower than the single-point PSR due to the increased influence of GM in the full fit data relative to the single point data. Furthermore, the single point PSR is more continuous near tissue boundaries compared to the full fit estimation, as can be seen in the ventral part of the spinal cord abutting the CSF in control two. There is less ambiguity of the location of the cord/CSF boundary in the single point PSR compared with the full fit PSR. This increased conspicuity is likely due to the fact that the constraints reduce the number of independent free parameters necessary to fit the PSR, reducing the inconsistencies of fits that would occur at these interfaces due to movement and other in vivo confounds.

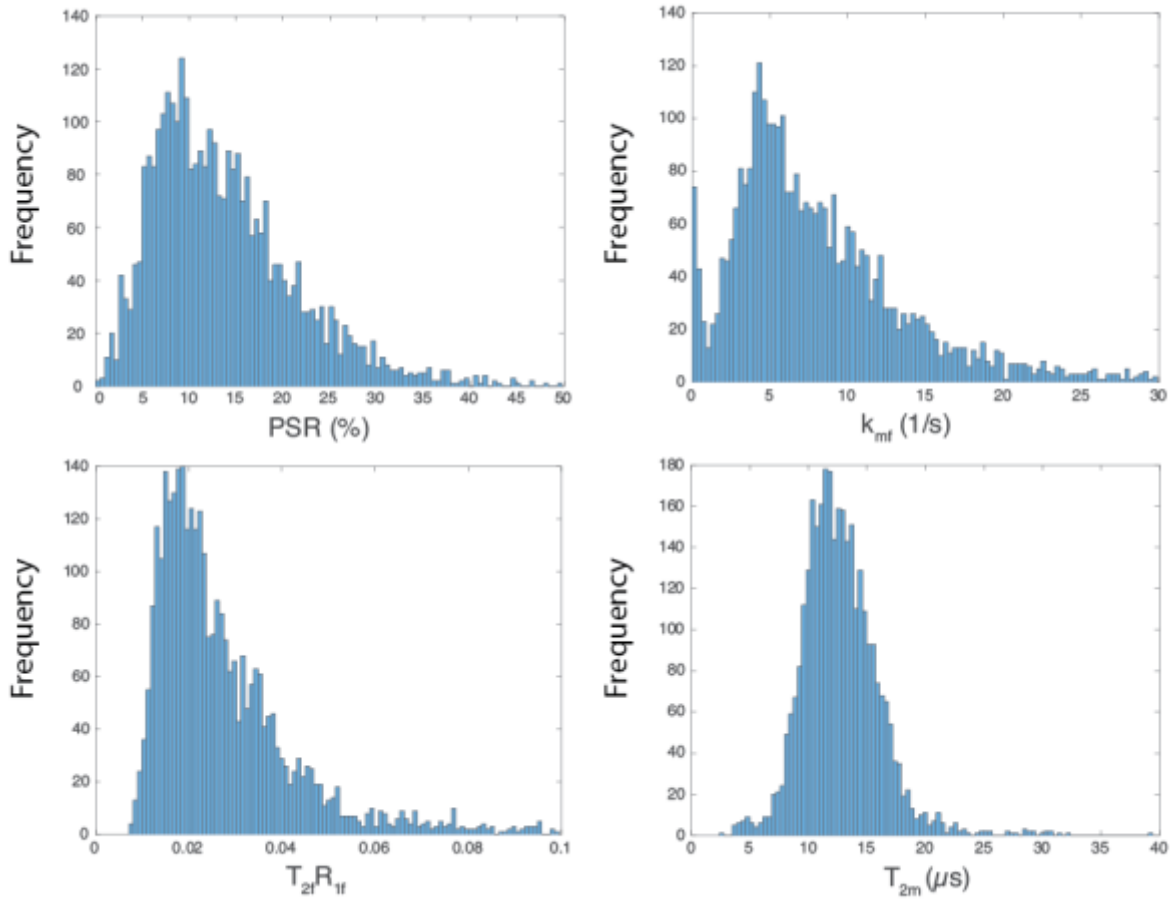

Figure 4.6. Histograms of the full fit model parameters for the control group subjects for (a.) the PSR, (b.) the exchange rate constant k_{mf}, (c.) $T_{2f}R_{1f}$, and (d.) T_{2m} over the total number of voxels in all subjects.

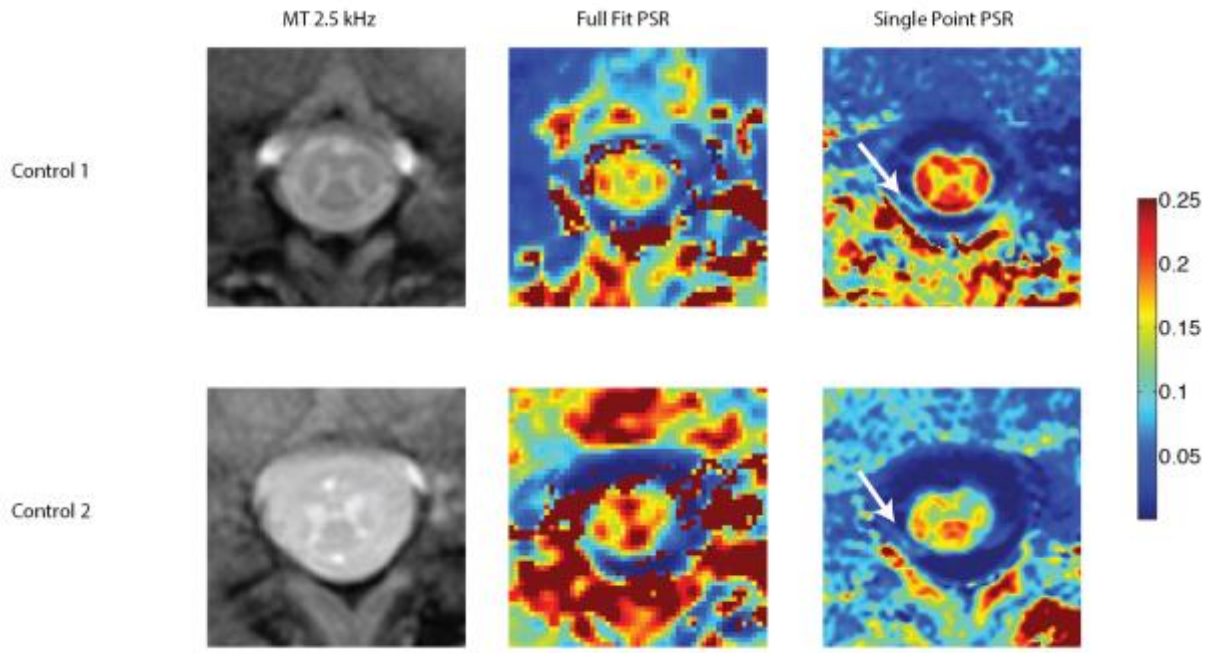

Figure 4.7. MT-weighted data, full fit PSR, and single point, high resolution PSR for two controls. Notice the clear delineation between the cord and CSF in the single point data, as well as the GM/WM differences. Also note the dorsal roots protruding from the dorsal GM (arrows).

Table 4.6 shows the mean PSR values for WM and GM in the lumbar SC for the full fit and single point data, with a comparison to the single point data in the cervical SC from section 4.1. We can see that the full fit and single point data in WM and GM agree with one another. Furthermore, the standard deviation in the measures also decreased in both WM and GM, which may be due to the reduction of motion-induced errors near tissue boundaries in the single point fit compared with the full fit. Importantly, the WM and GM data match closely to the data obtained in the cervical spinal cord. However, due to the low sample size, statistical comparisons did not yield significant differences.

Table 4.6 Mean PSR values for the full fit and single point PSR in the white matter and grey matter ROIs for all volunteers. The cervical spinal cord (C-Spine) PSR from section 4.1 is also provided as a comparison.

	White Matter	Grey Matter
Full Fit PSR	0.18±0.09	0.16±0.07
Single Point PSR	0.18±0.05	0.14±0.03
C-Spine PSR	0.18±0.01	0.15±0.01

4.2.4. Discussion

The goal of this study was to demonstrate that the single-point qMT method can be easily applied to other anatomies outside of the cervical SC and brain. I compared the PSR across volunteers and between grey and white matter. My results demonstrate the PSR can be consistently obtained in the lumbar SC of healthy volunteers. The ability to generate these high-resolution PSR maps from only a single qMT measurement may increase the clinical utility of this method, as well as provide an opportunity to further study the effects of demyelinating diseases, such as MS, in the TLC.

To the author's knowledge, this is the first in vivo qMT study of the lumbar cord in humans. However, several other studies have investigated the effects of MS-related neurodegeneration in animal models. In particular, Wujek, et al. (188) found that axonal loss throughout the entire length of the cord is correlated with clinical disability in a mouse model of MS. Therefore, developing a method that can reliably determine pathological changes in macromolecular content non-invasively is paramount for early detection and management of MS. The data shown here may provide an avenue to quantitatively characterize the SC at all levels, and thus, may help improve detection of MS before large-scale clinical symptoms are manifest.

Although this study was only performed in four subjects, importantly, I show that this methodology can be easily applied in any difficult-to-image anatomy. The single-point method, when applied and constrained appropriately, can provide an opportunity to examine anatomies such as the TLC anatomies at high-resolution, and thus, provides an opportunity to characterize underlying tissue physiology. Furthermore, since the long ascending and descending tracts in the

spinal cord should be similar between the cervical and lumbar cord, the similarity between the cervical and TLC estimates of PSR is promising. Additionally, Bosma and Stroman (189) performed a diffusion tensor imaging (DTI) study along the entire length of the SC in healthy controls, and found that DTI indices in both GM and WM were consistent along the entire length of the cord, further demonstrating that the PSR estimates obtained in the cervical and lumbar regions of the cord may be equivalent as well.

Although this study demonstrated the ability to apply the single point method in the difficult to image area of the TLC, it was limited through several factors. Most importantly, the low number of volunteers limited the statistical power of this study. The low number of volunteers also potentially biased the constraints derived from the full-fit parameter estimates, as more volunteers would provide a more representative distribution of data. Of similar importance was the lack of B_1 mapping techniques. Although B_1 images were acquired, their values were inconsistent, and would routinely provide estimates that were on the order of 80% or below, and were found to be as low as 20% in some volunteers. As the amount of saturation was consistent across volunteers, I conclude that the B_1 mapping technique I utilized was not well-suited to estimate B_1^+ and B_1^- from the plank coil. More accurate techniques for B_1^+ mapping must therefore be pursued. For instance, the Bloch-Siegert B_1 mapping method has been shown to be relatively robust to B_0 inhomogeneities, chemical shift, and MT effects (190,191), and can be made relatively insensitive to B_1^- effects (192).

4.2.5. Conclusions

The results of this study demonstrate the feasibility to translate single-point qMT into the human thoracolumbar cord in vivo. The development of this technique may provide an opportunity to further research the lumbar cord and determine its relationship to clinical measures of spinal cord pathology. Future work involves collecting data in more volunteers, and applying this methodology in patients suffering from lower limb, bladder, and/or bowel dysfunction to determine how the thoracolumbar cord may play a role in these disease processes.

Chapter 5: Rapid, Whole-Brain, High-Resolution Inhomogeneous Magnetization Transfer in vivo

5.1. Introduction

Magnetization transfer (MT) has shown great promise for imaging in the central nervous system (CNS), as it has emerged as an MRI technique capable of characterizing myelin changes (12,13). These, and many other studies of white matter (WM) disease have reported a relationship between MT contrast and WM integrity, which may then relate to macromolecular pathology and tissue damage in diseases such as multiple sclerosis (MS) (157,158,184,185).

The MT phenomenon has its origin in the existence of both semisolid molecules and water-like protons which are present in most tissues (such as the myelin in WM). Although semi-solid protons in tissue cannot be imaged directly, due to their short T_2 (≈10 ms), there is a constant interplay between the semi-solid and water-like protons through exchange of spin information, which is termed the MT effect (33). This exchange can be exploited to indirectly study the semisolid component (also called "pool") by using radiofrequency (RF) irradiation to selectively saturate the broad semisolid proton resonance. Through the MT effect this saturation will be transferred throughout the tissue via spin diffusion and exchanged (through dipole-dipole and direct chemical exchange) with the unsaturated water, thereby attenuating the observed water signal (54,55). The MT effect, and by extension, the water signal attenuation due to MT has been classically quantified with the magnetization transfer ratio (MTR), however, while sensitive to macromolecular concentration, the MTR is not a specific measure of tissue macromolecular composition (e.g. myelin (34,73)), and not easily reproduced across scanners, hardware, vendors, and field strengths (6) due to the differences in RF pulse shapes, sequence timing and saturation powers. Additionally, while quantitative methods have been developed that obviate these concerns and may more directly measure myelin content (12,13,125-127), they are hampered by long scans times, and are still non-specific to myelin changes.

Recent studies have demonstrated that complex macromolecular structures, such as those found in the myelin sheath, are different in their organization, packing, and exchange phenomena, and thus, their MT effects may be more complex than the conventional two pool

model (113,193). The increased complexity was originally described as inhomogeneous broadening of the lipid line shapes, and thus has been termed inhomogeneous MT (ihMT) (112,113). ihMT has demonstrated a remarkable specificity to white matter when compared with the conventional MTR. Indeed, Varma, et al. (112) and Girard, et al. (113) demonstrated that the white matter to grey matter ratio in metrics of ihMT imaging were significantly greater than the white matter to grey matter ratio in the MTR. However, existing ihMT studies in vivo have deployed pulse trains for narrow-bandwidth, high power RF saturation, which due to the requirement of steady state saturation, many investigators have focused their studies on only single slice methods due to the long scan times necessary to acquire sufficient signal to appropriately study the ihMT phenomenon (112,113,193). There is currently only one report of a 3D variant of the ihMT imaging method (194): this 3D method requires a customized sampling of k-space, and application of MT saturation only near the center of k-space in order to reduce the specific absorption rate (SAR) to a level acceptable to image in an acceptable scan time. Thus, in order to improve coverage, the proposed 3D ihMT method is challenging to employ clinically as it requires extensive modification of the acquisition and reconstruction software on the scanner. Conventional MT methods have recently utilized a spoiled gradient echo (SPGR) approach with high power saturation and high-duty cycle TRs to build a steady state signal over several TRs (35), however, this methodology has not been expanded to ihMT imaging. Therefore, in this chapter I have developed a 3D, whole brain ihMT imaging methodology that takes advantage of the theoretical framework formalized originally by Sled and Pike (35,36). I show that this method requires minimal changes to the pulse sequence design, and thus can be easily deployed on any scanner to acquire rapid, high-resolution, whole-brain ihMT images at 3T.

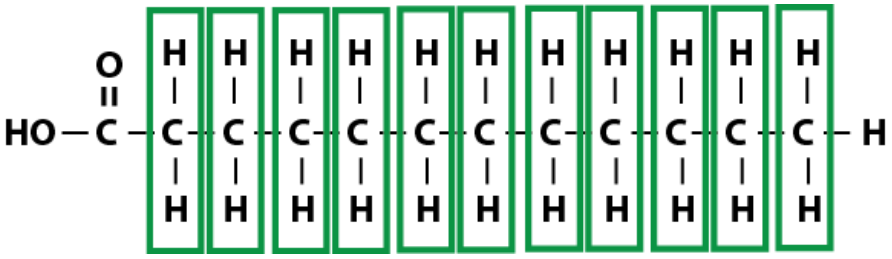

Figure 5.1. The structural formula for a methylene chain. Each pair of hydrogen atoms in the methylene chain (represented by the green boxes) can be approximated as coupled spin-1/2 protons. These effectively form a spin-1 system.

5.2. Theory

5.2.1. Basics of ihMT: Broadening from inhomogeneous lines

The original theory proposed by Varma, et al. (112) theorized that the ihMT effect arises from inhomogeneously broadened lineshapes. Large membranes, such as the myelin sheath in white matter, may not be homogeneously broadened (112). This is due to the fact that lipids and proteins within the membrane of myelin will fully rotate only around an axis perpendicular to the surface of the membrane (195). Furthermore, spin diffusion in membrane lipid molecules are significantly reduced with respect to outside the membrane because the small fluctuations in the bond angles of the lipids inhibits this motion (196). Because these mechanisms of homogeneous broadening are absent from myelin membranes, it is believed that inhomogeneous broadening occurs in these membranes (112). This has lead Varma et al. (112,113) to develop inhomogeneous MT (ihMT).

5.2.2. Basics of ihMT: Contrast specific to spin-1 systems

An alternate theory of the ihMT effect proposed by Manning, et al. (197) describes the ihMT effect as a result of differences in the magnetic properties of water and lipid chains. This theory can be explained by understanding the biochemical nature of the long methylene chains present in most lipid bilayers, such as that in myelin. Protons in lipid bilayers have unique so-called thermal averaging due to their restricted motion within these lipid chains: the methylene chains spin, translate, and vibrate along the chain's length which results in an averaged dipolar coupling rate between the protons (112,193) (rather than a specific dipolar coupling), which alters the

saturation diffusion throughout lamellar structures. The result of these motion-restricted methylene chains in highly organized lipid structures (see Figure 5.1), such as myelin, is that the methylene chains effect the dipolar coupling such that it appears as an approximate spin-1 system derived from the "coupled" spin-1/2 systems of the protons (197), and the resulting energy spectrum has three spin states and two transitions between states. By applying a modified MT saturation pulse (or series of pulses), (see Figure 5.2), it is possible to selectively highlight this spin-1 system.

5.2.3. The ihMT Experiment

An ihMT experiment is performed using a saturation pulse (or pulse train) 1) applied at +Δω (Figure 5.2a), 2) at -Δω (Figure 5.2b) and 3) at both +Δω and -Δω simultaneously (Figure 5.2c). In vivo, the motion-restricted and dipolar averaged spin-1 system undergoing saturation transfers this saturation to the observable free water system (as with conventional MT), and results in a concurrent reduction in the water signal (197). The three observations are combined as a difference between the ± saturation and the MTR (i.e. difference between conventional MTR and ihMT) and defined as the inhomogeneous MTR (ihMTR) Varma, et al. (112):

$$ihMTR = \frac{S(+\Delta\omega) + S(-\Delta\omega) - 2S(\pm\Delta\omega)}{S_0} \qquad 5.1$$

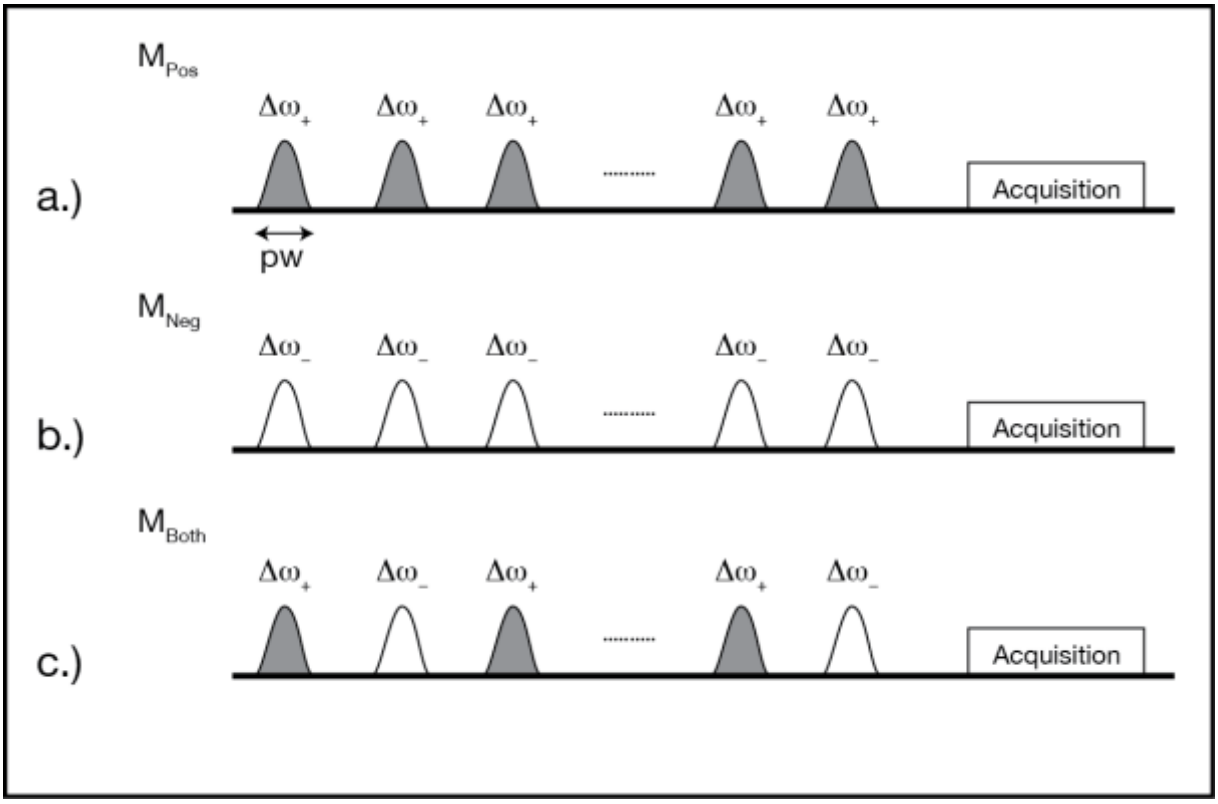

Figure 5.2. A typical pulse train ihMT experiment. In (a.) a series of pulses are played out at an offset Δω, similar to a normal pulse train MT experiment. Next, in (b.), that same series of pulses is played out at -Δω. Lastly, in (c.), the offset of each pulse in the pulse train is alternated between +Δω and -Δω. Adapted from Varma, et al. (112).

5.2.4. A Quantitative SPGR Model

The biochemical interactions embodied in the ihMT phenomenon can be formalized by modifying the two-pool Bloch-McConnell equations, as has been shown in earlier experiments (3,198,199). Instead of using a two-pool model, as shown in Equation 1.17, an extra dipolar order pool is introduced that is in exchange with the macromolecular pool. Importantly, interaction between the dipolar and macromolecular pools can only occur when off-resonance irradiation is applied (193), resulting in the following set of equations:

$$\frac{d\boldsymbol{M}}{dt}=\begin{bmatrix} -\frac{1}{T_{2f}} & -\Delta\omega & 0 & 0 & 0 \\ \Delta\omega & -\frac{1}{T_{2f}} & -\omega_1 & 0 & 0 \\ 0 & \omega_1 & -(R_{1f}+k_{fm}) & k_{mf} & 0 \\ 0 & 0 & k_{fm} & -(R_{1m}+k_{fm}+R_{rfm}) & R_{rfm} \\ 0 & 0 & 0 & R_{rfm}\left(\frac{\Delta\omega}{D}\right)^2 & -\left(\frac{1}{T_{1D}}+R_{rfm}\left(\frac{\Delta\omega}{D}\right)^2\right) \end{bmatrix}\boldsymbol{M}+\begin{bmatrix} 0 \\ 0 \\ R_{1f} \\ R_{1m}*PSR \\ 0 \end{bmatrix} \quad 5.2$$

where $\boldsymbol{M}=(M_x^f, M_y^f, M_z^f, M_z^m, \beta)$, β is the inverse spin temperature associated with the dipolar order, $T_2^{f,m}$ are the transverse relaxation times for the free (f) and macromolecular (m) pools, $R_1^{f,m}=1/T_1^{f,m}$ are the longitudinal relaxation constants for each pool, $\Delta\omega$ is the RF pulse offset with respect to water, ω_1 is the RF pulse amplitude, k_{mf} and k_{fm} are the exchange rates between the macromolecular and free pools, and vice versa, respectively, R_{rfm} is the RF saturation rate for the macromolecular pool, and is defined as:

$$R_{rfm}=\pi\omega_1^2 g_m(2\pi\Delta\omega) \quad 5.3$$

is the normalized line shape of the macromolecular pool, D is the second moment of g_m, and T_{1D} is the relaxation time of the dipolar order. However, if the power is simultaneously divided between +Δω and -Δω with the same total amplitude, it can be shown that the dipolar order term becomes zero, which eliminates the dipolar order pool (193), reducing Equation 5.2 to:

$$\frac{d\boldsymbol{M}}{dt}=\begin{bmatrix} -\frac{1}{T_{2f}} & -\Delta\omega & 0 & 0 \\ \Delta\omega & -\frac{1}{T_{2f}} & -\omega_1 & 0 \\ 0 & \omega_1 & -(R_{1f}+k_{fm}) & k_{mf} \\ 0 & 0 & k_{fm} & -(R_{1m}+k_{fm}+R_{rfm}) \end{bmatrix}\boldsymbol{M}+\begin{bmatrix} 0 \\ 0 \\ R_{1f} \\ R_{1m}*PSR \end{bmatrix} \quad 5.4$$

The approximation in Equation 5.4 has been shown to be valid for ihMT quantification, as long as the MTR asymmetry is less than 4% (200).

5.3. Materials and Methods

All numerical simulations and data analyses were performed with scripts written in MATLAB 2015b (MathWorks, Natick, Massachusetts), unless otherwise noted.

5.3.1. Simulations

The full Bloch equations from Equations 5.2 and 5.4 were simulated to steady state using tissue parameters typical for WM: PSR = 0.2, k_{mf} = 10 1/s, T_D = 3.3 ms, T_{1f} = T_{1m} = 700 ms, T_{2f} = 70 ms, and T_{2m} = 10 µs. A pulse train sequence using parameters from Varma, et al. (193) was compared

against the proposed pulsed steady state SPGR sequence to demonstrate that each sequence is producing similar contrast, and the ihMTR for each method was plotted to illustrate these similarities. Specific pulse parameters are listed in Table 5.1.

Table 5.1 Pulse Parameters used for the simulated data. The TR for the pulse train was set at 3 seconds, similar to Varma, et al. (193), while the TR for the pulsed SPGR data was derived from the time to simulate the full MT acquisition with a 10 ms readout time.

	Pulse Train	Pulsed SPGR
MT Pulse length (ms)	0.5	5
Number of MT Pulses	1000	8
MT Pulse train Duty Cycle	0.25	1
TR (ms)	3000	52
	Common to Both Sequences	
Max $B1_{MT}$ (μT)	4, 8, 12	
Excitation flip angle (degrees)	10	
Excitation pulse length (ms)	2	

5.3.2. MRI Experiments

All MRI experiments were performed on a 3T Philips Achieva (Philips Healthcare, Best, The Netherlands) system. A two-channel multi-transmit body coil was used for excitation. All ihMT experiments resulted in a set of 4 images: MT weighted images at $+\Delta\omega$, $-\Delta\omega$, $\pm\Delta\omega$, and a reference image at 100,000 kHz (S_0).

Phantom experiments

Imaging was performed on a set of phantoms consisting of several different concentrations of agarose (1, 2, 3, and 4% by mass), as well as TreSemme™ hair conditioner, which has been described as having macromolecular and lamellar structure similar to WM (112,201). A phantom consisting of phosphate buffered saline (PBS) was also included as a control. These phantoms were immersed in a container filled with water to reduce B_0 inhomogeneities, and a 16 channel neurovascular coil was used for signal reception. The nominal in-plane resolution of 1.15 x 1.15

mm^2 (reconstructed to 0.86 x 0.86 mm^2), slice thickness of 5 mm, with a SENSE factor of 2 (RL direction), with an in-plane field of view (FOV) of 220 x 220 mm^2.

Two ihMT experiments were performed: a 2D, pulse train acquisition using the MT parameters from Varma, et al. (193) (the gold standard), and a 3D pulsed steady state experiment. The pulse train experiment consisted of an MT preparation with a multi-shot EPI readout, with an EPI factor of 5, TR/TE/ α = 2800 ms/5 ms/15˚, and 4 averages. The MT preparation was applied for 2 seconds with 0.5 ms pulses every 1.5 ms (for a duty cycle of 0.25), with: $B_{1,max}$ = 8 μT, $|\Delta\omega|$ = 7 kHz, and used a single-lobed sinc pulse with Gaussian apodization. The total acquisition time for the 2D pulse train experiment was approximately 18 minutes.

The pulsed steady state sequence consisted of an 3D SPGR sequence with multi-shot EPI readout with the following parameters: EPI factor of 3, TR/TE/α = 198 ms/4.0 ms/10˚, and 4 averages, a 5 mm slice thickness over 10 slices, covering 50 mm through-plane. The MT saturation pulse consisted of eight, 5 ms pulses with a duty cycle of 1.0, $B_{1,max}$ = 8 μT, and $|\Delta\omega|$ = 7 kHz, and used a single-lobed sinc pulse with Gaussian apodization. Additionally, the sequence duty cycle (i.e. the rate of saturation played out over the acquisition) is approximately 0.25, which is the same sequence duty cycle used in previous acquisitions by Varma, et al. (112). The total acquisition time for the pulsed SPGR experiment was approximately 14 minutes.

In vivo experiments

The local Institutional Review Board approved this study, and signed, informed consent was obtained prior to the examination. Data were obtained on six healthy controls (all female, age range 21 – 37 years, mean age 26.3 ± 5.7 years). A 32-channel head coil was used for signal reception. All parameters for the in vivo experiments were kept constant to the phantom imaging, except the in vivo imaging employed 2 averages. The FOV for all sequences is: 220 x 202 x 100 mm^3, with nominal in-plane resolution of 1.15 x 1.15 mm^2 (reconstructed to 0.86 x 0.86 mm^2), slice thickness of 5 mm, and 20 slices, with a SENSE factor of 2 (RL direction), and covered the entire brain volume. The total acquisition time for full brain coverage was 19 minutes.

A sagittal volume in one of the volunteers was also collected over the corticospinal tract, brain stem, and upper cervical spinal cord to demonstrate that this technique is specific to neurological tissue. This acquisition covered 10 slices used the same parameters as the axial

acquisition, with the exception of the following parameters: in-plane FOV: 250 x 250 mm^2, nominal in-plane resolution of 1.5 x 1.5 mm^2 (reconstructed to 1 x 1 mm^2), and TR/TE = 218/3.5 ms.

5.3.3. Image Processing and Analysis

Phantom Experiments

The MTR($\Delta\omega$ = +7 kHz) and ihMTR were first calculated in both experiments, and, the mean ihMTR and MTR of each phantom (and each z-phase encode for the 3D pulsed experiment) for each experiment was determined. For the 3D experiment, the ihMTR and MTR were plotted over slices two through nine in all of the MT phantoms (conditioner and agarose phantoms) as well in order to demonstrate that the ihMTR effect is equivalent over the full volume. The first and last slice were excluded due to interference from air and the phantom holder.

In-vivo experiments

Before fitting, all in vivo images were co-registered using tools from FSL v5.0.2.1 (FMRIB, Oxford, UK) (145,146). First, all images were brain-extracted using the brain extraction tool (BET) (143,144), then all of the subject-level data was co-registered to the S_0 image using FLIRT (145,146). Next, the ihMTR and MTR(+7 kHz) were calculated for each subject before performing group-level co-registration.

Sagittal volume inter-subject registration was performed by drawing a manual mask over the entire brain and spinal cord using MIPAV (NIH, Bethesda, MD) to preferentially register the neurological tissue; these images were then registered to the S_0 using FLIRT and registration matrices were generated. The registration matrices were then used to co-register the unmasked data to the S_0 image and the ihMTR was calculated.

Axial volume group-level registration was performed by using the non-linear FNIRT package from FSL (147,202,203). The S_0 image from each subject was registered to a reference subject – choosing the first subject as the reference – and then these warping fields were applied to the ihMTR and MTR to move all of the data into a single subject space. The resulting registered MTR, ihMTR, and S_0 images were imported into MATLAB for further processing. Due to the changes in brain volume between volunteers, as well as registration errors caused by slight changes in positioning within the different volunteers, the first five and last two slices were

excluded from the analysis, resulting in 13 slices spanning from the superior portion of the brain stem to the superior cerebrum.

Statistical Analysis

The mean and standard deviation for the MTR and ihMTR values were calculated for grey matter (GM) and WM over all subjects by thresholding the ihMTR for each subject below and above 10% of the maximum ihMTR for each subject, respectively. A statistical analysis was then performed using the Wilcoxon rank-sum test to compare WM vs GM for both the ihMTR and MTR. Measures of the ihMTR and MTR images were also taken in the following regions of interest (ROIs): the splenium of the corpus callosum (Sp) and the posterior leg of the internal capsule (IC) to represent WM, and the putamen (P) and the occipital calcarine cortex (OCC) to represent GM (see Figure 5.8a). The ratio of WM to GM was then calculated for each combination of WM and GM ROI (i.e. Sp vs P, Sp vs OCC, IC vs P, and IC vs OCC) for both the ihMTR and MTR. The one-tailed Wilcoxon rank-sum was then used to determine if the WM/GM ratio in the ihMTR was statistically greater than that in the MTR. Statistical significance for all comparisons was defined as $p < 0.05$.

5.4. Results

5.4.1. Simulations

The ihMT from the simulations for the pulsed SPGR and pulse train are shown in Figure 5.3. Although the effect is smaller in the pulsed approach compared to the pulse train (ΔihMTR(7 kHz) = 1.1%) there still exists a significant ihMTR for a given B_1 value. The reduction in ihMTR signal is most likely due to the large delay between TRs, which will provide more time for relaxation effects to play a role. Additionally, the spectral location of the peak for the ihMTR can be seen to vary in offset frequency change offset value as the B_1 is modified: this is most likely due to changes in the Z-spectrum of each respective pulse, and how efficiently the dipolar order transfers magnetization to the macromolecular pool at a given B_1 power. Importantly, the pulse train data produces values similar to those seen in simulations by Varma, et al. (193).

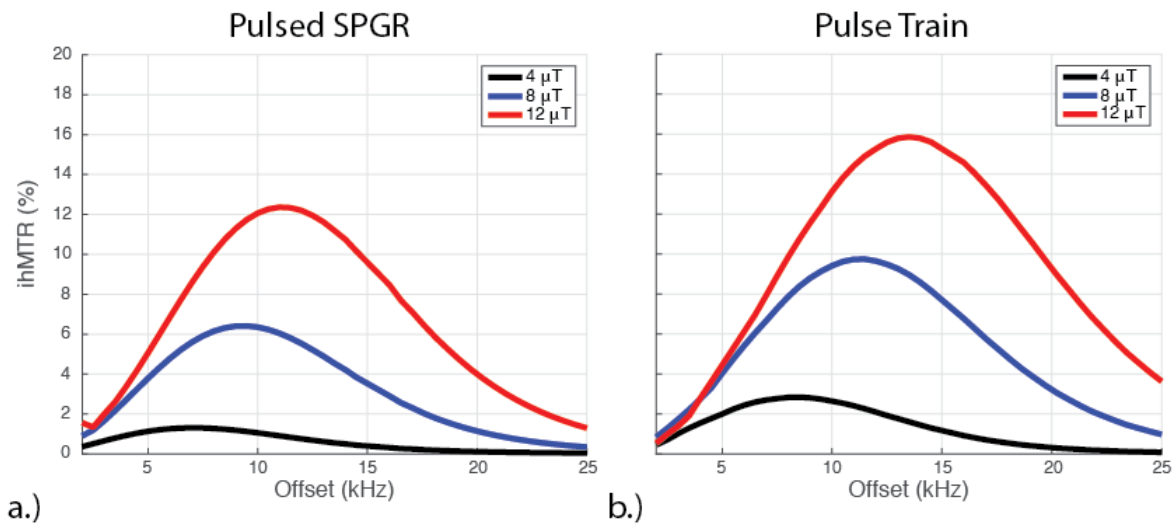

Figure 5.3. Simulation results for the ihMTR found from the (a.) pulsed SPGR approach and the (b.) pulse train approach using Equations **5.2** and **5.4**.

5.4.2. Phantoms

Phantom data for the two central slices of the phantom using the SPGR experiment, and data from the gold standard pulse train experiment are shown in Figure 5.4. While all of the MT phantoms illustrate varying levels of MTR contrast, only the conditioner displays ihMTR contrast. This is due to the lipids present in the conditioner, allowing it to form a series of spin-1 systems, and thus producing ihMT contrast. Furthermore, this contrast is consistent across all slices, which illustrates that the pulsed SPGR sequence can be consistently deployed across large volumes. Finally, the pulsed approach and the gold standard pulse train approach show very similar ihMT contrasts, demonstrating that these methods are producing similar results. This is in contrast to the MTR which shows contrast for all agarose and hair conditioner phantoms.

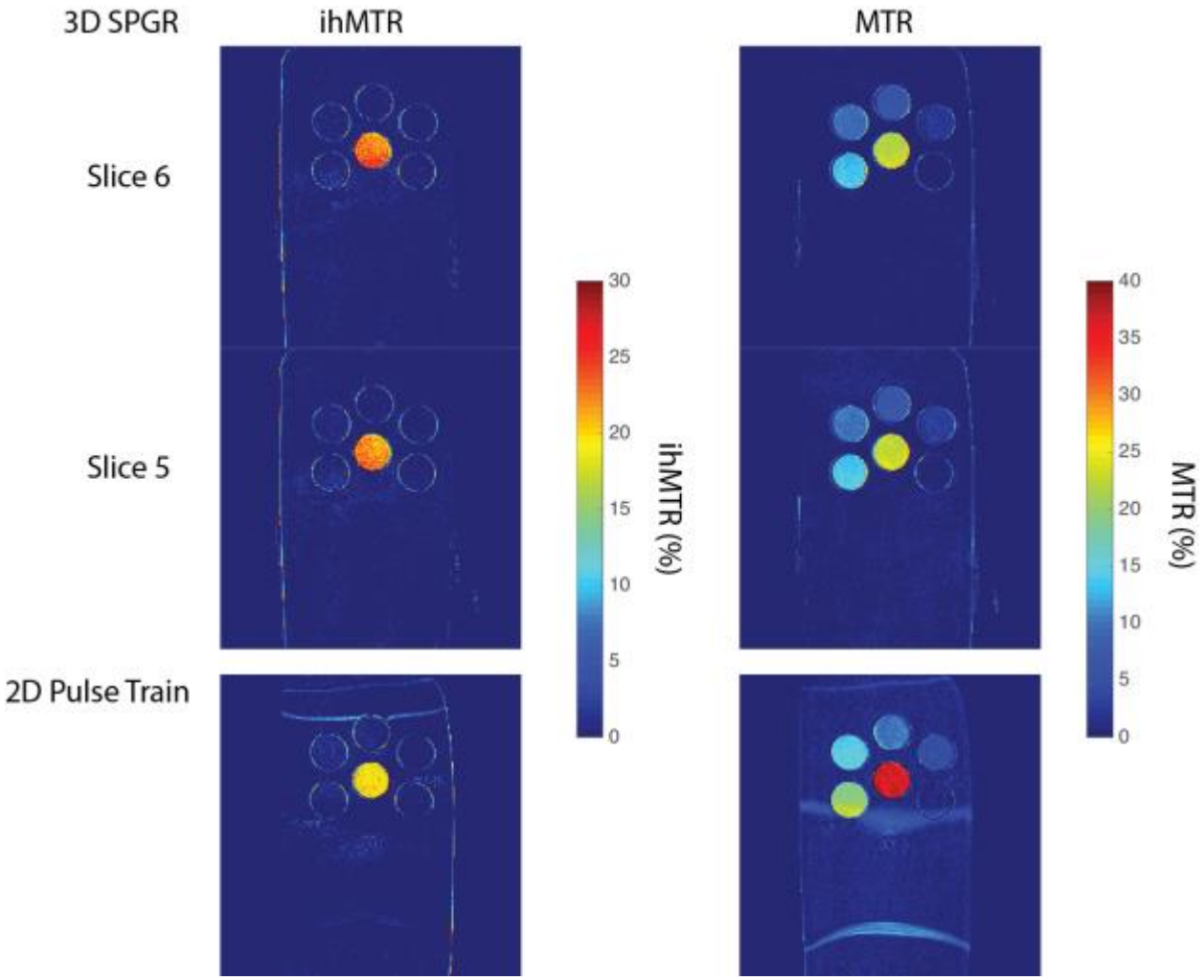

Figure 5.4. ihMTR and MTR data at 7 kHz for the central two slices for the phantom experiment using a pulsed SPGR experiment, and using a pulse train acquisition. The conditioner phantom is the central phantom, and the outer phantoms are (clockwise from the bottom left): 4% agarose, 3% agarose, 2% agarose, 1% agarose, and PBS. All of the MT phantoms (agarose and conditioner) show varying amounts of MTR, however, the conditioner produces a strong ihMTR, with no significant ihMTR appearing in the other phantoms. Additionally, the ihMTR effect is visually equivalent between the SPGR and pulse train acquisitions.

Looking more quantitatively at the data in Figure 5.5, where the mean MTR and ihMTR values from each of the phantoms are plotted over all slices, illustrates that the ihMTR from the pulsed approach is consistent across the volume. While the MTR displays the expected variance in parameter values across phantoms, the ihMTR is only significantly present in the conditioner phantom (therefore agarose phantoms were not plotted), indicating that the spin system is indeed different in the conditioner than in agarose. Furthermore, plotting the mean value from

the 2D pulse train approach (19.3%±1%, red bar) against the mean values for the pulsed approach (Figure 5.5b) confirms that the pulsed acquisition and gold standard pulse train acquisition are similar. Lastly, the ihMTR difference between the gold standard and SPGR sequences are displayed, further illustrating that we see very similar (and within error) levels of contrast across the volume.

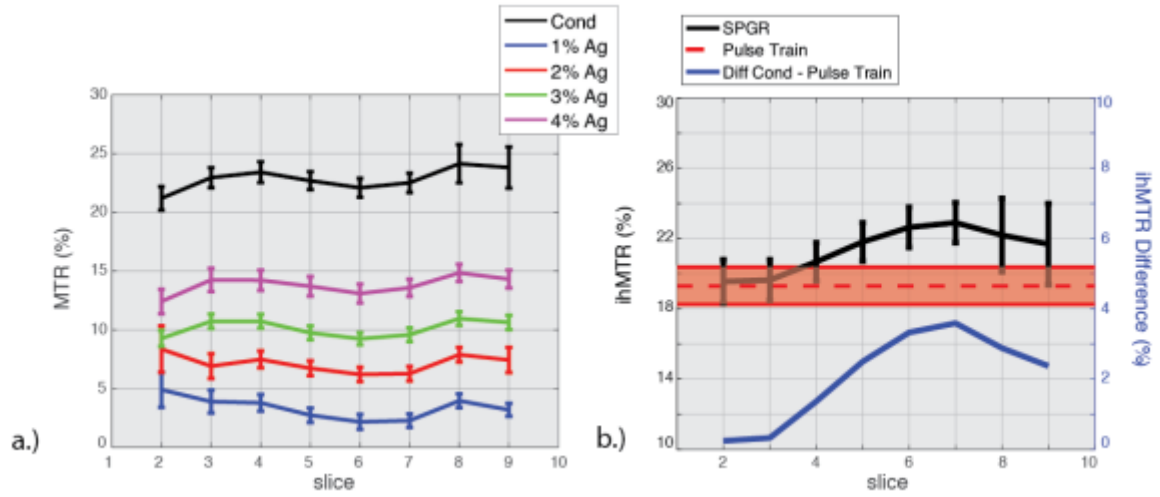

Figure 5.5. Plots of the (a.) MTR and (b.) ihMTR at 7 kHz from the second to ninth slice for the SPGR experiment. The MTR shows the expected variance in values between the different phantoms, while the only the conditioner displayed significant ihMTR contrast. The ihMTR from the pulse train acquisition (mean - dotted line, standard deviation – red shaded area) is plotted to illustrate that both methods are producing similar results. A difference curve is also included in (b.) (right axis) to more directly quantify the difference between the SPGR and pulse train experiments.

5.4.1. In Vivo

Figure 5.6a shows the ihMTR over the full measurable volume for a single volunteer, spanning from the superior brain stem and midbrain to the superior cerebrum. The ihMTR appears to be specific to white matter, showing high contrast in the main WM tracts within the brain, with little to no contrast in the surrounding GM (WM ihMTR = 4.84%±1.8%, GM ihMTR = 1.35%±0.79%, > 50% reduction in ihMTR signal from the WM to the GM). This is in contrast to the MTR (Figure 5.6b), which is not specific to WM, displaying relatively high MTR values across neurological tissue (WM MTR = 18.86%±1.78%, GM MTR = 16.40%±2.59%, ~ 10% reduction). Furthermore, taking a

sagittal slice that encompasses the brain stem and spinal cord illustrates the specificity of the ihMTR to WM throughout the CNS (Figure 5.6c). The brain stem, cerebellum, and spinal cord form the only coherent ihMTR contrast below the cerebrum, with most other high ihMTR contrast attributed to motion or registration artifacts. This can be seen particularly well in the tongue, where there are significant edge effects due to movement between different acquisitions, but no major contrast within the tongue.

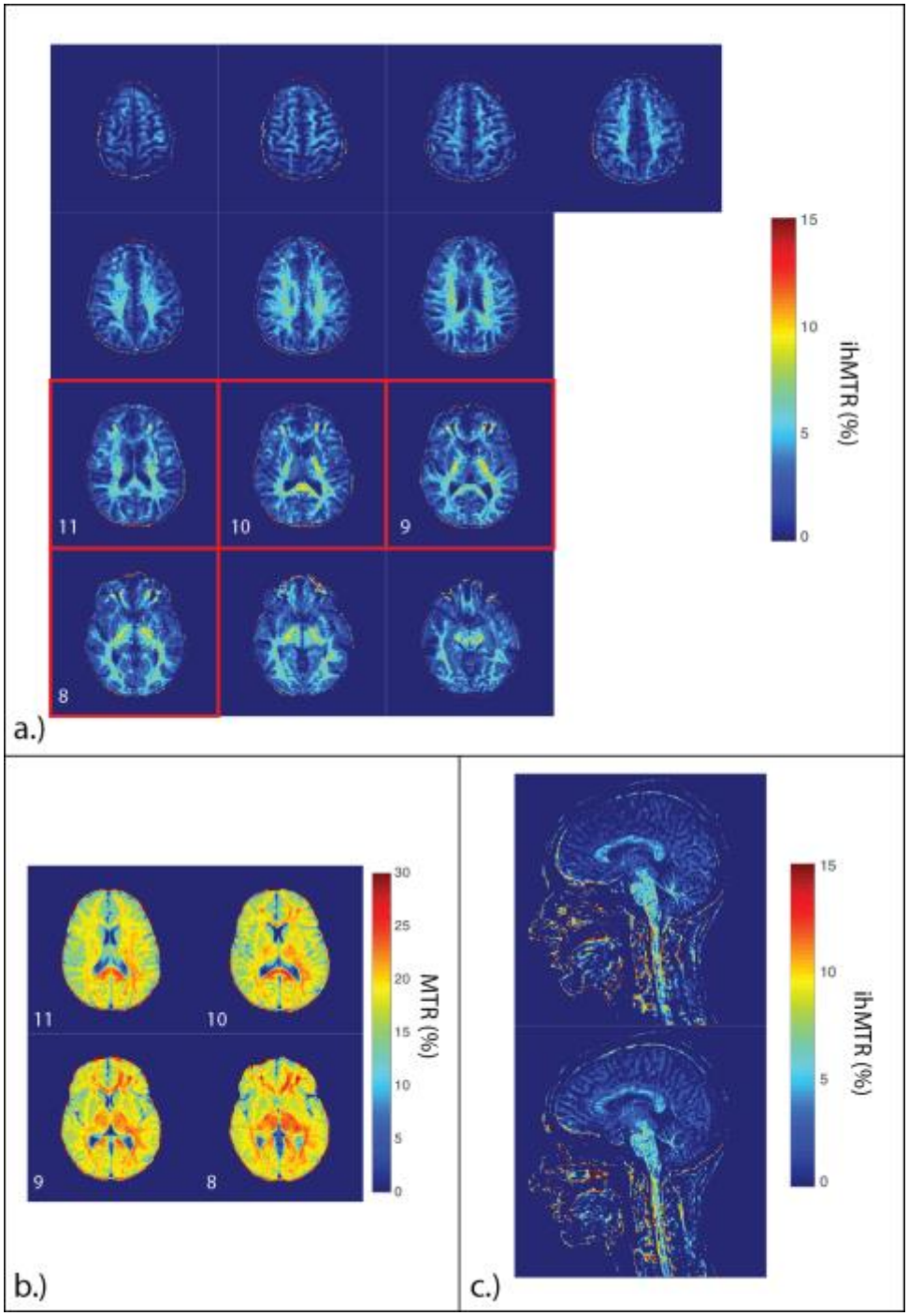

Figure 5.6. (a.) ihMTR over the full brain, spanning from the superior brain stem to the superior cerebrum. The ihMTR shows marked specificity for the WM throughout the entire brain. (b.) MTR in the central slices of the brain (corresponding to the slices as those in red boxes in (a.). Notice the reduced specificity for WM compared with the ihMTR. (c.) Sagittal ihMTR, illustrating that the ihMT effect can be seen to traverse the full brain stem and cervical spinal cord. Notice that WM areas, such as the corpus callosum, brain stem, and spinal cord, are much brighter than the surrounding tissue, due to their much higher myelin content.

Threshold Analysis

The 10% threshold is illustrated visually in Figure 5.7 and the mean ihMTR values for WM and GM over all subjects are listed in Table 5.2 with the MTR for comparison. The 10% threshold appears to separate the GM and WM consistently across slices, and the low threshold value demonstrates that the ihMTR may be specific to myelin content. Furthermore, the WM and GM are well-separated over all slices, indicating that the pulsed SPGR method can be consistently applied across a volume of interest, and is not restricted to a pulse train acquisition. Statistically, the ihMTR was found to be significantly different between GM and WM ($p = 0.002$), while the MTR was not statistically different ($p = 0.132$), indicating that the ihMTR and MTR are providing different values from one another.

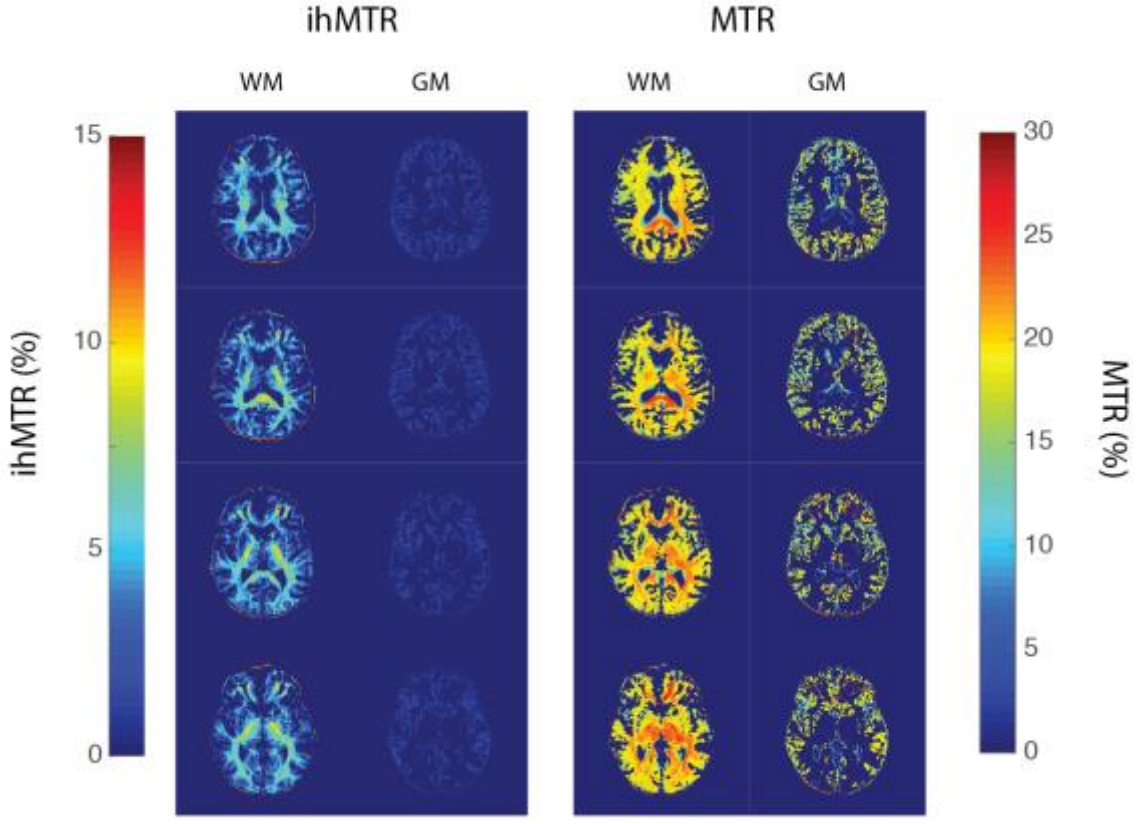

Figure 5.7. The result of the threshold analysis separating GM and WM. A threshold of 10% of the maximum ihMTR in each volunteer was used to separate GM and WM and can be seen in the left set of images. The GM/WM separation was also applied to the MTR (right set of images) to compare to the ihMTR.

Table 5.2 Mean ihMTR and MTR values over the full brain, and the results from the Wilcoxon rank-sum test. The ihMTR is statistically different between GM and WM over the whole brain, while the MTR has shown to not be statistically significant.

	ihMTR (%)		MTR (%)	
	Mean	p-value	Mean	p-value
White Matter	4.84±1.8	0.002	18.86±1.78	0.132
Grey Matter	1.35±0.79		16.40±2.59	

A plot comparing the WM/GM ratio between the ihMTR and the MTR, with a representative slice showing the locations of the ROIs is shown in Figure 5.8. The WM/GM contrast between the ihMTR and MTR was found to be significantly greater in the ihMTR in all cases ($p < 0.01$), indicating that the ihMTR is more clearly distinguished between WM and GM when compared to the MTR.

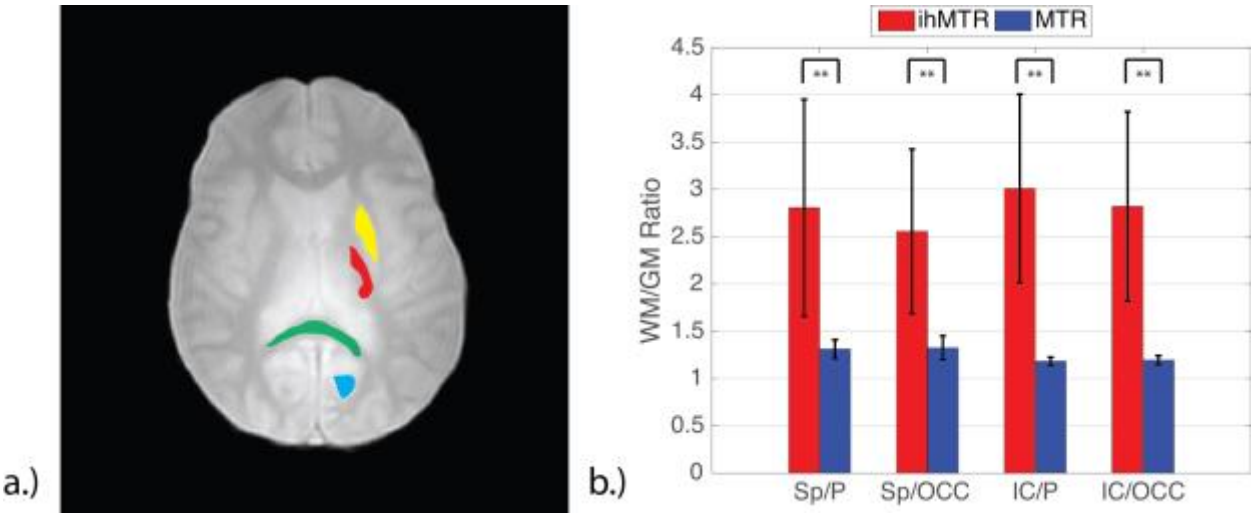

Figure 5.8. a.) Reference (S_0) image with ROIs in the splenium (green), internal capsule (red), putamen (yellow), and occipital calcarine cortex (blue). Bar plots of the WM/GM ratio in several different ROIs for both the ihMTR and MTR, with errors bars of the standard deviation across subjects – **$p < 0.01$ (one-tailed rank-sum test). Notice that the WM/GM ratio is significantly different in all cases, indicating that the contrast between the WM and GM in the ihMTR is more apparent than that in the MTR.

5.5. Discussion

MT experiments have exemplified marked sensitivity to many different pathologies, including MS (13,23-29), Lupus erythematosus (30), dementia, Huntington's, Parkinson's (31), and schizophrenia (32). However, researchers have not yet been able to demonstrate that MT is specific to myelinated tissues, and thus, cannot definitively determine the underlying cause of diseases shown to damage WM. ihMT has demonstrated that it may provide indices more specific to myelin (112,113,197), however, previous acquisition techniques are not applicable to human disease models since they cannot be deployed over a large volume in a reasonable scan time. The research presented here has rectified this, and provides an opportunity to start evaluating ihMT in the presence of disease.

5.5.1. Generalized ihMT Equations

While this new contrast has been developed and applied in several different volumes (112,204,205), the biophysical mechanisms underlying this contrast have not been extensively explored. Varma, et al. (193) were able to demonstrate that this contrast depends on a dipolar reservoir present in systems that contain lamellar structures, however they only developed equations that can be satisfied after a long saturation pulse, limiting their applicability towards understanding the pulsed acquisition strategy we have developed. In order to evaluate the effect of sequence design on the ihMT effect, we have therefore expanded their theories here to a set of ODE's (Equations 5.2 and 5.4) which can be applied across many different types of acquisition strategies, and have demonstrated that the ihMT effect can be obtained using a variety of pulse sequence types (Figure 5.2). This is an important development, as it provides a generalized model that is not dependent on any particular acquisition strategy, and thus this technique will not be limited by hardware specifications, acquisition volume, or sequence design.

5.5.2. Comparison of gold standard with pulsed SPGR technique

Comparing the pulsed acquisition strategy with the gold standard pulse train strategy demonstrated several important improvements. Although the readout was different in the gold standard acquisition, the MT preparation was similar to one of the sequences applied in Varma, et al. (193), and yielded contrast similar to that seen previously (112). Importantly, all ihMT techniques demonstrated marked specificity for the conditioner, which is considered a lamellar

structure (as seen in Figure 5.4). However, applying the gold standard acquisition strategy took significantly longer than the pulsed approach, and could only be applied over a 2D cross-section of the volume, whereas the pulsed approach covered the entire volume of interest. Additionally, even applying the sequence used by Varma, et al. (112) in the phantoms here would result in a 2.5 minute scan per slice, which translates to a 25 minute scan over the same volume the pulsed scan covers, which almost doubles the effective scan time.

One additional added benefit of utilizing a pulsed SPGR sequence is that there are less opportunities to incur image distortion due to B_0 and B_1 inhomogeneities, which can accrue in fast acquisition strategies such as the single shot EPI or HASTE sequences. An SPGR sequence also provides more SNR per unit time relative to the HASTE sequence used previously, which provides an opportunity to move to higher resolution while still holding the SNR above what can be achieved in a HASTE sequence in an equivalent amount of scan time. Employing small field of view, fast imaging strategies may also provide additional scan time improvements without adversely distorting the image, as was seen here with an EPI factor of 3.

5.5.3. Whole Brain ihMT

Moving from a 2D acquisition to a 3D acquisition makes this method a viable alternative to conventional MT imaging. There are minimal differences (maximum difference = 3.5% ihMTR) between the 2D pulse train acquisition and the 3D pulsed SPGR acquisition in the phantoms, as seen in Figure 5.5b. Importantly, this trend is seen across the entire scan volume, indicating that the pulsed SPGR experiment is a viable alternative to the 2D experiment for generating ihMTR contrast.

While important for developing a new acquisition type, and for understanding the underlying scientific processes controlling ihMT, a 2D acquisition would be difficult to employ in pathology. Most diseases present in the CNS are heterogeneous, and require a large volume acquisition in order to accurately characterize the tissue. Therefore, it is important to be able to employ a 3D acquisition to cover the full extent of the pathological tissue. Importantly, the increased SNR from a 3D volume acquisition will provide an opportunity to reduce the reconstructed slice thickness to more accurately characterize pathology. Previous experiments have required quite large slice thicknesses (on the order of 10 mm) (112,113,193,204) to produce

enough SNR to capture the ihMTR effect. However, many pathologies may require higher resolution to accurately characterize their effects in vivo. In particular, WM diseases, such as MS, can present with small, localized lesions (12), which may be difficult to fully characterize when using a 2D acquisition strategy.

The acquisitions here were optimized to produce the maximum ihMTR contrast in the minimum scan time possible. This can be seen from the simulations in Figure 5.3, where an 8 μT pulse at 7 kHz was selected. However, additional optimization of the pulse sequence may be possible to maximize the ihMT contrast. My work here found that increasing the pulse power and number of pulses produced negligible increases in ihMTR due to the concurrent increase in TR to account for the higher SAR. Additionally, while we used a 5 mm slice thickness here to reduce scan time, the through-plane resolution can be easily reduced without significantly sacrificing SNR in order to characterize pathologies which require high resolution.

While previous methods have shown ihMT acquired over a full volume, they did not employ standard imaging methods in order to achieve this effect (194). This limits the applicability of this method, as it requires modifying both the acquisition and reconstruction significantly in order to reduce the SAR to shorten the TR. At this time, this is the only technique using a pulsed SPGR strategy to produce the ihMT effect over a large volume.

5.5.4. Quantitative MT

The evolution of this new contrast type follows a trend seen previously with conventional MT imaging. Sled and Pike (35) developed the first SPGR MT experiments, which reduced the scan time by a large margin, providing an opportunity to move to more quantitative methods. Previous methods required large pulse trains or a special RF coil that would produce a continuous wave irradiation (4,5). These have seen much use since their inception in the brain (13,35-37,74,78,206,207), spinal cord (14,38,76), optic nerve (77), and muscle (152).

Due to the specificity of ihMT to coupled spin-1/2 systems, quantifying this effect in vivo may improve our understanding of how this effect characterizes these systems, as well as how this effect changes in pathology. Although ihMT has been shown to be more specific to myelin than conventional MT imaging, the ihMTR is still only be semi-quantitative in nature, as it is dependent on B_0 and B_1, similarly to what has been seen with the MTR (6). Therefore, to truly

test the specificity of this technique, quantitative ihMT methods must be employed. While this has been attempted previously (193), the researchers here utilized a pulse train methodology, and therefore, could only collect a full quantitative dataset over a single slice. Moving to the acquisition strategy here would provide an opportunity to cover a large volume, or collect data more rapidly to build a larger quantitative dataset than what was collected previously.

5.5.5. Specificity to Myelin

This acquisition has shown a marked specificity towards myelin. This can be seen in Figure 5.6, where there is a large contrast difference between the WM and GM, and in Table 5.2, which indicates significant differences between WM and GM using the ihMTR, but no significant differences using the MTR. Additionally, the statistical tests (see Figure 5.8) comparing the GM/WM ratios in the ihMTR and MTR demonstrate that the ihMTR is may be more selective for WM than the MTR. However, in order to truly test this specificity, more studies need to be employed, particularly in pathologies such as MS, where there is a significant loss of myelin. While conventional MT and qMT have proven sensitive to myelin, they have not definitively shown this was specific to changes in myelin alone. While studies have shown that some qMT parameters are more specific to myelin in certain disease models (177), there may be other biophysical parameters, such as water infiltration, that may bias these decreases. Therefore, quantifying the ihMT effect may provide parameters more specific to these changes in myelin content (such as the T_{1D} parameter), which are not affected by other confounding factors.

5.5.6. Limitations

While the ihMTR is an important improvement to conventional MT imaging, it has several limitations. First, since the ihMTR calculation involves a subtraction, high SNR must be obtained, or any coherent signal may be overshadowed by noise, which implies that higher resolution imaging may require additional signal averaging to effectively calculate the ihMTR. Additionally, the ihMTR is also biased by B_1 inhomogeneities, which prevented this study from studying the cerebellum, as B_1 inhomogeneities introduced a bias in some volunteers which significantly affected our inter-subject registration. Moving towards more quantitative methods would solve this problem, however, this also requires optimizing the protocol to account for the increased scan time necessary to collect enough data to completely characterize the ihMT model (193).

While this method uses an EPI train with an EPI factor of 3 to decrease scan time, other methods of decreasing scan time may be employed. For instance, reducing the number of pulses in the pulse train may serve to decrease the scan time, however, this may also decrease the ihMTR contrast. Additionally, alternate methods to employ the ihMT pulse may be utilized, such as switching the frequency between TR's and not between individual pulses, may provide similar contrast; however, this has not been explored in detail, and would be the subject of future studies.

5.6. Conclusions

This work has demonstrated for the first time that the ihMT technique can be applied over a large scan volume in a reasonable scan time in vivo. We demonstrated that we receive similar metrics using a pulsed SPGR strategy to that observed using a long pulse train in both simulations and in phantoms. This technique was then demonstrated in healthy controls over the full brain volume. Future work involves applying this technique in patients with MS, and developing a quantitative method of evaluating this technique in vivo.

Chapter 6: A New Combined Model for Quantifying the CEST Effect in the Presence of MT

6.1. Introduction

Chemical exchange saturation transfer (CEST) is a magnetic resonance imaging (MRI) technique sensitive to the presence of low concentration mobile protons exchanging with water. While chemical exchange has been understood for decades using nuclear magnetic resonance (NMR) techniques (17,51,53,55), recently chemical exchange has been exploited as an imaging method (92). CEST techniques are sensitive to several different small, soluble metabolites, such as the backbone amide protons of proteins and peptides (88). Its versatility as a contrast mechanism has been demonstrated in many different clinical applications, including multiple sclerosis (208), cancer (42,209,210), and stroke (45,93,211-213), and thus CEST has added a new dimension to the detection and monitoring of these and other pathologies.

CEST contrast can be generated in a similar manner to saturation-based MT techniques (33), but with several important differences. In a typical saturation MT technique, a radiofrequency (RF) irradiation pulse is applied at a frequency off-resonance to water. This saturation is then transferred to water through both dipole-dipole exchange and direct chemical exchange, resulting in an observed signal attenuation. Because MT is primarily concerned with saturating the broad spectral linewidth (3) of the semi-solid components, the sequences employed by MT imaging will typically employ short pulses. However, because the solutes of interest have small, relatively narrow resonance frequencies, CEST imaging must utilize a much narrower RF irradiation bandwidth (which translates to a longer pulse width or pulse train) to be sensitive to these solutes. Additionally, CEST contrast is generated through direct chemical exchange; however, MT contrast and CEST contrast are not mutually exclusive events, thus a bulk water proton can experience both types of exchange and as a result will produce a similar observable signal attenuation. Therefore, CEST contrast will be corrupted in the presence of semi-solid components. Last, the CEST z-spectrum is a narrow, asymmetric lineshape given that the assumption of slow exchange on the MR timescale (i.e. exchange rate $k <$ chemical shift of the labile protons) is met.

The primary method to quantify the CEST effect in vivo is the magnetization transfer asymmetry ratio (MTR_{Asym}), which is found using Equation 1.30, and assumes in a saturation transfer experiment, the only asymmetrical effect present over the Z-spectrum is the CEST effect downfield from water. However, the symmetry assumed by the MTR_{asym} has been shown to not be the case, as inherent asymmetries, such as MT (90) and the nuclear Overhauser effects (NOE) upfield from water (84) have been shown to significantly affect these measurements (43). While several methods have been developed to ignore these upfield effects (43,214), several studies have been recently published that have indicated the NOE effects may have clinical importance (213,215,216). Therefore, methods which can simultaneously model the MT and direct water saturation (DWS) effects are needed in order to appropriately detect effects both upfield and downfield of water.

Several researchers have developed methods to model more components of the CEST spectrum. Zaiss et al (42,45) developed a multi-Lorentzian model, which they used to simultaneously map the CEST effect, MT effect, and NOE effect at 7T. However, this method is restricted to high field strengths due to the need for the increased spectral resolution obtained at these higher field strengths, and thus, cannot be utilized at clinical fields (i.e. 3T). Desmond and Stanisz (40) also recently demonstrated that a CEST spectrum can be fit utilizing a full three-pool model of the Bloch-McConnell equations, however, fitting the full set of differential equations for each point in a data set would quickly become computationally intensive for a full brain volume.

Yarnykh and Yuan (82) recently showed that the two-pool Bloch-McConnell equations can be solved in the steady state in order to greatly decrease computational power. However, they made several approximations which prevent them from applying this model at offset frequencies smaller than 1 kHz away from water. In this work, I have removed these approximations, and now demonstrate that these improved steady state equations can be used to fit the CEST and MT effects simultaneously, providing new information about the entire CEST spectrum at clinical field strengths, as well as the typical values estimated from the two pool MT model. To this end, I i.) performed simulations demonstrating the superiority of this new two-pool qMT model over a simple Lorentzian difference method, and ii.) applied this model to in vivo data in the brain.

6.2. Theory

The steady state equations in their current form approximate a typical pulse sequence as a series of constant events, as shown in Figure 6.1. During each of these events, a constant process is occurring, which can be represented by the equations from Yarnykh (78) & Yarnykh and Yuan (82):

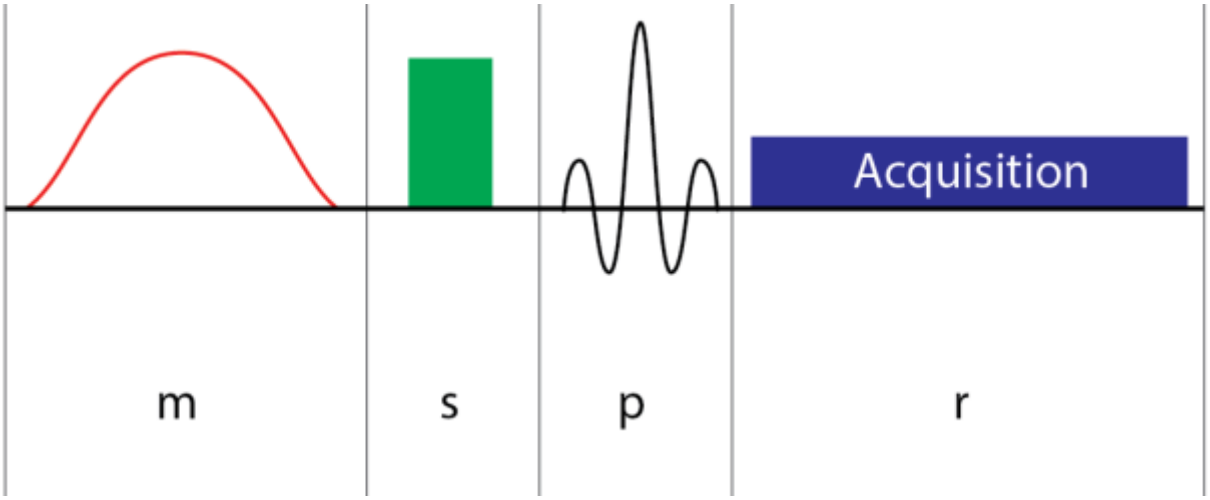

Figure 6.1. Visual representation of the different events within a typical MT SPGR pulse sequence. This sequence can be broken into four basic parts: the MT pulse (m), the prepulse spoiling (s), the excitation pulse (p), and the readout and delay before the next pulse (r).

$$\boldsymbol{M}_m = \exp\big((\boldsymbol{R}+\boldsymbol{W})t_m\big)\,\boldsymbol{M}_r + \big(\boldsymbol{I} - \exp\big((\boldsymbol{R}+\boldsymbol{W})t_m\big)\big)\boldsymbol{M}_{ss} \quad 6.1$$

$$\boldsymbol{M}_{s,r} = \exp\big(\boldsymbol{R}t_{s,r}\big)\,\boldsymbol{M}_{m,p} + \big(\boldsymbol{I} - \exp\big(\boldsymbol{R}t_{s,r}\big)\big)\boldsymbol{M}_{eq} \quad 6.2$$

$$\boldsymbol{M}_p = \boldsymbol{C}\boldsymbol{M}_s \quad 6.3$$

where **R** is the relaxation matrix (Equation 1.24), $\mathbf{M}_{ss}$ is the steady-state magnetization vector (Equation 1.23), **W** is the average saturation rate for each pool (free (f) and macromolecular (m)) (Equation 1.25), $\mathbf{M}_{eq}$ is the equilibrium magnetization vector:

$$\boldsymbol{M}_{eq} = \begin{bmatrix} 1 \\ PSR \end{bmatrix} \quad 6.4$$

and $\boldsymbol{C} = diag(\cos(\alpha), 1)$ is the instantaneous rotation of the magnetization in the free pool by an excitation pulse with a flip angle α. The pool size ratio (PSR) from Equation 6.4 is the ratio of

the macromolecular (m) to free (f) pools, and is correlated with white matter myelin density (13,125,126). Equations 6.1-6.4 can then be substituted into $\mathbf{M}_s$ (Equation 6.2)to solve for the magnetization in the free pool. These equations have been shown to well-approximate the two-pool Bloch-McConnell equations when using a variety of MT pulse saturations. However, these equations are valid only with two fundamental approximations: 1) the pulse is ideally spoiled, and 2) that the saturation pulse in phase m of the pulse sequence shown in Figure 6.1 can be substituted for its mean-square value (i.e. an amplitude of an effective rectangular pulse with the same duration producing the same average power) (78,82). While the first approximation is generally assumed to be correct for most SPGR sequences, the approximation of the RF pulse removes the amplitude modulation required to accurately model the effect of the water pool on the magnetization. While approximating the RF pulse is generally inconsequential for MT applications, where the offset frequency of the MT pulse is greater than 1 kHz, this approximation becomes problematic when applying the steady state model to data with a significant water contribution. Therefore, in order to more accurately model the MT pulse, we can instead model the MT phase (m in Figure 6.1) of the pulse sequence as a series of n smaller time points that will more accurately describe the shape of the MT pulse; breaking the MT pulse into many smaller pieces that can be approximated at a constant RF power over a small interval in time, Δt, without losing the overall shape of the RF pulse. The expansion of $\boldsymbol{M}_m$ will result in the following set of equations:

$$\boldsymbol{M}_{m,1} = \exp\big((\boldsymbol{R} + \boldsymbol{W}_1)\Delta t\big)\,\boldsymbol{M}_r + \big(\boldsymbol{I} - \exp\big((\boldsymbol{R} + \boldsymbol{W}_1)\Delta t\big)\big)\boldsymbol{M}_{eq} \qquad 6.5a$$

$$\boldsymbol{M}_{m,2} = \exp\big((\boldsymbol{R} + \boldsymbol{W}_2)\Delta t\big)\,\boldsymbol{M}_{m,1} + \big(\boldsymbol{I} - \exp\big((\boldsymbol{R} + \boldsymbol{W}_2)\Delta t\big)\big)\boldsymbol{M}_{ss,1} \qquad 6.5b$$

$$\vdots$$

$$\boldsymbol{M}_{m,n} = \exp\big((\boldsymbol{R} + \boldsymbol{W}_n)\Delta t\big)\,\boldsymbol{M}_{m,n-1} + \big(\boldsymbol{I} - \exp\big((\boldsymbol{R} + \boldsymbol{W}_n)\Delta t\big)\big)\boldsymbol{M}_{ss,n-1} \qquad 6.5c$$

Including these equations in the equation for $\mathbf{M}_s$ will result in the following equation:

$$M_z = \left\{ \boldsymbol{I} - \boldsymbol{E}_s \prod_{i=1}^{n} \boldsymbol{E}_{m,i}\, \boldsymbol{E}_r \boldsymbol{C} \right\}^{-1} *$$

$$* \left\{ \left[\boldsymbol{E}_s \left(\prod_{i=1}^{n} \boldsymbol{E}_{m,i} \left(\boldsymbol{I} - \boldsymbol{E}_r \right) + \prod_{i=2}^{n} \boldsymbol{E}_{m,i} \left(\boldsymbol{I} - \boldsymbol{E}_{m,1} \right) \right) + \left(\boldsymbol{I} - \boldsymbol{E}_s \right) \right] \boldsymbol{M}_{eq} \right. \qquad 6.6$$

$$\left. + \boldsymbol{E}_s \left[\sum_{i=2}^{n-1} \prod_{j=i+1}^{n} \boldsymbol{E}_{m,j} \left(\boldsymbol{I} - \boldsymbol{E}_{m,i} \right) \boldsymbol{M}_{ss,i-1} + \left(\boldsymbol{I} - \boldsymbol{E}_{m,n} \right) \boldsymbol{M}_{ss,n-1} \right] \right\}$$

where $\boldsymbol{E_{m,i}} = \exp\left((\boldsymbol{R} + \boldsymbol{W_i}) \Delta t \right)$ describes off-resonance saturation at each pulse interval, i, $\boldsymbol{E_r} = \exp(\boldsymbol{R} t_r)$ describes the relaxation during the acquisition/repetition delay, and $\boldsymbol{E_s} = \exp(\boldsymbol{R} t_s)$ describes the relaxation during the spoiling delay after the MT pulse. The term $\mathbf{W}_i$ is described by:

$$W^{f,m} = \pi \omega_{1,i}^2 g^{f,m} \left(\Delta\omega, T_2^{f,m} \right) \qquad 6.7$$

where $\omega_{1,i}$ is the interpolated of the B_1 amplitude at the time point, $t_{m,i}$, of the MT pulse. Modeling **W** for each small time point $t_{m,i}$ removes the approximation from the MT pulse, and therefore Equation 6.6 can be extended below 1 kHz. If the number of MT pulses is reduced to a single pulse, Equation 6.6 will be reduced to:

$$M_z = \{ \boldsymbol{I} - \boldsymbol{E}_s \boldsymbol{E}_m \boldsymbol{E}_r \boldsymbol{C} \}^{-1} * \left\{ [\boldsymbol{E}_s \boldsymbol{E}_m (\boldsymbol{I} - \boldsymbol{E}_r) + (\boldsymbol{I} - \boldsymbol{E}_s)] \boldsymbol{M}_{eq} + \boldsymbol{E}_s (\boldsymbol{I} - \boldsymbol{E}_m) \boldsymbol{M}_{ss} \right\} \qquad 6.8$$

Which is the same equation as that proposed by Yarnykh and Yuan (82)

Fitting Equation 6.6 to MT and CEST data simultaneously will generate a set of qMT parameters – the PSR, macromolecular (m) to water (f) pool exchange rate (k_{mf}), and the relaxation rates in each pool, T_{2f} and T_{2m} – which can then be used to model the MT effect in the CEST regime. The measured signal intensity in Equation 6.6 is proportional to the longitudinal magnetization of the free pool before an excitation pulse, M_z^f:

$$S_{MT} = M_z^f \exp\left(-\frac{TE}{T_2^*} \right) \sin(\alpha) \qquad 6.9$$

However, these multiplicative factors can be excluded by normalizing the signal to a reference measurement M_0, typically taken at an offset of 100 kHz to minimize MT effects,

$$m_z = \frac{S_{MT}}{S_{ref}} = \frac{M_z^f(\Delta\omega)}{M_z^f(\Delta\omega = 100\ kHz)} \qquad 6.10$$

and the resulting signal can be directly fit to the model described in Equation 6.6, normalized by the same reference measurement at $M_z^f\,(\Delta\omega = 100\ kHz)$. This new model is referred to as the qMT model or qMT fit in subsequent sections.

6.3. Materials and Methods

All numerical simulations and data analyses were performed with scripts written in MATLAB 2016a (MathWorks, Natick, Massachusetts), unless otherwise noted. Additionally, because the most often reported CEST effect in vivo is amide proton transfer (APT) CEST, which is sensitive to amide protons associated with proteins and peptides resonating 3.5 ppm downfield from water, the APT CEST effect was the target of all simulations and imaging protocols. Furthermore, since a CEST effect will bias the CEST z-spectrum away from a spectrum composed entirely of MT and water, the area from 3 to 4 ppm was ignored in all fits. The area between -1 to 1 ppm was also ignored in the fitting due to minor differences seen between the generated Bloch equation data and the qMT fitting parameters at the water resonance.

6.3.1. Simulations

A three pool model consisting of a bulk water pool (f), an MT pool (m), and a solute pool (s) was created by combining Equations 1.17 and 1.31, and was used to generate steady state signal data for healthy white matter (WM), healthy grey matter (GM), and an MS lesion. The tissue parameters for the water pool used for the simulations are listed in Table 6.1. The tissue parameters for the MT pool and solute pools were defined as: k_{mf} – 10 1/s, the exchange rate from the solute pool to the water pool, k_{sf} = 40 1/s, a solute concentration relative to water of 0.1%, $R_{1m} = R_{1f}$ for each tissue type, R_{1s} = 1 1/s, T_{2m} = 10 µs, and T_{2s} = 160 ms.

Table 6.1 Tissue parameters used for the Simulations. Values were chosen from typical values in each respective tissue.

	White Matter	Grey Matter	MS Lesion
PSR	0.20	0.13	0.08
R_{1f} (1/s)	0.77	0.69	0.51
T_{2f} (ms)	70	100	120

Three-pool data was generated for two different experiments: an MT experiment in order to appropriately estimate the MT parameters, and a CEST experiment to fit the CEST and water pool data. The MT experiment included two saturation powers at nominal flip angles (α_{MT}) of 360˚ and 820˚ applied over 20 ms, with frequency offsets of 1, 1.5, 2, 2.5, 4, 64, and 100 kHz. The CEST experiment was performed over a single saturation power in all cases, with a saturation length of 150 ms, with 31 frequency offsets evenly spaced between -5 and 5 ppm, with a reference measurement at 100 kHz. Other relevant simulation parameters for the specific cases are listed below.

Simulation 1

The first set of simulations demonstrate the impact of modeling the a two-pool MT model, instead of approximating the curve from a Lorentzian fit. To this end, signal data was generated using the parameters above with two maximum B_1 saturation powers (2 and 3 μT) for all tissue types listed in Table 6.1. The resulting data was then fit using Equation 6.6 to estimate a set of qMT parameters that fit both the MT and CEST data, and a z-spectrum over ±5 ppm was generated. Next, the Lorentizan function from Jones, et al. (43) was fit to the same data and a z-spectrum of this data was generated as well. Last, signal data from a two-pool model (water+MT) was generated in order to illustrate what z-spectrum the qMT fit should be generating. The resulting z-spectra for all fits were plotted for each B_1 power and tissue type.

Simulation 2

The second simulation demonstrates how both the Lorentzian and qMT fits behave under non-ideal conditions. To determine this, Monte Carlo simulations were performed by first adding Gaussian noise (SNR = 60 at thermal equilibrium) to the generated data, and the qMT and Lorentzian fits were performed over 100 noise realizations for each tissue type. The maximum B_1 saturation power was fixed at 2 μT in order to simulate a similar effect to what was prescribed in vivo (see Section 6.3.2 below). The area under the curve (AUC) was taken by finding the integral of the residuals (difference between the CEST data and the generated fits) from 3 to 4 ppm for the Lorentzian and qMT fits. The ideal signal data for a two-pool model with no CEST effect was also generated, similar to what was done in Simulation 1. The AUC for this generated data was also calculated to represent the ideal AUC. A two-sample t-test was then used to

determine if the Lorentzian and qMT fits were significantly different from the ideal AUC for a threshold of $p < 0.05$.

6.3.2. In Vivo Imaging

The local Institutional Review Board approved this study, and signed informed consent was obtained prior to examination. A single volunteer (female, age 22 years old) was imaged in a 3T Philips Achieva scanner (Philips Healthcare, Best, the Netherlands). A two-channel, multi-transmit body coil was used for excitation, and a 32-channel head coil was used for signal reception. Two experiments were performed: a qMT acquisition, which consisted of acquiring MT-weighted images, T_1-weighted images, and B_1 and B_0 maps to correct for field inhomogeneities, and a CEST acquisition, which consisted of acquiring CEST-weighted images and a water saturation shift referencing (WASSR) image (217) to correct B_0 inhomogeneities in the CEST spectrum. All acquisitions used a FOV of 220 x 220 x 20 mm^3 over four slices, used a SENSE (RL) factor of 2 where appropriate, and were acquired at a resolution of 1 x 1 x 5 mm^3, unless otherwise specified. Additionally, all images were reconstructed to the same in-plane matrix size of 256 x 256.

The MT protocol was acquired at 8 offsets ($\Delta\omega$) and 2 RF powers (α_{MT}) over 2 signal averages, and an echo planar imaging (EPI) factor of 5 and TR/TE/α_{EX}=50 ms/7.4 ms/10˚. MT weighting was achieved using a 20-ms, single-lobed sinc pulse with Gaussian apodization, α_{MT}= 360˚ and 900˚, and offset frequencies ($\Delta\omega$) = 1, 1.5, 2, 2.5, 8, 16, 32, 100 kHz (chosen to approximately logarithmically sample the expected MT z-spectra). To correct for B_1 and B_0 inhomogeneities across the volume, B_1 and B_0 maps were acquired using fast 3D techniques — B_0: dual-TE GRE with $TR/TE_1/TE_2$ = 50/3.4/5.7 ms and α = 25˚ at a resolution of 2 x 2 x 5 mm^3; B_1: dual-TR actual flip angle (AFI) GRE method (142) with $TR_1/TR_2/TE$ = 30/130/1.88 ms and α = 60˚ at a resolution of 2 x 2 x 5 mm^3. T_1 mapping was performed using a double angle acquisition, as described in Smith, et al. (58), with TR/TE =100/10 ms and α = 15˚ and 60˚. Acquisition times were 3 minutes for the MT weighted images, 30 seconds for the B_0 map, 50 seconds for the B_1 map, and 2 minutes for the T_1 map.

The CEST protocol was acquired over 36 offsets, applied asymmetrically between ±5 ppm with a TR/TE/α_{EX}=302 ms/8.6 ms/15˚. CEST saturation was achieved with a shaped 2 μT pulse

(a single 150 ms RF sinc-Gauss pulse). An additional image at an offset of 100,000 ppm was acquired for a reference, yielding a total of 37 individual images. Additional parameters for the CEST acquisition were an EPI factor of 7, and 1 signal average. The WASSR images used the same parameters as the CEST acquisition, except: The saturation pulse was a 0.5 μT pulse, and this protocol was acquired over 21 offsets between ±1 ppm, with an additional reference image acquired at 100,000 ppm. Acquisition times were 14 minutes, 22 seconds for the CEST protocol, and 8 minutes, 42 seconds for the WASSR protocol, resulting in an overall scan time of approximately 30 minutes.

6.3.3. Image Analysis

Before fitting, all in vivo images were co-registered using tools from FSL v5.0.2.1 (FMRIB, Oxford, UK) (145,146). First, all images were brain-extracted using the brain extraction tool (BET) (143,144), then all of the subject-level data was co-registered to the S_0 image from the MT imaging data using FLIRT (145,146). All image data was then imported into MATLAB for further processing.

An R_{1obs} ($1/T_{1obs}$) map was independently reconstructed by using the double angle formula originally proposed by Smith, et al. (58), which calculates a T_1 value for each voxel after correcting for B_1 inhomogeneities. To correct for B_0 inhomogeneities in the CEST spectrum, the mean absolute frequency shift was calculated from the WASSR scan and the CEST z-spectrum was shifted accordingly.

Finally, the normalized to S_0 MT and CEST data was used to generate qMT parameter maps for each voxel. This model contains six independent parameters to accurately fit the two pool signal model: R_{1m}, R_{1f}, T_{2m}, T_{2f}, PSR = M_{0m}/M_{0f}, and $k_{mf} = k_{fm}/PSR$. R_{1f} was set equal to the R_{1obs}, and as the signal dependence on R_{1m} is weak (19), this was set to R_{1obs} as well (37). The remaining parameters were estimated for each voxel using Equation 6.6. Additionally, the B_0 map was used to correct field inhomogeneities in the MT portion of the qMT fit, and the B_1 map was used to correct B_1 inhomogeneities in both the CEST and MT portions of the qMT fit.

To estimate the CEST effect in vivo, the estimated parameter maps from the qMT fit were then used to generate signal data from 3 to 4 ppm. The APT CEST effect was calculated using an

AUC analysis from 3 to 4 ppm, as performed in the simulations above. To compare against a "gold standard" calculation, the data was also fit to the Jones Lorentzian function (43).

Mean parameter values for each fitting methodology, and for all qMT parameters, were calculated from regions of interest (ROI) in the GM and WM, as shown in Figure 6.4a. ROIs were placed manually using MIPAV (NIH, Bethesda, MD). The mean values for each tissue type and fitting methodology were then compared.

6.4. Results

6.4.1. Simulations

Z-spectra from simulation 1 are displayed in Figure 6.2 for (a., d.) white matter, (b., e.) grey matter, and (c., f.) lesion data. The qMT fit data approximates the ideal two pool signal data very well, with the exception of around the water resonance. However, comparing the qMT fit with the Lorentzian fit illustrates a striking difference: the Lorentzian data underfits the signal data in every example (a-f) at the target of 3-4 ppm. This is particularly apparent in Figure 6.2a, where the Lorentzian model cuts directly through the CEST effect.

This effect is more clearly seen in Figure 6.3, where the results of the Monte Carlo analysis are shown. The Lorentzian fit (AUC: WM = 1.1±1.0%, GM = 2.0±1.0%, Lesion = 2.9±1.0%) was found to have a much lower AUC than the qMT fit (AUC: WM = 2.5±1.3%, GM = 3.2±1.1%, Lesion = 4.1±1.0%), and the ideal fit (AUC: WM = 2.7±1.3%, GM = 3.5±1.6%, Lesion = 4.3±1.6%). The Lorentzian difference was also found to be significantly different than both the qMT fit and the ideal fit ($p < 0.0001$), for all simulated tissue types, indicating that the Lorentzian method is not describing a true fit of the model data.

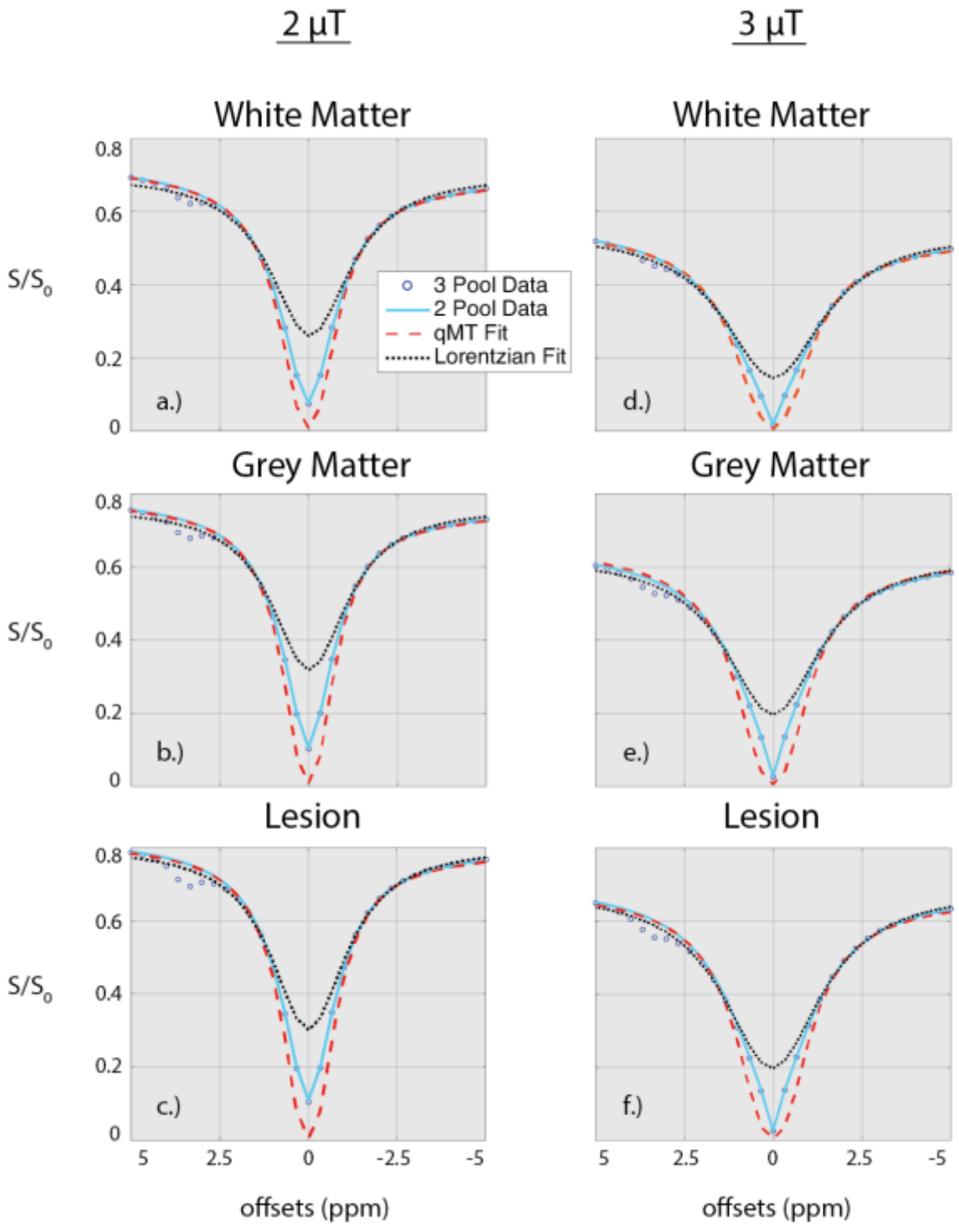

Figure 6.2. Simulations of the Z-spectra for the three pool CEST signal data (blue circles), ideal two pool signal data (light blue line), qMT fit (red dash), Lorentzian fit (black dots) for 2 µT (a-c), and 3 µT (d-f) for healthy white matter, grey matter, and lesion tissue parameters. Notice that the Lorentzian fit underestimates the CEST effect in all cases, while the qMT fit more closely approximates the ideal two pool signal data.

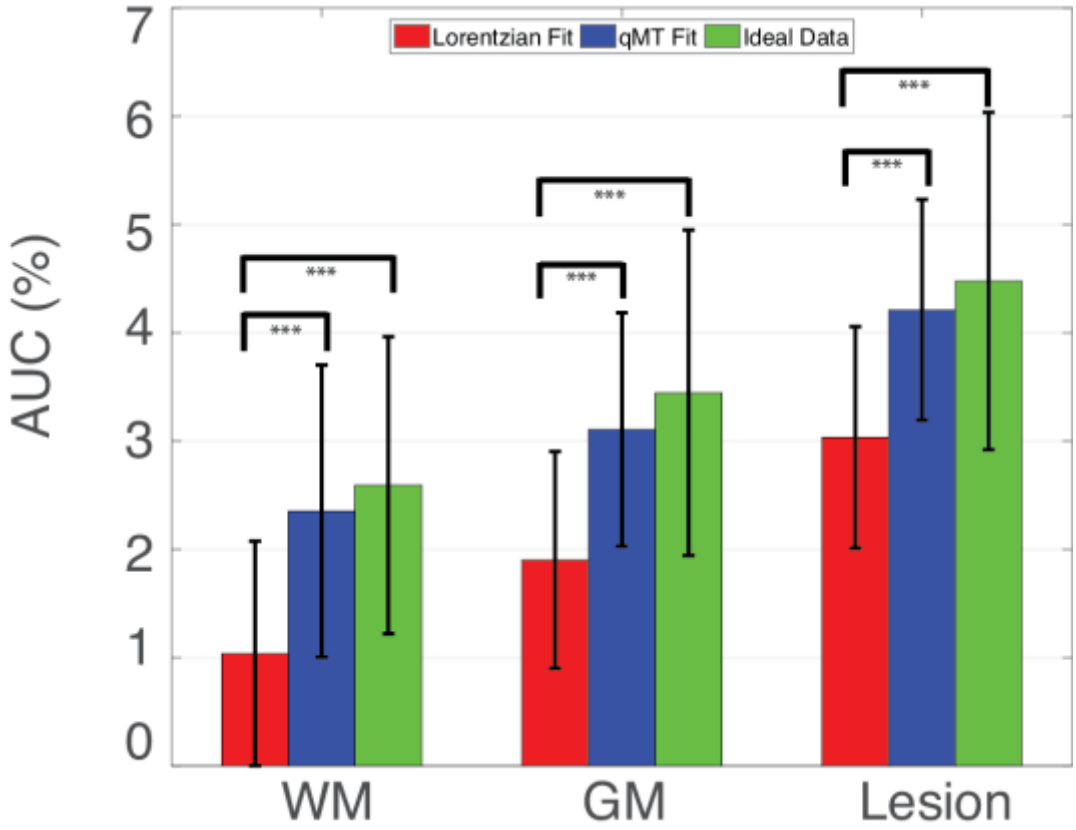

Figure 6.3. Results from the Monte Carlo analysis. The Lorentzian fit was found to be significantly different (***, $p<0.0001$) from the qMT and ideal data fits.

6.4.2. In vivo data

Anatomical and qMT parameter maps are displayed in Figure 6.4, with the mean values from the ROIs for WM and GM listed in Table 6.2. The PSR (WM = 23.3±3.3%, GM = 11.8±1.7%) clearly delineate the different tissues within the brain, while the k_{mf} (WM = 12.3±3.9 1/s GM = 9.1±3.0and T_{2m} (WM = 9.9±0.3 µs, GM = 9.9±0.1 µs) are largely unaffected by tissue type (i.e. white matter and grey matter). Interestingly, the T_{2f} (WM = 50.0±3.1 ms, GM = 66.1±5.6 ms) displays higher values than has been reported previously (36,37), however, these increased values do not seem to be due to a misfit of the data. Instead, this may be indicative of a more realistic fit of the T_{2f} parameter, as these values are within 20 ms of what has been reported previously for T_2 (frontal WM = 69±2 ms, frontal GM = 88±3 ms) values in the brain previously at 3T (218).

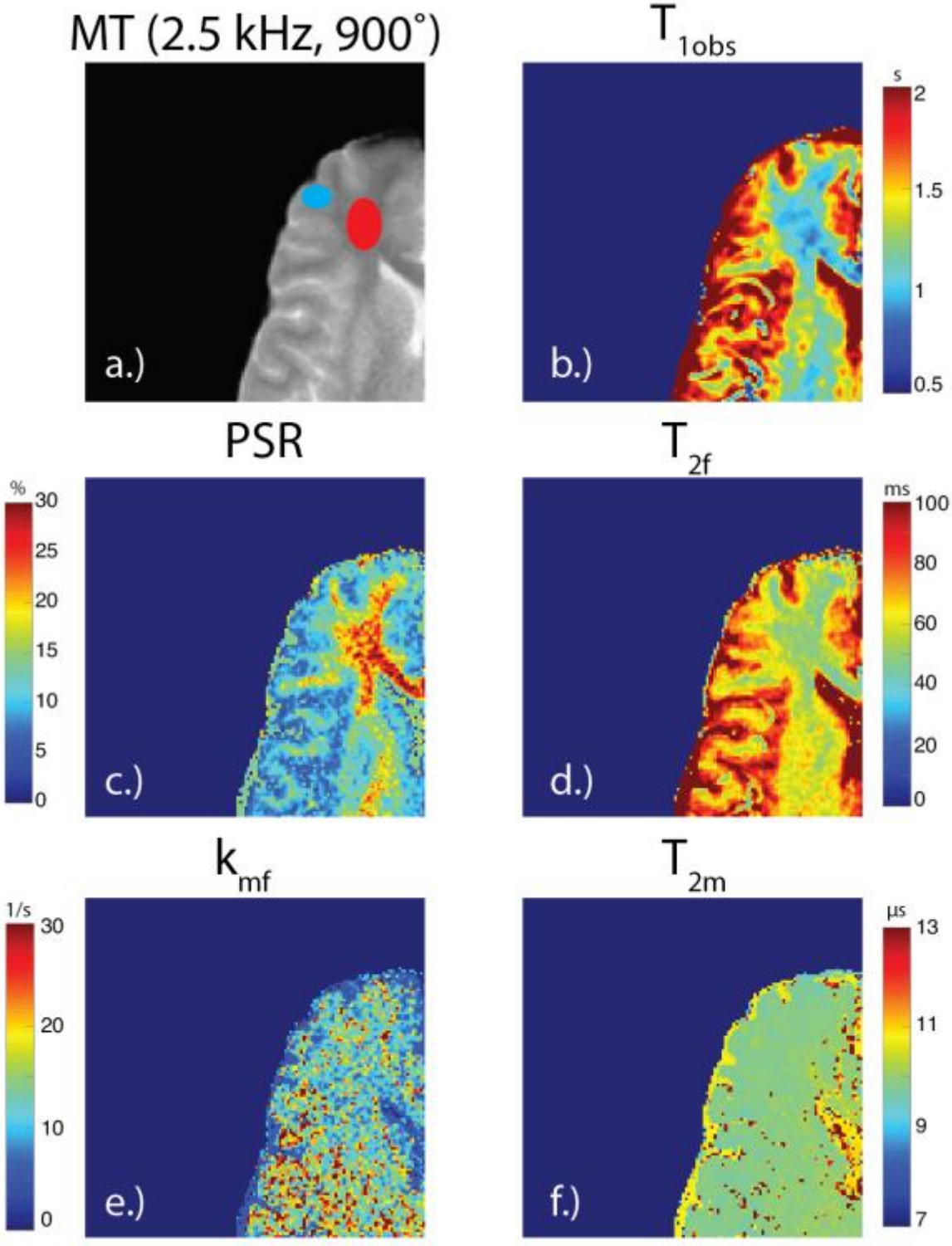

Figure 6.4. a.) Anatomical image illustrating the area of the brain under analysis, with the ROIs for the GM (blue) and WM (red) displayed as well. The T_{1obs} map for the brain is shown in b.), with the corresponding estimates from the qMT fit shown in (c.-f.), corresponding to the PSR, T_{2f}, k_{mf}, and T_{2m}, respectively.

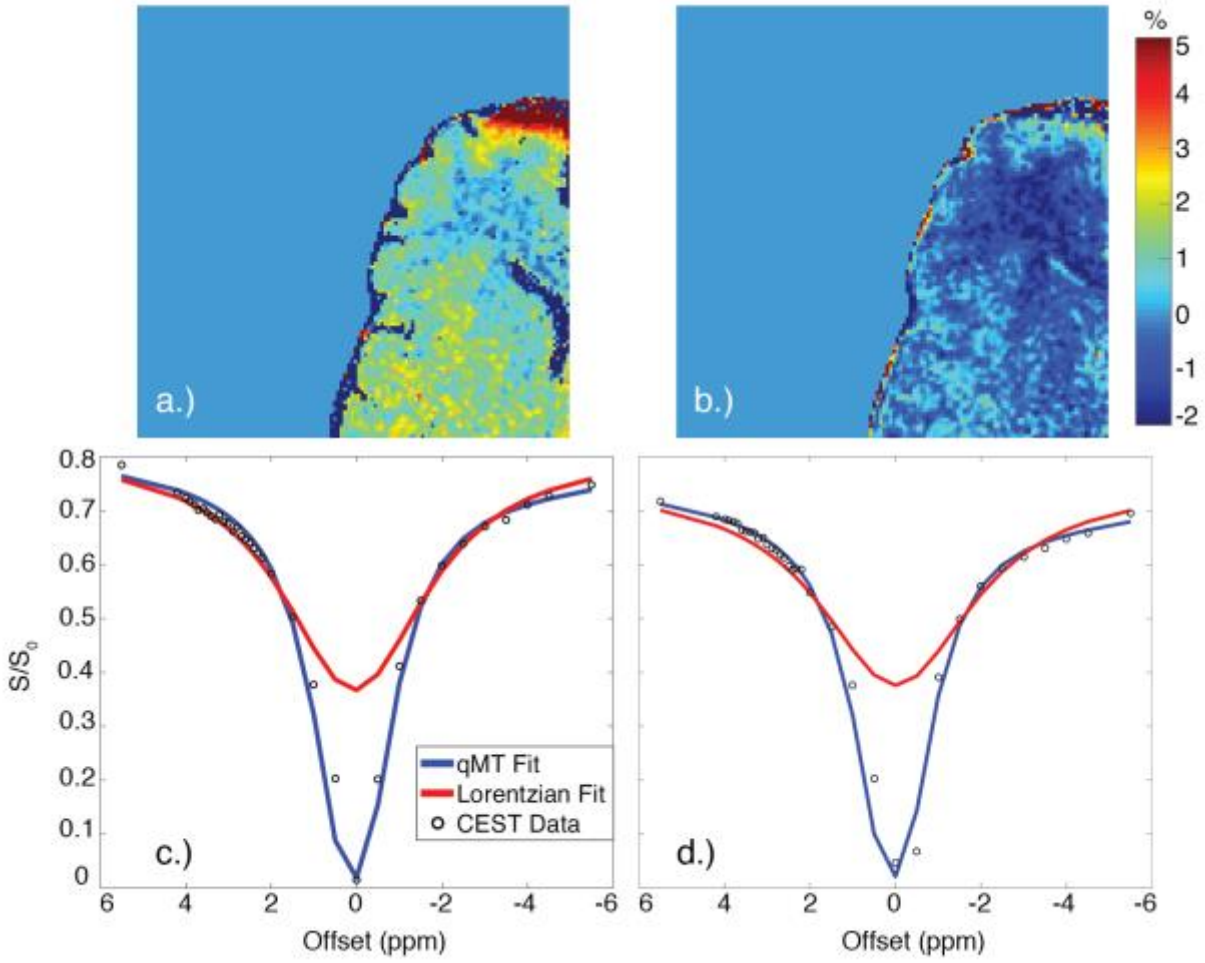

Figure 6.5. AUC maps for the (a.) qMT fit and (b.) Lorentzian fit, with corresponding CEST spectra in the (c.) grey matter and (d.) white matter. Notice that the Lorentzian fit severely underestimates the positive side of the spectrum, particularly in the presence of significant MT effects, as is typical in white matter.

AUC maps for the qMT and Lorentzian fits are shown in Figure 6.5a and b, respectively, with representative CEST z-spectra from a point in the grey matter and white matter displayed in Figure 6.5c and d, respectively. Additionally, mean values for the AUC using the qMT fit and the Lorentzian fit are listed in Table 6.2. A majority of the fits in the Lorentzian model were found to be below 0, indicating that the Lorentzian fit was underfitting the spectrum from 3-4 ppm (WM: -1.5±0.4%, GM: -0.6±0.3%). This is confirmed in the z-spectra in Figure 6.5c and d: the Lorentzian fit was biased toward the negative side of the spectrum. However, this trend is not present in

the qMT fitting model, which fits both sides of the CEST spectrum adequately, and thus, provides positive AUC values (WM: 0.3±0.05%, GM: 1.1±0.2%).

Table 6.2 Mean (±SD) values for ROIs drawn in the white matter and grey matter of the brain. qMT parameter values are derived from the two pool fit, while the AUC for each fitting methodology was found by finding the integral from 3 to 4 ppm.

	White Matter	Grey Matter
PSR (%)	23.3±3.3	11.8±1.7
k_{mf} (1/s)	12.3±3.9	9.1±3.0
T_1 (s)	1.1±0.1	1.7±0.2
T_{2f} (ms)	50.0±3.1	66.1±5.6
T_{2m} (μs)	9.9±0.3	9.9±0.1
qMT AUC (%)	0.3±0.05	1.1±0.2
Lorentzian AUC (%)	-1.5±0.4	-0.6±0.3

6.5. Discussion

The purpose of this study was to derive a more accurate steady state model of the two-pool Bloch equations that could be utilized in CEST imaging. I compared simulations of the Lorentzian fit originally described by (43) with the new qMT fit presented here, and found that the qMT fit more accurately describes a standard two pool model over the range of values typical for a CEST spectrum. This new model will improve our sensitivity to deviations in the CEST spectrum due to CEST (upfield from water) and NOE (downfield from water) moieties, and thus may help better characterize the underlying chemical environment within tissues.

The Lorentzian method has only been shown to be valid when the presence of MT effects is not significant. In their paper presenting the Lorentzian fit, (43) applied a short, low power (1 μT) saturation pulse in order to minimize the MT effect in the z-spectrum. While the Lorentzian fit can be used with low power CEST acquisitions to generate accurate measures of the AUC, utilizing the Lorentzian fitting strategy at higher saturation powers will yield results similar to what is seen in this paper (Figure 6.2). This poor fit will in turn underestimate the CEST effect,

and lead to reduced sensitivity to changes in the moiety of interest. By incorporating the MT effect into the two-pool model I have effectively increased our sensitivity to CEST effects because I have removed some of the influence of MT signal from the fitting model. Therefore, deviations from the expected signal should be primarily influenced by CEST effects. The in vivo estimates of the CEST effect further confirm this conclusion. Because asymmetry exists in the CEST spectrum due to the MT effect, a Lorentzian function will not be able to adequately capture both sides of the curve. Therefore, the fitting function for the Lorentzian will either overestimate the downfield side of the z-spectrum, or underestimate the upfield side of the z-spectrum; the latter was seen in this analysis, which provided negative AUC values for the APT effect. However, the qMT fit was able to adequately capture both sides of the z-spectrum, and thus, was able to properly fit the CEST data.

In addition to downfield CEST effects, this new qMT model can also be used to estimate NOE effects on the upfield side of the curve when in the presence of significant MT signal. Because deviations from the qMT model should indicate areas where there are effects not related to water or MT, finding a significant deviation on the upfield side of the z-spectrum should indicate the presence of NOE effects. This may be particularly useful at higher field strengths, where several studies have shown the presence of NOE signal in both healthy controls and patient populations (42,216), as well as in animal models (215,219) of disease. Furthermore, as the MT and CEST protocols are acquired separately, this new qMT model should be able to be combined with any qMT imaging method to accurately map the MT effect in the CEST spectrum. Therefore, by utilizing alternative methods, such as selective inversion recovery (59,220), the qMT fitting model may be applied to any set of data that contains both MT and CEST components.

Employing a fit closer to the water resonance has also improved the estimates of the T_{2f} parameter in the pulsed saturation qMT model. The original experiments performed by Sled and Pike (36) found that the T_{2f} was approximately 30% lower in the model fits than was found in multi-echo T_2 experiments. Indeed, a similar trend has been seen in experiments since then, with Yarnykh's experiments in the brain (37,78,82), and my own experiments in the spinal cord (76), the T_{2f} was found to be around 20-30 ms. Sled and Pike postulated that this decrease in the T_2 was due to improperly modeling the number of pools necessary to accurately depict the multiple

free water components present in vivo (221,222). However, the original steady state equations may not have been able to adequately model the water component because the RF approximation restricted the two-pool model to offsets above 1 kHz, thereby underestimating the T_{2f} parameter. Indeed, the experiments performed here reported much higher (approximately double) T_{2f} values compared to those found in Yarnykh (37), which are more in line with what has been reported for quantitative T_2 values in the brain (218).

While the qMT model has shown that it can more accurately fit the CEST curve than traditional Lorentzian methods when in the presence of significant MT effects, there are several limitations. As can be seen from Figure 6.2, this model does not fit the area directly surrounding the water resonance well. This deviation in the model may be due to the approximation that is made with the water lineshape. Water has been shown to be well-approximated by a Lorentzian lineshape, however, this may not be adequate to resolve the actual lineshape of water near 0 ppm. Therefore, it may be necessary to develop a set of steady state equations that directly model the transverse effects of the water components to completely model this signal at 0 ppm, or develop a lineshape that more accurately captures the water lineshape near 0 ppm.

Importantly, while the qMT portion of the acquisition presented here adds additional scan time, it is not significant if the benefits of this acquisition are considered. The entire qMT acquisition takes only 6.5 minutes longer for the volume scanned here, and fast acquisition strategies can be pursued to decrease the scan time further. However, the added value provided by acquiring the qMT data may reduce the detrimental aspects of acquiring more data. Indeed, the qMT data, and in particular, the PSR, has been shown to be well-correlated with myelin content (25,28,179), and thus, CEST studies that seek to characterize white matter may benefit from the additional information provided by the qMT data.

Additionally, while this model accounts for the MT portion of the CEST curve, it has not completely isolated the CEST effect. As can be seen in Figure 6.2, the CEST effect is still slightly dependent on the MT effect (seen in the changes between tissue types) and B_1, therefore, there are still areas of this method that can be improved. Desmond and Stanisz (40) demonstrated that a three pool model (CEST, MT, water) can be used to quantitatively estimate the CEST effect in vitro using the full Bloch equations. While the Bloch equations take a significantly long period

to properly fit a CEST spectrum, solving for a three-pool steady state model using the same approach applied in this paper and in Yarnykh (78) could quantify the CEST effect efficiently, isolating it from the B_1 and MT effects that may affect an accurate characterization of the CEST effect.

One of the main drawbacks of the qMT model is that it takes a much longer time to fit all of the parameters than a simple Lorentzian model would take. This is most likely due to the large number of points, and the need to completely characterize the RF pulse shape for each offset and power in both the CEST and MT parts of the spectrum. However, several optimizations can be made to improve the efficiency of the qMT fitting model. The original derivation of the steady state signal equations by Sled and Pike (35) found that modeling the bandwidth of the saturation pulse was negligible in their initial experiments. This was also observed in the experiments here when modeling the MT (i.e. > 1kHz) part of the spectrum, thus, this model may become more efficient by approximating the RF pulse in the MT part of the spectrum. Additionally, this model used 100 individual points to accurately capture the RF bandwidth, however, the number of points may be able to be reduced without detrimentally affecting the model. Lastly, the number of individual offsets can potentially be reduced through interpolation or efficient sampling of the Z-spectrum in order to reduce the amount of data needed to fit the model.

6.6. Conclusion

This study demonstrates that the MT effect can be effectively modeled in a CEST Z-spectrum. The model described here provides a more accurate measure of the CEST effect than is provided by a conventional Lorentzian fit, and also improves the accuracy in estimates of T_{2f}. Future work includes deriving a three-pool model in order to quantify CEST effects, comparing the measures obtained from the qMT fit against quantitative T_2 data, as well as improving the goodness of fit of this model around the water resonance.

Chapter 7: General Discussion and Conclusions

The overall goal of this dissertation was to further the understanding of quantitative magnetization transfer (qMT) imaging at clinical MRI field strengths. Since qMT imaging has been shown to be sensitive to myelin pathology, the first goal of this thesis was to expand these metrics to areas outside of the brain, into the optic nerve and spinal cord (SC), where radiological changes may be better correlated with clinical disability. Next, I expanded a new MT imaging method, inhomogeneous magnetization transfer (ihMT), that has been shown to be specific to WM, and thus, may provide a better indicator of changes in myelin than traditional MT imaging. Finally, I developed a steady state model of the two-pool Bloch equations that would fit both the MT and water pools in CEST to more appropriately isolate the CEST effect.

MT imaging has been shown to be remarkably sensitive to changes in myelin content (13,159,168), with the macromolecular to free pool size ratio (PSR) correlating well with myelin content in the brain (13,125-127). However, there has been a clinical need to move these quantitative MT techniques to areas of the central nervous system (CNS) outside of the brain. The SC and optic nerve in particular have been shown to exhibit symptoms in multiple sclerosis (MS) that may correlate strongly with other clinical deficits (108,110). Therefore, the first goal of this dissertation was to explore the sensitivity of qMT to anatomies outside of the brain. First, the full two-pool model was applied in the optic nerve. This required a modification to the standard MT acquisition due to the unique anatomy of the optic nerve: the optic nerve is surrounded by fatty connective tissue, necessitating fat suppression techniques to accurately visualize the nerve. Therefore, I demonstrated that the Dixon fat-water separation method can be used to suppress the fat signal in MT-weighted images, which allowed me to quantify the macromolecular signal in the optic nerve. The PSR proved robust to the potential changes in signal due to the Dixon fat-water separation method, while not utilizing the Dixon method in the presence of fat proved to significantly confound the two-pool qMT model and deliver inaccurate estimates of the PSR.

Next, a new qMT method was applied in the SC in order to rapidly acquire estimates of the underlying macromolecular structure of the SC. While the SC macromolecular structure has been quantified in the past (15), the small size of the SC has necessitated high resolution imaging

in order to accurately visualize the composition within the SC. However, the conventional qMT acquisition strategy would require a significantly long scan time in order to accurately estimate quantitative parameters in the SC. Therefore, I applied the single point qMT model, as formalized by Yarnykh (37), to the SC, and derived a set of constraints that could be used to increase the resolution in the qMT acquisition without significantly sacrificing scan time. The estimates of the PSR from the single point method were robust over time, and were shown to be similar to their counterparts from the conventional qMT model.

When this qMT method was applied in a patient cohort, statistical comparisons of the constrained parameters from the full qMT between the healthy and patient groups demonstrated a trend towards a significant p-value. Therefore, contrary to what Yarnykh, et al. (180) demonstrated in the brain, it is necessary to derive constrained parameters to use in the single point model in the pathology of interest. When appropriately constraining the model for the SC in the patient cohort, the high-resolution PSR maps provided several important differences from the healthy control group. First, they demonstrated a significant specificity to lesions with respect to both the white matter (WM) in the control group and the normal appearing white matter (NAWM) in the patient group. Second, histograms of the NAWM versus the healthy control WM illustrated a large difference between the two groups. Specifically, the NAWM contained a significant amount of low PSR values, which may indicate that the PSR is sensitive to changes that may be occurring in the pathological tissues before they are appear in conventional imaging metrics. The increased sensitivity to the subtle changes in the patient cohort offered by the high-resolution PSR maps may provide a more accurate method to diagnose and treat disease, such as MS, in the SC.

The single point qMT method was also applied in the thoracolumbar SC to demonstrate that these constraints can be derived along the entire SC in order to facilitate high-resolution imaging. Although the power of the sample size prevented statistical comparisons, the PSR in grey matter (GM) and WM was shown to be similar to what was found in the cervical SC. Applying the single point method in the thoracolumbar cord will provide an opportunity to both quantitatively characterize this area of the cord in healthy tissue, and determine how the thoracolumbar region of the SC is affected by neurodegenerative pathologies, such as MS.

While the sensitivity of qMT has been well-established, the specificity of MT to myelin content has not been definitively demonstrated. However, there have been recent strides to improve upon this by utilizing a new type of MT contrast called ihMT (112,113). ihMT has been shown to be remarkably specific to myelin content in the brain and SC, however, under its current implementation, it cannot collect data in a large, 3D volume, and thus cannot be effectively employed to investigate pathology. The work in this dissertation demonstrated that by using a pulsed acquisition strategy, we can acquire a full volume of ihMT data in the same scan time that a single slice would need under the original acquisition methodology. Importantly, the change in acquisition method (from a pulse train to a pulsed acquisition) did not significantly affect the ihMT scan, indicating that the pulsed acquisition strategy fundamentally improves the ihMT technique. This research lays the groundwork for application of this technique in a patient model, such as MS, where the increased specificity offered by ihMT may improve early detection of disease, and may offer a more accurate measure of tracking treatment course.

The last major part of this dissertation involved utilizing the Bloch equations to improve our understanding of the confounding effects in the CEST spectrum. MT effects dominate the entire CEST spectrum, corrupting most conventional measures of the CEST effect. However, this dissertation has demonstrated that these confounding effects in the CEST spectrum can be minimized by utilizing the Bloch equations to account for both MT and DWS effects. Accurate detection of low concentration metabolites with CEST may provide additional information about the underlying chemical and neurological processes involved in MS and other neurodegenerative disorders.

The effect of MT on the CEST spectrum was modeled by developing a set of steady state equations that could be effectively modeled at resonance offset (with respect to water) frequencies below 1 kHz. Previous attempts (35,82) could not extend below 1 kHz due to the approximations those models made about the RF saturation pulse: by assuming it was a square wave, they removed the spectral bandwidth of the pulse, and thus their models differed significantly from observed data. However, by appropriately modeling the RF saturation pulse, the work presented in this dissertation has removed the 1 kHz limitation of previous models. Thus, this new qMT model can be used to improve upon current CEST techniques by fitting the

MT and water components of the CEST spectrum. This qMT fit model will more appropriately isolate the CEST effect, and thus will provide more accurate measurements of the CEST effect than previous methods have been able to achieve. One side effect of previous approximations of the Bloch equations was that the T_2 of the free pool could not be adequately modeled due to the 1 kHz restriction, and thus, most qMT models have shown a reduction in the T_2 in the water pool. However, because the qMT model presented in this dissertation can extend below 1 kHz, it can more appropriately fit the water components of the model, and will therefore provide a more accurate estimate of the T_2 of the water pool.

Additionally, while not included in the text of this dissertation, DWS has prevented CEST species with resonance frequencies close to the water resonance from being detected at clinical field strengths. However, uniquely sampling the CEST spectrum using a variable power CEST (vCEST) technique will minimized DWS, increasing the sensitivity of CEST at resonances close to water. This technique was employed to measure the hydroxyl CEST effect in the knee cartilage of several patients, and our results demonstrated increased sensitivity to this CEST species over conventional CEST imaging. This work has been summarized in Clark, et al. (223). It is also theorized that fast exchanging species, such as glutamate, may display higher sensitivity when utilizing the vCEST method, however, previous attempts were significantly confounded by MT effects. By combining the new qMT model described in Chapter 6 with vCEST, these fast exchanging species may be able to be detected. The ability to detect these fast exchanging species at clinical field strengths greatly extends the versatility of CEST, and offers a viable alternative to CEST imaging in vivo at 7T.

In conclusion, qMT has been shown to be a remarkably important technique towards understanding the properties of myelin. The studies described here have provided further evidence that investigating the quantitative nature of MT can provide important benefits towards understanding and diagnosing neurodegenerative diseases. Gaining a fundamental understanding of how these disease processes affect the macromolecular structure of neural tissues may facilitate advances in the way we diagnose, treat, and hopefully cure disease. qMT may provide key contributions to this puzzle, and the studies described here have hopefully laid a foundation to drive these future discoveries.

REFERENCES:

1. Pike GB, Glover GH, Hu BS, Enzmann DR. Pulsed magnetization transfer spin-echo MR imaging. Journal of magnetic resonance imaging : JMRI 1993;3(3):531-539.
2. Kucharczyk W, Macdonald PM, Stanisz GJ, Henkelman RM. Relaxivity and magnetization transfer of white matter lipids at MR imaging: importance of cerebrosides and pH. Radiology 1994;192(2):521-529.
3. Morrison C, Stanisz G, Henkelman RM. Modeling magnetization transfer for biological-like systems using a semi-solid pool with a super-Lorentzian lineshape and dipolar reservoir. Journal of magnetic resonance Series B 1995;108(2):103-113.
4. Quesson B, Thiaudiere E, Delalande C, Dousset V, Chateil JF, Canioni P. Magnetization transfer imaging in vivo of the rat brain at 4.7 T: interpretation using a binary spin-bath model with a superLorentzian lineshape. Magnetic resonance in medicine : official journal of the Society of Magnetic Resonance in Medicine / Society of Magnetic Resonance in Medicine 1997;38(6):974-980.
5. Quesson B, Thiaudiere E, Delalande C, Chateil JF, Moonen CT, Canioni P. Magnetization transfer imaging of rat brain under non-steady-state conditions. Contrast prediction using a binary spin-bath model and a super-lorentzian lineshape. Journal of magnetic resonance 1998;130(2):321-328.
6. Berry I, Barker GJ, Barkhof F, Campi A, Dousset V, Franconi JM, Gass A, Schreiber W, Miller DH, Tofts PS. A multicenter measurement of magnetization transfer ratio in normal white matter. Journal of magnetic resonance imaging : JMRI 1999;9(3):441-446.
7. Henkelman RM, Stanisz GJ, Graham SJ. A multicenter measurement of magnetization transfer ratio in normal white matter. Journal of magnetic resonance imaging : JMRI 2000;11(5):568.
8. Ropele S, Stollberger R, Hartung HP, Fazekas F. Estimation of magnetization transfer rates from PACE experiments with pulsed RF saturation. Journal of magnetic resonance imaging : JMRI 2000;12(5):749-756.

9. Barker GJ, Schreiber WG, Gass A, Ranjeva JP, Campi A, van Waesberghe JH, Franconi JM, Watt HC, Tofts PS. A standardised method for measuring magnetisation transfer ratio on MR imagers from different manufacturers--the EuroMT sequence. Magma 2005;18(2):76-80.
10. Haacke EM, Cheng NY, House MJ, Liu Q, Neelavalli J, Ogg RJ, Khan A, Ayaz M, Kirsch W, Obenaus A. Imaging iron stores in the brain using magnetic resonance imaging. Magnetic resonance imaging 2005;23(1):1-25.
11. Filippi M, Rocca MA. Magnetization transfer magnetic resonance imaging of the brain, spinal cord, and optic nerve. Neurotherapeutics : the journal of the American Society for Experimental NeuroTherapeutics 2007;4(3):401-413.
12. Laule C, Vavasour IM, Kolind SH, Li DK, Traboulsee TL, Moore GR, MacKay AL. Magnetic resonance imaging of myelin. Neurotherapeutics : the journal of the American Society for Experimental NeuroTherapeutics 2007;4(3):460-484.
13. Schmierer K, Tozer DJ, Scaravilli F, Altmann DR, Barker GJ, Tofts PS, Miller DH. Quantitative magnetization transfer imaging in postmortem multiple sclerosis brain. Journal of magnetic resonance imaging : JMRI 2007;26(1):41-51.
14. Smith SA, Golay X, Fatemi A, Jones CK, Raymond GV, Moser HW, van Zijl PC. Magnetization transfer weighted imaging in the upper cervical spinal cord using cerebrospinal fluid as intersubject normalization reference (MTCSF imaging). Magnetic resonance in medicine : official journal of the Society of Magnetic Resonance in Medicine / Society of Magnetic Resonance in Medicine 2005;54(1):201-206.
15. Dortch RD, Welch EB, Gore JC, Smith SA. Quantitative Magnetization Transfer Imaging of Human Cervical Spinal Cord at 3T. 2010; Hawaii.
16. Edzes HT, Samulski ET. The measurement of cross-relaxation effects in the proton NMR spin-lattice relaxation of water in biological systems: Hydrated collagen and muscle. Journal of Magnetic Resonance (1969) 1978;31(2):207-229.
17. Sobol WT, Cameron IG, Inch WR, Pintar MM. Modeling of proton spin relaxation in muscle tissue using nuclear magnetic resonance spin grouping and exchange analysis. Biophys J 1986;50(1):181-191.

18. Caines GH, Schleich T, Rydzewski JM. Incorporation of Magnetization Transfer into the Formalism for Rotating-Frame Spin-Lattice Proton Nmr Relaxation in the Presence of an Off-Resonance-Irradiation Field. Journal of magnetic resonance 1991;95(3):558-566.
19. Morrison C, Henkelman RM. A model for magnetization transfer in tissues. Magnetic resonance in medicine : official journal of the Society of Magnetic Resonance in Medicine / Society of Magnetic Resonance in Medicine 1995;33(4):475-482.
20. Li K, Dortch RD, Welch EB, Bryant ND, Buck AK, Towse TF, Gochberg DF, Does MD, Damon BM, Park JH. Multi-parametric MRI characterization of healthy human thigh muscles at 3.0 T - relaxation, magnetization transfer, fat/water, and diffusion tensor imaging. NMR in biomedicine 2014;27(9):1070-1084.
21. Sinclair CD, Samson RS, Thomas DL, Weiskopf N, Lutti A, Thornton JS, Golay X. Quantitative magnetization transfer in in vivo healthy human skeletal muscle at 3 T. Magnetic resonance in medicine : official journal of the Society of Magnetic Resonance in Medicine / Society of Magnetic Resonance in Medicine 2010;64(6):1739-1748.
22. Louie EA, Gochberg DF, Does MD, Damon BM. Transverse relaxation and magnetization transfer in skeletal muscle: effect of pH. Magnetic resonance in medicine : official journal of the Society of Magnetic Resonance in Medicine / Society of Magnetic Resonance in Medicine 2009;61(3):560-569.
23. Boorstein JM, Moonis G, Boorstein SM, Patel YP, Culler AS. Optic neuritis: imaging with magnetization transfer. AJR American journal of roentgenology 1997;169(6):1709-1712.
24. Grossman RI, Barkhof F, Filippi M. Assessment of spinal cord damage in MS using MRI. Journal of the neurological sciences 2000;172:S36-S39.
25. Tozer D, Ramani A, Barker GJ, Davies GR, Miller DH, Tofts PS. Quantitative magnetization transfer mapping of bound protons in multiple sclerosis. Magnet Reson Med 2003;50(1):83-91.
26. Oh J, Henry RG, Genain C, Nelson SJ, Pelletier D. Mechanisms of normal appearing corpus callosum injury related to pericallosal T1 lesions in multiple sclerosis using directional diffusion tensor and 1H MRS imaging. Journal of neurology, neurosurgery, and psychiatry 2004;75(9):1281-1286.

27. Trip SA, Schlottmann PG, Jones SJ, Li WY, Garway-Heath DF, Thompson AJ, Plant GT, Miller DH. Optic nerve magnetization transfer imaging and measures of axonal loss and demyelination in optic neuritis. Multiple sclerosis 2007;13(7):875-879.
28. Levesque IR, Giacomini PS, Narayanan S, Ribeiro LT, Sled JG, Arnold DL, Pike GB. Quantitative magnetization transfer and myelin water imaging of the evolution of acute multiple sclerosis lesions. Magnetic resonance in medicine : official journal of the Society of Magnetic Resonance in Medicine / Society of Magnetic Resonance in Medicine 2010;63(3):633-640.
29. Berg S, Kaschka I, Utz KS, Huhn K, Lammer A, Lammer R, Waschbisch A, Kloska S, Lee DH, Doerfler A, Linker RA. Baseline magnetic resonance imaging of the optic nerve provides limited predictive information on short-term recovery after acute optic neuritis. PloS one 2015;10(1):e0113961.
30. Ercan E, Ingo C, Tritanon O, Magro-Checa C, Smith A, Smith S, Huizinga T, van Buchem MA, Ronen I. A multimodal MRI approach to identify and characterize microstructural brain changes in neuropsychiatric systemic lupus erythematosus. NeuroImage Clinical 2015;8:337-344.
31. Tambasco N, Nigro P, Romoli M, Simoni S, Parnetti L, Calabresi P. Magnetization transfer MRI in dementia disorders, Huntington's disease and parkinsonism. Journal of the neurological sciences 2015.
32. Mandl RC, Pasternak O, Cahn W, Kubicki M, Kahn RS, Shenton ME, Hulshoff Pol HE. Comparing free water imaging and magnetization transfer measurements in schizophrenia. Schizophr Res 2015;161(1):126-132.
33. Wolff SD, Balaban RS. Magnetization transfer contrast (MTC) and tissue water proton relaxation in vivo. Magnetic resonance in medicine : official journal of the Society of Magnetic Resonance in Medicine / Society of Magnetic Resonance in Medicine 1989;10(1):135-144.
34. Henkelman RM, Huang X, Xiang QS, Stanisz GJ, Swanson SD, Bronskill MJ. Quantitative interpretation of magnetization transfer. Magnetic resonance in medicine : official journal

of the Society of Magnetic Resonance in Medicine / Society of Magnetic Resonance in Medicine 1993;29(6):759-766.

35. Sled JG, Pike GB. Quantitative interpretation of magnetization transfer in spoiled gradient echo MRI sequences. Journal of magnetic resonance 2000;145(1):24-36.

36. Sled JG, Pike GB. Quantitative imaging of magnetization transfer exchange and relaxation properties in vivo using MRI. Magnetic resonance in medicine : official journal of the Society of Magnetic Resonance in Medicine / Society of Magnetic Resonance in Medicine 2001;46(5):923-931.

37. Yarnykh VL. Fast macromolecular proton fraction mapping from a single off-resonance magnetization transfer measurement. Magnetic resonance in medicine : official journal of the Society of Magnetic Resonance in Medicine / Society of Magnetic Resonance in Medicine 2012;68(1):166-178.

38. Smith SA, Golay X, Fatemi A, Mahmood A, Raymond GV, Moser HW, van Zijl PC, Stanisz GJ. Quantitative magnetization transfer characteristics of the human cervical spinal cord in vivo: application to adrenomyeloneuropathy. Magnetic resonance in medicine : official journal of the Society of Magnetic Resonance in Medicine / Society of Magnetic Resonance in Medicine 2009;61(1):22-27.

39. Portnoy S, Stanisz GJ. Modeling pulsed magnetization transfer. Magnetic resonance in medicine : official journal of the Society of Magnetic Resonance in Medicine / Society of Magnetic Resonance in Medicine 2007;58(1):144-155.

40. Desmond KL, Stanisz GJ. Understanding quantitative pulsed CEST in the presence of MT. Magnetic resonance in medicine : official journal of the Society of Magnetic Resonance in Medicine / Society of Magnetic Resonance in Medicine 2012;67(4):979-990.

41. Zaiß M, Schmitt B, Bachert P. Quantitative separation of CEST effect from magnetization transfer and spillover effects by Lorentzian-line-fit analysis of z-spectra. Journal of magnetic resonance 2011;211(2):149-155.

42. Zaiss M, Windschuh J, Paech D, Meissner JE, Burth S, Schmitt B, Kickingereder P, Wiestler B, Wick W, Bendszus M, Schlemmer HP, Ladd ME, Bachert P, Radbruch A. Relaxation-

compensated CEST-MRI of the human brain at 7T: Unbiased insight into NOE and amide signal changes in human glioblastoma. NeuroImage 2015;112:180-188.

43. Jones CK, Polders D, Hua J, Zhu H, Hoogduin HJ, Zhou J, Luijten P, van Zijl PC. In vivo three-dimensional whole-brain pulsed steady-state chemical exchange saturation transfer at 7 T. Magnetic resonance in medicine : official journal of the Society of Magnetic Resonance in Medicine / Society of Magnetic Resonance in Medicine 2012;67(6):1579-1589.
44. Zaiss M, Zu Z, Xu J, Schuenke P, Gochberg DF, Gore JC, Ladd ME, Bachert P. A combined analytical solution for chemical exchange saturation transfer and semi-solid magnetization transfer. NMR in biomedicine 2015;28(2):217-230.
45. Zaiss M, Xu J, Goerke S, Khan IS, Singer RJ, Gore JC, Gochberg DF, Bachert P. Inverse Z-spectrum analysis for spillover-, MT-, and T1 -corrected steady-state pulsed CEST-MRI - application to pH-weighted MRI of acute stroke. NMR in biomedicine 2014;27(3):240-252.
46. Bloch F. Nuclear Induction. Physical Review 1946;70(7-8):460-474.
47. Bloch F. The Principle of Nuclear Induction. Science 1953;118(3068):425-430.
48. Knight WD. Nuclear Magnetic Resonance Shift in Metals. Physical Review 1949;76(8):1259-1260.
49. Dickinson WC. Dependence of the F-19 Nuclear Resonance Position on Chemical Compound. Physical Review 1950;77(5):736-737.
50. Proctor WG, Yu FC. The Dependence of a Nuclear Magnetic Resonance Frequency upon Chemical Compound. Physical Review 1950;77(5):717-717.
51. Gutowsky HS, McCall DW, Slichter CP. Nuclear Magnetic Resonance Multiplets in Liquids. The Journal of Chemical Physics 1953;21(2):279-292.
52. McConnell HM. Reaction Rates by Nuclear Magnetic Resonance. The Journal of Chemical Physics 1958;28(3):430-431.
53. Edzes HT, Samulski ET. Cross relaxation and spin diffusion in the proton NMR or hydrated collagen. Nature 1977;265(5594):521-523.
54. Hoffman RA, Forsén S. Transient and Steady-State Overhauser Experiments in the Investigation of Relaxation Processes. Analogies between Chemical Exchange and Relaxation. The Journal of Chemical Physics 1966;45(6):2049-2060.

55. Alger JR, Shulman RG. NMR studies of enzymatic rates in vitro and in vivo by magnetization transfer. Q Rev Biophys 1984;17(1):83-124.

56. Chai JW, Chen C, Chen JH, Lee SK, Yeung HN. Estimation of in vivo proton intrinsic and cross-relaxation rate in human brain. Magnetic resonance in medicine : official journal of the Society of Magnetic Resonance in Medicine / Society of Magnetic Resonance in Medicine 1996;36(1):147-152.

57. Gochberg DF, Kennan RP, Robson MD, Gore JC. Quantitative imaging of magnetization transfer using multiple selective pulses. Magnetic resonance in medicine : official journal of the Society of Magnetic Resonance in Medicine / Society of Magnetic Resonance in Medicine 1999;41(5):1065-1072.

58. Smith SA, Edden RA, Farrell JA, Barker PB, Van Zijl PC. Measurement of T1 and T2 in the cervical spinal cord at 3 tesla. Magnetic resonance in medicine : official journal of the Society of Magnetic Resonance in Medicine / Society of Magnetic Resonance in Medicine 2008;60(1):213-219.

59. Gochberg DF, Kennan RP, Gore JC. Quantitative studies of magnetization transfer by selective excitation and T1 recovery. Magnetic resonance in medicine : official journal of the Society of Magnetic Resonance in Medicine / Society of Magnetic Resonance in Medicine 1997;38(2):224-231.

60. Eng J, Ceckler TL, Balaban RS. Quantitative 1H magnetization transfer imaging in vivo. Magnetic resonance in medicine : official journal of the Society of Magnetic Resonance in Medicine / Society of Magnetic Resonance in Medicine 1991;17(2):304-314.

61. Grad J, Mendelson D, Hyder F, Bryant RG. Applications of nuclear magnetic cross-relaxation spectroscopy to tissues. Magnetic resonance in medicine : official journal of the Society of Magnetic Resonance in Medicine / Society of Magnetic Resonance in Medicine 1991;17(2):452-459.

62. Grad J, Bryant RG. Nuclear magnetic cross-relaxation spectroscopy. Journal of Magnetic Resonance (1969) 1990;90(1):1-8.

63. Grad J, Mendelson D, Hyder F, Bryant RG. Direct measurements of longitudinal relaxation and magnetization transfer in heterogeneous systems. Journal of Magnetic Resonance (1969) 1990;86(2):416-419.
64. Koenig SH, Brown RD, 3rd. A molecular theory of relaxation and magnetization transfer: application to cross-linked BSA, a model for tissue. Magnetic resonance in medicine : official journal of the Society of Magnetic Resonance in Medicine / Society of Magnetic Resonance in Medicine 1993;30(6):685-695.
65. Wu X. Lineshape of magnetization transfer via cross relaxation. Journal of Magnetic Resonance (1969) 1991;94(1):186-190.
66. Anet FAL, O'Leary DJ. NMR lineshapes caused by transverse cross relaxation of nearly like spins. Journal of Magnetic Resonance (1969) 1990;86(2):358-370.
67. Vasavada KV, Kaplan JI. Distinction between linewidths of identical and nonidentical dipolar-coupled systems with and without exchange. Journal of Magnetic Resonance (1969) 1985;62(1):37-41.
68. Li JG, Graham SJ, Henkelman RM. A flexible magnetization transfer line shape derived from tissue experimental data. Magnetic resonance in medicine : official journal of the Society of Magnetic Resonance in Medicine / Society of Magnetic Resonance in Medicine 1997;37(6):866-871.
69. Henkelman RM, Stanisz GJ, Graham SJ. Magnetization transfer in MRI: a review. NMR in biomedicine 2001;14(2):57-64.
70. Stanisz GJ, Kecojevic A, Bronskill MJ, Henkelman RM. Characterizing white matter with magnetization transfer and T(2). Magnetic resonance in medicine : official journal of the Society of Magnetic Resonance in Medicine / Society of Magnetic Resonance in Medicine 1999;42(6):1128-1136.
71. Graham SJ, Henkelman RM. Pulsed magnetization transfer imaging: evaluation of technique. Radiology 1999;212(3):903-910.
72. Koenig SH. Cholesterol of myelin is the determinant of gray-white contrast in MRI of brain. Magnetic resonance in medicine : official journal of the Society of Magnetic Resonance in Medicine / Society of Magnetic Resonance in Medicine 1991;20(2):285-291.

73. Stanisz GJ, Odrobina EE, Pun J, Escaravage M, Graham SJ, Bronskill MJ, Henkelman RM. T1, T2 relaxation and magnetization transfer in tissue at 3T. Magnetic resonance in medicine : official journal of the Society of Magnetic Resonance in Medicine / Society of Magnetic Resonance in Medicine 2005;54(3):507-512.

74. Levesque IR, Sled JG, Narayanan S, Giacomini PS, Ribeiro LT, Arnold DL, Pike GB. Reproducibility of quantitative magnetization-transfer imaging parameters from repeated measurements. Magnetic resonance in medicine : official journal of the Society of Magnetic Resonance in Medicine / Society of Magnetic Resonance in Medicine 2010;64(2):391-400.

75. Samson RS, Ciccarelli O, Kachramanoglou C, Brightman L, Lutti A, Thomas DL, Weiskopf N, Wheeler-Kingshott CA. Tissue- and column-specific measurements from multi-parameter mapping of the human cervical spinal cord at 3 T. NMR in biomedicine 2013;26(12):1823-1830.

76. Smith AK, Dortch RD, Dethrage LM, Smith SA. Rapid, high-resolution quantitative magnetization transfer MRI of the human spinal cord. NeuroImage 2014;95:106-116.

77. Smith AK, Dortch RD, Dethrage LM, Lyttle BD, Kang H, Welch EB, Smith SA. Incorporating dixon multi-echo fat water separation for novel quantitative magnetization transfer of the human optic nerve in vivo. Magnetic resonance in medicine : official journal of the Society of Magnetic Resonance in Medicine / Society of Magnetic Resonance in Medicine 2016.

78. Yarnykh VL. Pulsed Z-spectroscopic imaging of cross-relaxation parameters in tissues for human MRI: theory and clinical applications. Magnetic resonance in medicine : official journal of the Society of Magnetic Resonance in Medicine / Society of Magnetic Resonance in Medicine 2002;47(5):929-939.

79. Yarnykh VL. Optimal radiofrequency and gradient spoiling for improved accuracy of T1 and B1 measurements using fast steady-state techniques. Magnetic resonance in medicine : official journal of the Society of Magnetic Resonance in Medicine / Society of Magnetic Resonance in Medicine 2010;63(6):1610-1626.

80. Mossahebi P, Yarnykh VL, Samsonov A. Analysis and correction of biases in cross-relaxation MRI due to biexponential longitudinal relaxation. Magnetic resonance in medicine : official journal of the Society of Magnetic Resonance in Medicine / Society of Magnetic Resonance in Medicine 2013.
81. Sritanyaratana N, Samsonov A, Mossahebi P, Wilson JJ, Block WF, Kijowski R. Cross-relaxation imaging of human patellar cartilage in vivo at 3.0T. Osteoarthritis Cartilage 2014;22(10):1568-1576.
82. Yarnykh VL, Yuan C. Cross-relaxation imaging reveals detailed anatomy of white matter fiber tracts in the human brain. NeuroImage 2004;23(1):409-424.
83. Listerud J. Off-resonance pulsed magnetization transfer in clinical MR imaging: optimization by an analysis of transients. Magnetic resonance in medicine : official journal of the Society of Magnetic Resonance in Medicine / Society of Magnetic Resonance in Medicine 1997;37(5):693-705.
84. van Zijl PC, Yadav NN. Chemical exchange saturation transfer (CEST): what is in a name and what isn't? Magnetic resonance in medicine : official journal of the Society of Magnetic Resonance in Medicine / Society of Magnetic Resonance in Medicine 2011;65(4):927-948.
85. McMahon MT, Gilad AA, Zhou J, Sun PZ, Bulte JW, van Zijl PC. Quantifying exchange rates in chemical exchange saturation transfer agents using the saturation time and saturation power dependencies of the magnetization transfer effect on the magnetic resonance imaging signal (QUEST and QUESP): Ph calibration for poly-L-lysine and a starburst dendrimer. Magnetic resonance in medicine : official journal of the Society of Magnetic Resonance in Medicine / Society of Magnetic Resonance in Medicine 2006;55(4):836-847.
86. Zhou J, Wilson DA, Sun PZ, Klaus JA, Van Zijl PC. Quantitative description of proton exchange processes between water and endogenous and exogenous agents for WEX, CEST, and APT experiments. Magnetic resonance in medicine : official journal of the Society of Magnetic Resonance in Medicine / Society of Magnetic Resonance in Medicine 2004;51(5):945-952.

87. Snoussi K, Bulte JW, Gueron M, van Zijl PC. Sensitive CEST agents based on nucleic acid imino proton exchange: detection of poly(rU) and of a dendrimer-poly(rU) model for nucleic acid delivery and pharmacology. Magnetic resonance in medicine : official journal of the Society of Magnetic Resonance in Medicine / Society of Magnetic Resonance in Medicine 2003;49(6):998-1005.

88. Zhou J, Payen JF, Wilson DA, Traystman RJ, van Zijl PC. Using the amide proton signals of intracellular proteins and peptides to detect pH effects in MRI. Nature medicine 2003;9(8):1085-1090.

89. Liepinsh E, Otting G. Proton exchange rates from amino acid side chains--implications for image contrast. Magnetic resonance in medicine : official journal of the Society of Magnetic Resonance in Medicine / Society of Magnetic Resonance in Medicine 1996;35(1):30-42.

90. Hua J, Jones CK, Blakeley J, Smith SA, van Zijl PC, Zhou J. Quantitative description of the asymmetry in magnetization transfer effects around the water resonance in the human brain. Magnetic resonance in medicine : official journal of the Society of Magnetic Resonance in Medicine / Society of Magnetic Resonance in Medicine 2007;58(4):786-793.

91. Sun PZ, Sorensen AG. Imaging pH using the chemical exchange saturation transfer (CEST) MRI: Correction of concomitant RF irradiation effects to quantify CEST MRI for chemical exchange rate and pH. Magnetic resonance in medicine : official journal of the Society of Magnetic Resonance in Medicine / Society of Magnetic Resonance in Medicine 2008;60(2):390-397.

92. Ward KM, Aletras AH, Balaban RS. A new class of contrast agents for MRI based on proton chemical exchange dependent saturation transfer (CEST). Journal of magnetic resonance 2000;143(1):79-87.

93. Sun PZ, Murata Y, Lu J, Wang X, Lo EH, Sorensen AG. Relaxation-compensated fast multislice amide proton transfer (APT) imaging of acute ischemic stroke. Magnetic resonance in medicine : official journal of the Society of Magnetic Resonance in Medicine / Society of Magnetic Resonance in Medicine 2008;59(5):1175-1182.

94. Liu G, Li Y, Sheth VR, Pagel MD. Imaging in vivo extracellular pH with a single paramagnetic chemical exchange saturation transfer magnetic resonance imaging contrast agent. Molecular imaging 2012;11(1):47-57.

95. Schmitt B, Zamecnik P, Zaiss M, Rerich E, Schuster L, Bachert P, Schlemmer HP. A new contrast in MR mammography by means of chemical exchange saturation transfer (CEST) imaging at 3 Tesla: preliminary results. RoFo : Fortschritte auf dem Gebiete der Rontgenstrahlen und der Nuklearmedizin 2011;183(11):1030-1036.

96. Zhou J, Blakeley JO, Hua J, Kim M, Laterra J, Pomper MG, van Zijl PC. Practical data acquisition method for human brain tumor amide proton transfer (APT) imaging. Magnetic resonance in medicine : official journal of the Society of Magnetic Resonance in Medicine / Society of Magnetic Resonance in Medicine 2008;60(4):842-849.

97. Guivel-Scharen V, Sinnwell T, Wolff SD, Balaban RS. Detection of proton chemical exchange between metabolites and water in biological tissues. Journal of magnetic resonance 1998;133(1):36-45.

98. Mulkern RV, Williams ML. The general solution to the Bloch equation with constant rf and relaxation terms: application to saturation and slice selection. Medical physics 1993;20(1):5-13.

99. Smith SA, Bulte JW, van Zijl PC. Direct saturation MRI: theory and application to imaging brain iron. Magnetic resonance in medicine : official journal of the Society of Magnetic Resonance in Medicine / Society of Magnetic Resonance in Medicine 2009;62(2):384-393.

100. Edgar JM, McLaughlin M, Yool D, Zhang SC, Fowler JH, Montague P, Barrie JA, McCulloch MC, Duncan ID, Garbern J, Nave KA, Griffiths IR. Oligodendroglial modulation of fast axonal transport in a mouse model of hereditary spastic paraplegia. J Cell Biol 2004;166(1):121-131.

101. Bjartmar C, Trapp BD. Axonal and neuronal degeneration in multiple sclerosis: mechanisms and functional consequences. Current opinion in neurology 2001;14(3):271-278.

102. Kirkpatrick LL, Witt AS, Payne HR, Shine HD, Brady ST. Changes in microtubule stability and density in myelin-deficient shiverer mouse CNS axons. The Journal of neuroscience : the official journal of the Society for Neuroscience 2001;21(7):2288-2297.
103. Edgar JM, Garbern J. The myelinated axon is dependent on the myelinating cell for support and maintenance: molecules involved. Journal of neuroscience research 2004;76(5):593-598.
104. Boucher SE, Cypher MA, Carlock LR, Skoff RP. Proteolipid protein gene modulates viability and phenotype of neurons. The Journal of neuroscience : the official journal of the Society for Neuroscience 2002;22(5):1772-1783.
105. Dyer CA. The structure and function of myelin: from inert membrane to perfusion pump. Neurochem Res 2002;27(11):1279-1292.
106. Keegan BM, Noseworthy JH. Multiple sclerosis. Annu Rev Med 2002;53:285-302.
107. van Waesberghe JH, Kamphorst W, De Groot CJ, van Walderveen MA, Castelijns JA, Ravid R, Lycklama a Nijeholt GJ, van der Valk P, Polman CH, Thompson AJ, Barkhof F. Axonal loss in multiple sclerosis lesions: magnetic resonance imaging insights into substrates of disability. Annals of neurology 1999;46(5):747-754.
108. Ikuta F, Zimmerman HM. Distribution of plaques in seventy autopsy cases of multiple sclerosis in the United States. Neurology 1976;26(6 PT 2):26-28.
109. Pane A, Burdon MA, Miller NR. The Neuro-ophthalmology Survival Guide. London: Mosby/Elsevier; 2007.
110. Optic Neuritis Study G. Multiple sclerosis risk after optic neuritis: final optic neuritis treatment trial follow-up. Archives of neurology 2008;65(6):727-732.
111. Dixon WT. Simple proton spectroscopic imaging. Radiology 1984;153(1):189-194.
112. Varma G, Duhamel G, de Bazelaire C, Alsop DC. Magnetization transfer from inhomogeneously broadened lines: A potential marker for myelin. Magnetic resonance in medicine : official journal of the Society of Magnetic Resonance in Medicine / Society of Magnetic Resonance in Medicine 2015;73(2):614-622.
113. Girard OM, Prevost VH, Varma G, Cozzone PJ, Alsop DC, Duhamel G. Magnetization transfer from inhomogeneously broadened lines (ihMT): Experimental optimization of

saturation parameters for human brain imaging at 1.5 Tesla. Magnetic resonance in medicine : official journal of the Society of Magnetic Resonance in Medicine / Society of Magnetic Resonance in Medicine 2015;73(6):2111-2121.

114. Shams PN, Plant GT. Optic neuritis: a review. International MS journal / MS Forum 2009;16(3):82-89.

115. Cohen-Adad J, El Mendili MM, Lehericy S, Pradat PF, Blancho S, Rossignol S, Benali H. Demyelination and degeneration in the injured human spinal cord detected with diffusion and magnetization transfer MRI. NeuroImage 2011;55(3):1024-1033.

116. Dortch RD, Dethrage LM, Gore JC, Smith SA, Li J. Proximal nerve magnetization transfer MRI relates to disability in Charcot-Marie-Tooth diseases. Neurology 2014;83(17):1545-1553.

117. Ellingson BM, Ulmer JL, Kurpad SN, Schmit BD. Diffusion tensor MR imaging in chronic spinal cord injury. AJNR American journal of neuroradiology 2008;29(10):1976-1982.

118. Filippi M, Agosta F. Imaging biomarkers in multiple sclerosis. Journal of magnetic resonance imaging : JMRI 2010;31(4):770-788.

119. Freund P, Wheeler-Kingshott C, Jackson J, Miller D, Thompson A, Ciccarelli O. Recovery after spinal cord relapse in multiple sclerosis is predicted by radial diffusivity. Multiple sclerosis 2010;16(10):1193-1202.

120. Nair G, Carew JD, Usher S, Lu D, Hu XP, Benatar M. Diffusion tensor imaging reveals regional differences in the cervical spinal cord in amyotrophic lateral sclerosis. NeuroImage 2010;53(2):576-583.

121. Naismith RT, Xu J, Klawiter EC, Lancia S, Tutlam NT, Wagner JM, Qian P, Trinkaus K, Song SK, Cross AH. Spinal cord tract diffusion tensor imaging reveals disability substrate in demyelinating disease. Neurology 2013;80(24):2201-2209.

122. Poloni G, Minagar A, Haacke EM, Zivadinov R. Recent developments in imaging of multiple sclerosis. The neurologist 2011;17(4):185-204.

123. Zackowski KM, Smith SA, Reich DS, Gordon-Lipkin E, Chodkowski BA, Sambandan DR, Shteyman M, Bastian AJ, van Zijl PC, Calabresi PA. Sensorimotor dysfunction in multiple

sclerosis and column-specific magnetization transfer-imaging abnormalities in the spinal cord. Brain : a journal of neurology 2009;132(Pt 5):1200-1209.

124. Hinton DP, Bryant RG. 1H magnetic cross-relaxation between multiple solvent components and rotationally immobilized protein. Magnetic resonance in medicine : official journal of the Society of Magnetic Resonance in Medicine / Society of Magnetic Resonance in Medicine 1996;35(4):497-505.

125. Odrobina EE, Lam TY, Pun T, Midha R, Stanisz GJ. MR properties of excised neural tissue following experimentally induced demyelination. NMR in biomedicine 2005;18(5):277-284.

126. Ou X, Sun SW, Liang HF, Song SK, Gochberg DF. The MT pool size ratio and the DTI radial diffusivity may reflect the myelination in shiverer and control mice. NMR in biomedicine 2009;22(5):480-487.

127. Underhill HR, Rostomily RC, Mikheev AM, Yuan C, Yarnykh VL. Fast bound pool fraction imaging of the in vivo rat brain: association with myelin content and validation in the C6 glioma model. NeuroImage 2011;54(3):2052-2065.

128. Harrigan RL, Plassard AJ, Mawn LA, Galloway RL, Smith SA, Landman BA. Constructing a statistical atlas of the radii of the optic nerve and cerebrospinal fluid sheath in young healthy adults. Proc Soc Photo Opt Instrum Eng 2015;9413.

129. Kaldoudi E, Williams SC, Barker GJ, Tofts PS. A chemical shift selective inversion recovery sequence for fat-suppressed MRI: theory and experimental validation. Magnetic resonance imaging 1993;11(3):341-355.

130. Zhou XJ, Bernstein MA, King KF. Chapter 6 - Adiabatic Radiofrequency Pulses. Handbook of MRI Pulse Sequences. Burlington: Academic Press; 2004. p 177-212.

131. Dwyer AJ, Frank JA, Sank VJ, Reinig JW, Hickey AM, Doppman JL. Short-Ti inversion-recovery pulse sequence: analysis and initial experience in cancer imaging. Radiology 1988;168(3):827-836.

132. Berglund J, Kullberg J. Three-dimensional water/fat separation and T2* estimation based on whole-image optimization--application in breathhold liver imaging at 1.5 T. Magnetic

resonance in medicine : official journal of the Society of Magnetic Resonance in Medicine / Society of Magnetic Resonance in Medicine 2012;67(6):1684-1693.

133. Dimitrov I. mDIXON Quant delivers robust, high quality fat quantification. Volume 2015. http://clinical.netforum.healthcare.philips.com/global/Explore/White-Papers/MRI/mDIXON-Quant-delivers-robust-high-quality-fat-quantification: Philips Healthcare; 2014.

134. Eggers H, Brendel B, Duijndam A, Herigault G. Dual-echo Dixon imaging with flexible choice of echo times. Magnetic resonance in medicine : official journal of the Society of Magnetic Resonance in Medicine / Society of Magnetic Resonance in Medicine 2011;65(1):96-107.

135. Glover GH, Schneider E. Three-point Dixon technique for true water/fat decomposition with B0 inhomogeneity correction. Magnetic resonance in medicine : official journal of the Society of Magnetic Resonance in Medicine / Society of Magnetic Resonance in Medicine 1991;18(2):371-383.

136. Hardy PA, Hinks RS, Tkach JA. Separation of fat and water in fast spin-echo MR imaging with the three-point Dixon technique. Journal of magnetic resonance imaging : JMRI 1995;5(2):181-185.

137. Gold GE, Han E, Stainsby J, Wright G, Brittain J, Beaulieu C. Musculoskeletal MRI at 3.0 T: relaxation times and image contrast. AJR American journal of roentgenology 2004;183(2):343-351.

138. Pelli DG. The VideoToolbox software for visual psychophysics: transforming numbers into movies. Spat Vis 1997;10(4):437-442.

139. Zhang Y, Nateras OS, Peng Q, Kuranov RV, Harrison JM, Milner TE, Duong TQ. Lamina-specific anatomic magnetic resonance imaging of the human retina. Investigative ophthalmology & visual science 2011;52(10):7232-7237.

140. Beenakker JW, van Rijn GA, Luyten GP, Webb AG. High-resolution MRI of uveal melanoma using a microcoil phased array at 7 T. NMR in biomedicine 2013;26(12):1864-1869.

141. Brainard DH. The Psychophysics Toolbox. Spat Vis 1997;10(4):433-436.

142. Yarnykh VL. Actual flip-angle imaging in the pulsed steady state: a method for rapid three-dimensional mapping of the transmitted radiofrequency field. Magnetic resonance in medicine : official journal of the Society of Magnetic Resonance in Medicine / Society of Magnetic Resonance in Medicine 2007;57(1):192-200.
143. Smith SM. Fast robust automated brain extraction. Human brain mapping 2002;17(3):143-155.
144. Jenkinson M, Pechaud M, Smith S. BET2: MR-based estimation of brain, skull and scalp surfaces.; 2005.
145. Jenkinson M, Smith S. A global optimisation method for robust affine registration of brain images. Medical image analysis 2001;5(2):143-156.
146. Jenkinson M, Bannister P, Brady M, Smith S. Improved optimization for the robust and accurate linear registration and motion correction of brain images. NeuroImage 2002;17(2):825-841.
147. Jenkinson M, Beckmann CF, Behrens TE, Woolrich MW, Smith SM. Fsl. NeuroImage 2012;62(2):782-790.
148. Fram EK, Herfkens RJ, Johnson GA, Glover GH, Karis JP, Shimakawa A, Perkins TG, Pelc NJ. Rapid calculation of T1 using variable flip angle gradient refocused imaging. Magnetic resonance imaging 1987;5(3):201-208.
149. Jeong HK, Dewey BE, Hirtle JA, Lavin P, Sriram S, Pawate S, Gore JC, Anderson AW, Kang H, Smith SA. Improved diffusion tensor imaging of the optic nerve using multishot two-dimensional navigated acquisitions. Magnetic resonance in medicine : official journal of the Society of Magnetic Resonance in Medicine / Society of Magnetic Resonance in Medicine 2015;74(4):953-963.
150. Bonini RH, Zeotti D, Saraiva LA, Trad CS, Filho JM, Carrara HH, de Andrade JM, Santos AC, Muglia VF. Magnetization transfer ratio as a predictor of malignancy in breast lesions: preliminary results. Magnetic resonance in medicine : official journal of the Society of Magnetic Resonance in Medicine / Society of Magnetic Resonance in Medicine 2008;59(5):1030-1034.
151. Schmitt F, Stehling MK, Turner R. Echo-Planar Imaging. Berlin, Germany: Springer; 1998.

152. Li K, Dortch RD, Kroop SF, Huston JW, Gochberg DF, Park JH, Damon BM. A Rapid Approach for Quantitative Magnetization Transfer Imaging in Thigh Muscles using the Pulsed Saturation Method. Magnetic resonance imaging 2015.

153. Falconer JC, Narayana PA. Cerebrospinal fluid-suppressed high-resolution diffusion imaging of human brain. Magnetic resonance in medicine : official journal of the Society of Magnetic Resonance in Medicine / Society of Magnetic Resonance in Medicine 1997;37(1):119-123.

154. Bhagat YA, Beaulieu C. Diffusion anisotropy in subcortical white matter and cortical gray matter: changes with aging and the role of CSF-suppression. Journal of magnetic resonance imaging : JMRI 2004;20(2):216-227.

155. Li L, Miller KL, Jezzard P. DANTE-prepared pulse trains: a novel approach to motion-sensitized and motion-suppressed quantitative magnetic resonance imaging. Magnetic resonance in medicine : official journal of the Society of Magnetic Resonance in Medicine / Society of Magnetic Resonance in Medicine 2012;68(5):1423-1438.

156. Mossahebi P, Alexander AL, Field AS, Samsonov AA. Removal of cerebrospinal fluid partial volume effects in quantitative magnetization transfer imaging using a three-pool model with nonexchanging water component. Magnetic resonance in medicine : official journal of the Society of Magnetic Resonance in Medicine / Society of Magnetic Resonance in Medicine 2014.

157. Cohen AB, Neema M, Arora A, Dell'oglio E, Benedict RH, Tauhid S, Goldberg-Zimring D, Chavarro-Nieto C, Ceccarelli A, Klein JP, Stankiewicz JM, Houtchens MK, Buckle GJ, Alsop DC, Guttmann CR, Bakshi R. The relationships among MRI-defined spinal cord involvement, brain involvement, and disability in multiple sclerosis. Journal of neuroimaging : official journal of the American Society of Neuroimaging 2012;22(2):122-128.

158. Rocca MA, Horsfield MA, Sala S, Copetti M, Valsasina P, Mesaros S, Martinelli V, Caputo D, Stosic-Opincal T, Drulovic J, Comi G, Filippi M. A multicenter assessment of cervical cord atrophy among MS clinical phenotypes. Neurology 2011;76(24):2096-2102.

159. Stankiewicz JM, Neema M, Alsop DC, Healy BC, Arora A, Buckle GJ, Chitnis T, Guttmann CR, Hackney D, Bakshi R. Spinal cord lesions and clinical status in multiple sclerosis: A 1.5 T and 3 T MRI study. Journal of the neurological sciences 2009;279(1-2):99-105.

160. Oh J, Saidha S, Chen M, Smith SA, Prince J, Jones C, Diener-West M, van Zijl PC, Reich DS, Calabresi PA. Spinal cord quantitative MRI discriminates between disability levels in multiple sclerosis. Neurology 2013;80(6):540-547.

161. Wheeler-Kingshott CA, Stroman PW, Schwab JM, Bacon M, Bosma R, Brooks J, Cadotte DW, Carlstedt T, Ciccarelli O, Cohen-Adad J, Curt A, Evangelou N, Fehlings MG, Filippi M, Kelley BJ, Kollias S, Mackay A, Porro CA, Smith S, Strittmatter SM, Summers P, Thompson AJ, Tracey I. The current state-of-the-art of spinal cord imaging: Applications. NeuroImage 2014;84:1082-1093.

162. Stroman PW, Wheeler-Kingshott C, Bacon M, Schwab JM, Bosma R, Brooks J, Cadotte D, Carlstedt T, Ciccarelli O, Cohen-Adad J, Curt A, Evangelou N, Fehlings MG, Filippi M, Kelley BJ, Kollias S, Mackay A, Porro CA, Smith S, Strittmatter SM, Summers P, Tracey I. The current state-of-the-art of spinal cord imaging: Methods. NeuroImage 2014;84:1070-1081.

163. Held P, Dorenbeck U, Seitz J, Frund R, Albrich H. MRI of the abnormal cervical spinal cord using 2D spoiled gradient echo multiecho sequence (MEDIC) with magnetization transfer saturation pulse. A T2* weighted feasibility study. Journal of neuroradiology Journal de neuroradiologie 2003;30(2):83-90.

164. Bland JM, Altman DG. Statistical methods for assessing agreement between two methods of clinical measurement. Lancet 1986;1(8476):307-310.

165. Rovaris M, Judica E, Ceccarelli A, Ghezzi A, Martinelli V, Comi G, Filippi M. Absence of diffuse cervical cord tissue damage in early, non-disabling relapsing-remitting MS: a preliminary study. Multiple sclerosis 2008;14(6):853-856.

166. Hickman SJ, Hadjiprocopis A, Coulon O, Miller DH, Barker GJ. Cervical spinal cord MTR histogram analysis in multiple sclerosis using a 3D acquisition and a B-spline active surface segmentation technique. Magnetic resonance imaging 2004;22(6):891-895.

167. Tozer DJ, Rees JH, Benton CE, Waldman AD, Jager HR, Tofts PS. Quantitative magnetisation transfer imaging in glioma: preliminary results. NMR in biomedicine 2011;24(5):492-498.

168. Kearney H, Miller DH, Ciccarelli O. Spinal cord MRI in multiple sclerosis--diagnostic, prognostic and clinical value. Nat Rev Neurol 2015;11(6):327-338.

169. Gass A, Filippi M, Rodegher M, Schwartz A, Comi G, Hennerici M. Characteristics of chronic MS lesions in the cerebrum, brainstem, spinal cord, and optic nerve on T1---weighted MRI. Neurology 1998;50(2):548-550.

170. Bergers E, Bot JC, De Groot CJ, Polman CH, Lycklama a Nijeholt GJ, Castelijns JA, van der Valk P, Barkhof F. Axonal damage in the spinal cord of MS patients occurs largely independent of T2 MRI lesions. Neurology 2002;59(11):1766-1771.

171. Patrucco L, Rojas JI, Cristiano E. Assessing the value of spinal cord lesions in predicting development of multiple sclerosis in patients with clinically isolated syndromes. Journal of neurology 2012;259(7):1317-1320.

172. Miller DH. Magnetic resonance in monitoring the treatment of multiple sclerosis. Annals of neurology 1994;36 Suppl:S91-94.

173. Androdias G, Reynolds R, Chanal M, Ritleng C, Confavreux C, Nataf S. Meningeal T cells associate with diffuse axonal loss in multiple sclerosis spinal cords. Annals of neurology 2010;68(4):465-476.

174. DeLuca GC, Alterman R, Martin JL, Mittal A, Blundell S, Bird S, Beale H, Hong LS, Esiri MM. Casting light on multiple sclerosis heterogeneity: the role of HLA-DRB1 on spinal cord pathology. Brain : a journal of neurology 2013;136(Pt 4):1025-1034.

175. Kearney H, Yiannakas MC, Samson RS, Wheeler-Kingshott CA, Ciccarelli O, Miller DH. Investigation of magnetization transfer ratio-derived pial and subpial abnormalities in the multiple sclerosis spinal cord. Brain : a journal of neurology 2014;137(Pt 9):2456-2468.

176. Samsonov A, Alexander AL, Mossahebi P, Wu YC, Duncan ID, Field AS. Quantitative MR imaging of two-pool magnetization transfer model parameters in myelin mutant shaking pup. NeuroImage 2012;62(3):1390-1398.

177. Ou X, Sun SW, Liang HF, Song SK, Gochberg DF. Quantitative magnetization transfer measured pool-size ratio reflects optic nerve myelin content in ex vivo mice. Magnetic resonance in medicine : official journal of the Society of Magnetic Resonance in Medicine / Society of Magnetic Resonance in Medicine 2009;61(2):364-371.

178. Rausch M, Tofts P, Lervik P, Walmsley A, Mir A, Schubart A, Seabrook T. Characterization of white matter damage in animal models of multiple sclerosis by magnetization transfer ratio and quantitative mapping of the apparent bound proton fraction f. Multiple sclerosis 2009;15(1):16-27.

179. Davies GR, Tozer DJ, Cercignani M, Ramani A, Dalton CM, Thompson AJ, Barker GJ, Tofts PS, Miller DH. Estimation of the macromolecular proton fraction and bound pool T2 in multiple sclerosis. Multiple sclerosis 2004;10(6):607-613.

180. Yarnykh VL, Bowen JD, Samsonov A, Repovic P, Mayadev A, Qian P, Gangadharan B, Keogh BP, Maravilla KR, Jung Henson LK. Fast Whole-Brain Three-dimensional Macromolecular Proton Fraction Mapping in Multiple Sclerosis. Radiology 2015;274(1):210-220.

181. Asman AJ, Landman BA. Formulating spatially varying performance in the statistical fusion framework. IEEE transactions on medical imaging 2012;31(6):1326-1336.

182. Asman AJ, Landman BA. Non-local statistical label fusion for multi-atlas segmentation. Medical image analysis 2013;17(2):194-208.

183. Filippi M, Paty DW, Kappos L, Barkhof F, Compston DA, Thompson AJ, Zhao GJ, Wiles CM, McDonald WI, Miller DH. Correlations between changes in disability and T2-weighted brain MRI activity in multiple sclerosis: a follow-up study. Neurology 1995;45(2):255-260.

184. Fox RJ. Refining diagnosis of multiple sclerosis with revised MRI criteria. Lancet neurology 2016.

185. Filippi M, Rocca MA, Ciccarelli O, De Stefano N, Evangelou N, Kappos L, Rovira A, Sastre-Garriga J, Tintore M, Frederiksen JL, Gasperini C, Palace J, Reich DS, Banwell B, Montalban X, Barkhof F, Group MS. MRI criteria for the diagnosis of multiple sclerosis: MAGNIMS consensus guidelines. Lancet neurology 2016;15(3):292-303.

186. Dorenbeck U, Schreyer AG, Grunwald IQ, Held P, Feuerbach S, Seitz J. Degenerative diseases of the lumbar spine. Comparison of the multiecho data image combination

sequence with magnetization transfer saturation pulse versus lumbar myelography/postmyelographic computed tomography. Acta Radiol 2004;45(8):866-873.

187. Mori Y, Murakami M, Arima Y, Zhu D, Terayama Y, Komai Y, Nakatsuji Y, Kamimura D, Yoshioka Y. Early pathological alterations of lower lumbar cords detected by ultrahigh-field MRI in a mouse multiple sclerosis model. Int Immunol 2014;26(2):93-101.

188. Wujek JR, Bjartmar C, Richer E, Ransohoff RM, Yu M, Tuohy VK, Trapp BD. Axon loss in the spinal cord determines permanent neurological disability in an animal model of multiple sclerosis. J Neuropathol Exp Neurol 2002;61(1):23-32.

189. Bosma RL, Stroman PW. Characterization of DTI Indices in the Cervical, Thoracic, and Lumbar Spinal Cord in Healthy Humans. Radiol Res Pract 2012;2012:143705.

190. Duan Q, van Gelderen P, Duyn J. Improved Bloch-Siegert based B1 mapping by reducing off-resonance shift. NMR in biomedicine 2013;26(9):1070-1078.

191. Sacolick LI, Wiesinger F, Hancu I, Vogel MW. B1 mapping by Bloch-Siegert shift. Magnetic resonance in medicine : official journal of the Society of Magnetic Resonance in Medicine / Society of Magnetic Resonance in Medicine 2010;63(5):1315-1322.

192. Wang J, Qiu M, Constable RT. In vivo method for correcting transmit/receive nonuniformities with phased array coils. Magnetic resonance in medicine : official journal of the Society of Magnetic Resonance in Medicine / Society of Magnetic Resonance in Medicine 2005;53(3):666-674.

193. Varma G, Girard OM, Prevost VH, Grant AK, Duhamel G, Alsop DC. Interpretation of magnetization transfer from inhomogeneously broadened lines (ihMT) in tissues as a dipolar order effect within motion restricted molecules. Journal of magnetic resonance 2015;260:67-76.

194. Girard O, Varma G, Mchinda S, Prevost VH, Le Troter A, Rapacchi S, Guye M, Ranjeva JP, Alsop DC, Duhamel G. Theoretical and Experimental Optimization of a 3D Steady-State Inhomogeneous Magnetization Transfer (ihMT) Gradient Echo Sequence: Boosting the ihMT Sensitivity with Sparse Energy Deposition. 2016; Singapore, Singapore.

195. Opella SJ. Structure determination of membrane proteins in their native phospholipid bilayer environment by rotationally aligned solid-state NMR spectroscopy. Accounts of chemical research 2013;46(9):2145-2153.

196. Huster D, Yao X, Hong M. Membrane protein topology probed by (1)H spin diffusion from lipids using solid-state NMR spectroscopy. Journal of the American Chemical Society 2002;124(5):874-883.

197. Manning A, Chang K, MacKay A, Micahl C. ihMT: Is It misnamed? A simple theoretical description of "inhomogeneous" MT.; 2016; Singapore, Singapore.

198. Yeung HN, Adler RS, Swanson SD. Transient Decay of Longitudinal Magnetization in Heterogeneous Spin Systems under Selective Saturation. IV. Reformulation of the Spin-Bath-Model Equations by the Redfield-Provotorov Theory. Journal of Magnetic Resonance, Series A 1994;106(1):37-45.

199. Provotorov BN. MAGNETIC RESONANCE SATURATION IN CRYSTALS. JETP 1962;14(5):9.

200. Prevost VH, Girard OM, Varma G, Alsop DC, Duhamel G. Minimizing the effects of magnetization transfer asymmetry on inhomogeneous magnetization transfer (ihMT) at ultra-high magnetic field (11.75 T). Magma 2016.

201. Swanson SD, Malyarenko D, Schmiedlin-Ren P, Adler J, Helvie K, Reingold L, Al-Hawary M, Zimmerman E. Lamellar liquid crystal phantoms for MT - Calibration and quality control in clinical studies. 2012; Melbourne, Australia.

202. Smith SM, Jenkinson M, Woolrich MW, Beckmann CF, Behrens TE, Johansen-Berg H, Bannister PR, De Luca M, Drobnjak I, Flitney DE, Niazy RK, Saunders J, Vickers J, Zhang Y, De Stefano N, Brady JM, Matthews PM. Advances in functional and structural MR image analysis and implementation as FSL. NeuroImage 2004;23 Suppl 1:S208-219.

203. Woolrich MW, Jbabdi S, Patenaude B, Chappell M, Makni S, Behrens T, Beckmann C, Jenkinson M, Smith SM. Bayesian analysis of neuroimaging data in FSL. NeuroImage 2009;45(1 Suppl):S173-186.

204. Girard OM, Callot V, Prevost VH, Robert B, Taso M, Ribeiro G, Varma G, Rangwala N, Alsop DC, Duhamel G. Magnetization transfer from inhomogeneously broadened lines (ihMT): Improved imaging strategy for spinal cord applications. Magnetic resonance in medicine

: official journal of the Society of Magnetic Resonance in Medicine / Society of Magnetic Resonance in Medicine 2016.

205. Taso M, Girard OM, Duhamel G, Le Troter A, Feiweier T, Guye M, Ranjeva JP, Callot V. Tract-specific and age-related variations of the spinal cord microstructure: a multi-parametric MRI study using diffusion tensor imaging (DTI) and inhomogeneous magnetization transfer (ihMT). NMR in biomedicine 2016.

206. Ropele S, Seifert T, Enzinger C, Fazekas F. Method for quantitative imaging of the macromolecular 1H fraction in tissues. Magnetic resonance in medicine : official journal of the Society of Magnetic Resonance in Medicine / Society of Magnetic Resonance in Medicine 2003;49(5):864-871.

207. Ropele S, Fazekas F. Magnetization transfer MR imaging in multiple sclerosis. Neuroimaging Clin N Am 2009;19(1):27-36.

208. Dula AN, Pawate S, Dortch RD, Barry RL, George-Durrett KM, Lyttle BD, Dethrage LM, Gore JC, Smith SA. Magnetic resonance imaging of the cervical spinal cord in multiple sclerosis at 7T. Multiple sclerosis 2016;22(3):320-328.

209. Dula AN, Arlinghaus LR, Dortch RD, Dewey BE, Whisenant JG, Ayers GD, Yankeelov TE, Smith SA. Amide proton transfer imaging of the breast at 3 T: establishing reproducibility and possible feasibility assessing chemotherapy response. Magnetic resonance in medicine : official journal of the Society of Magnetic Resonance in Medicine / Society of Magnetic Resonance in Medicine 2013;70(1):216-224.

210. Jones CK, Schlosser MJ, van Zijl PC, Pomper MG, Golay X, Zhou J. Amide proton transfer imaging of human brain tumors at 3T. Magnetic resonance in medicine : official journal of the Society of Magnetic Resonance in Medicine / Society of Magnetic Resonance in Medicine 2006;56(3):585-592.

211. Tietze A, Blicher J, Mikkelsen IK, Ostergaard L, Strother MK, Smith SA, Donahue MJ. Assessment of ischemic penumbra in patients with hyperacute stroke using amide proton transfer (APT) chemical exchange saturation transfer (CEST) MRI. NMR in biomedicine 2014;27(2):163-174.

212. Tee YK, Harston GW, Blockley N, Okell TW, Levman J, Sheerin F, Cellerini M, Jezzard P, Kennedy J, Payne SJ, Chappell MA. Comparing different analysis methods for quantifying the MRI amide proton transfer (APT) effect in hyperacute stroke patients. NMR in biomedicine 2014;27(9):1019-1029.

213. Li H, Zu Z, Zaiss M, Khan IS, Singer RJ, Gochberg DF, Bachert P, Gore JC, Xu J. Imaging of amide proton transfer and nuclear Overhauser enhancement in ischemic stroke with corrections for competing effects. NMR in biomedicine 2015;28(2):200-209.

214. Dula AN, Dewey BE, Arlinghaus LR, Williams JM, Klomp D, Yankeelov TE, Smith S. Optimization of 7-T Chemical Exchange Saturation Transfer Parameters for Validation of Glycosaminoglycan and Amide Proton Transfer of Fibroglandular Breast Tissue. Radiology 2014:140762.

215. Zhang XY, Wang F, Afzal A, Xu J, Gore JC, Gochberg DF, Zu Z. A new NOE-mediated MT signal at around -1.6ppm for detecting ischemic stroke in rat brain. Magnetic resonance imaging 2016.

216. Jones CK, Huang A, Xu J, Edden RA, Schar M, Hua J, Oskolkov N, Zaca D, Zhou J, McMahon MT, Pillai JJ, van Zijl PC. Nuclear Overhauser enhancement (NOE) imaging in the human brain at 7T. NeuroImage 2013;77:114-124.

217. Kim M, Gillen J, Landman BA, Zhou J, van Zijl PC. Water saturation shift referencing (WASSR) for chemical exchange saturation transfer (CEST) experiments. Magnetic resonance in medicine : official journal of the Society of Magnetic Resonance in Medicine / Society of Magnetic Resonance in Medicine 2009;61(6):1441-1450.

218. Lu H, Nagae-Poetscher LM, Golay X, Lin D, Pomper M, van Zijl PC. Routine clinical brain MRI sequences for use at 3.0 Tesla. Journal of magnetic resonance imaging : JMRI 2005;22(1):13-22.

219. Jin T, Wang P, Zong X, Kim SG. MR imaging of the amide-proton transfer effect and the pH-insensitive nuclear overhauser effect at 9.4 T. Magnetic resonance in medicine : official journal of the Society of Magnetic Resonance in Medicine / Society of Magnetic Resonance in Medicine 2013;69(3):760-770.

220. Dortch RD, Moore J, Li K, Jankiewicz M, Gochberg DF, Hirtle JA, Gore JC, Smith SA. Quantitative magnetization transfer imaging of human brain at 7 T. NeuroImage 2013;64:640-649.

221. Harrison R, Bronskill MJ, Henkelman RM. Magnetization transfer and T2 relaxation components in tissue. Magnetic resonance in medicine : official journal of the Society of Magnetic Resonance in Medicine / Society of Magnetic Resonance in Medicine 1995;33(4):490-496.

222. Whittall KP, MacKay AL. Quantitative interpretation of NMR relaxation data. Journal of Magnetic Resonance (1969) 1989;84(1):134-152.

223. Clark DJ, Smith AK, Dortch RD, Knopp MV, Smith SA. Investigating hydroxyl chemical exchange using a variable saturation power chemical exchange saturation transfer (vCEST) method at 3 T. Magnetic resonance in medicine : official journal of the Society of Magnetic Resonance in Medicine / Society of Magnetic Resonance in Medicine 2015.